Investigating the Response of Small-Diameter Buried Steel Pipes to Axial Ground Movements

by

© Sudipto Nath Priyom

A thesis submitted to the

School of Graduate Studies

in partial fulfillment of the requirements for the degree of

Master of Engineering

Faculty of Engineering and Applied Science

Memorial University of Newfoundland

May 2025

St. John's Newfoundland

Abstract

Small-diameter steel pipes are widely used for energy transportation to domestic supplies across Canada. These distribution pipelines often encounter ground movement, leading to pipe distress and failures. This research focuses on the responses of distribution pipes to axial ground movement using full-scale tests and numerical modeling. In the full-scale laboratory tests, a soil box was moved axially at a constant speed while a steel pipe buried in the soil box was restrained at one end, simulating the axial ground movement. Three different pipe diameters (26.7 mm, 60.3 mm, and 114.3 mm) were studied. Two compaction techniques, namely, hand tamper compaction and vibratory plate compaction, were used to examine the effects of different backfill compaction methods. The soil box was moved at three constant speeds (0.5 mm/min, 1.0 mm/min, and 2.0 mm/min) to observe the impact of varying ground displacement rates. Strain at the pipe's restrained end and pipe elongation were also measured. The test results for the 114.3 mm pipe at a pulling rate of 0.5 mm/min were simulated using finite element (FE) analysis to examine the soil-pipe interaction numerically, which could not be measured during experiments. The effect of interface dilation was found to be negligible in the numerical simulation, indicating that the increase in axial soil resistance on the pipe under dense sand conditions was most likely due to compaction-induced ground stresses and the surface roughness of the pipe. Three different approaches were employed to simulate the compaction-induced ground stresses and the resulting peak axial soil forces for the 114.3 mm diameter pipe. The effect of pipeline misalignment on the results was also studied using FE analysis.

Acknowledgment

The author expresses sincere gratitude to **Almighty God** for granting the mental clarity and well-being necessary to complete this research.

The author extends deep appreciation to his supervisor, **Prof. Dr. Ashutosh Sutra Dhar**, Faculty of Engineering and Applied Science, Memorial University of Newfoundland, for his unwavering guidance, expertise, and continuous support throughout this research. Without his encouragement and mentorship, the author's dream of pursuing his master's degree in Canada would not have been possible.

The author would also like to thank **Prof. Dr. Bipul Hawlader**, Faculty of Engineering and Applied Science, Memorial University of Newfoundland, for his valuable advice and insightful suggestions that significantly contributed to the success of this work.

Special thanks to the research team members for their dedication, technical expertise, and support throughout the research process. Financial and in-kind support for this research was provided by the National Science and Engineering Research Council of Canada, FortisBC Energy Inc., SaskEnergy Canada Inc., and WSP Canada Inc., which is greatly appreciated. The author deeply appreciates the laboratory and technical assistance provided by the laboratory technicians.

The author will be forever grateful to his wife, **Rituparna Nath**, whose unwavering support and encouragement were a constant source of strength throughout this journey. The author is also profoundly thankful to his parents and younger brother for their love, support, and encouragement.

Table of Contents

Abstract ii

Acknowledgment iii

List of Figures vii

List of Tables xi

Chapter 1: Introduction 1

1.1 Background 1

1.2 Statement of the Problem 2

1.3 Research Objectives 4

1.4 Thesis Organization 5

1.5 Key Contribution 6

1.6 Co-authorship Statement 6

Chapter 2: Literature Review 7

2.1 Introduction 7

2.2 Overview of Canada's Oil and Gas Industry and Transportation 7

2.3 Pipeline Incidents in Canada 9

2.4 Pipeline Performances Subjected to Geotechnical Hazards 10

2.4.1 Wave Propagation Hazard 11

2.4.2 Permanent Ground Deformation (PGD) Hazard 12

2.5 Modeling of Soil-Pipe Interaction 16

2.5.1 Axial Soil-Pipe Interaction 18

2.5.2 Traverse-Horizontal Soil-Pipe Interaction 21

2.5.3 Traverse-Vertical Upward Soil-Pipe Interaction 22
2.5.4 Traverse-Vertical Downward Soil-Pipe Interaction 24
2.6 Full-Scale Laboratory Testing on Axial Soil-Steel Pipe Interaction 25
2.7 Numerical Modeling of Axial Soil-Steel Pipe Interaction 33
2.8 Summary of Key Observations 34
Chapter 3: Full-Scale Laboratory Testing on Small-Diameter Steel Pipes........................ 36
3.1 Abstract.. 36
3.2 Introduction 37
3.3 Experimental Program 42
3.3.1 Pipes and Backfill Material 42
3.3.2 Test Facility 44
3.3.3 Test Preparation 45
3.4 Results and Discussion 49
3.4.1 Force–Displacement Response.. 49
3.4.2 Effects of Backfill Compaction 54
3.5 Conclusions 63
3.6 Acknowledgment.. 65
3.7 References 65
Chapter 4: Finite Element Modeling of Axial Soil-Pipe Interaction for Small-Diameter Steel Pipes 72
4.1 Introduction 72
4.2 Constitutive Modeling of Soil 73
4.3 Soil Parameters 74

4.4 Interface Parameter 77

4.5 Model Geometry and Meshing 78

4.6 Use of Higher Lateral Earth Pressure Coefficient (K Model) 81

4.7 Use of Compaction-Induced Stress (Compaction Model) 92

4.8 Use of Radial Expansion (Cavity Expansion Model) 103

4.9 Effect of Inclination Angle 109

4.10 Parametric Study 112

4.10.1 Effect of Soil Parameters 112

4.10.2 Effect of Interface Friction Factor 116

4.11 Conclusions 118

4.12 Reference 120

Chapter 5: Conclusion and Recommendations 126

5.1 Overview 126

5.2 Conclusions 126

5.3 Recommendations 128

References 130

Appendix A: Figures of Test Setup and Procedure 136

List of Figures

Figure 2.1: Canada’s pipeline infrastructure (NRC 2020) 9

Figure 2.2: Axial force in the pipe for shorter PGD zone (O’Rourke and Liu 2012) 13

Figure 2.3: Axial force in the pipe for larger PGD zone (O’Rourke and Liu 2012) 14

Figure 2.4: Traverse PGD (ALA 2005) 15

Figure 2.5: Pipe on Winkler foundation (after ALA 2005) 17

Figure 2.6: Variations of adhesion factor with undrained shear strength (ALA 2005) 20

Figure 2.7: Horizontal bearing capacity factors (Hansen 1961) 21

Figure 2.8: Vertical uplift factors (ALA 2005) 23

Figure 2.9: Bearing capacity factors (ALA 2005) 24

Figure 3.1: Pipeline failure during the 1994 Northridge earthquake (USGS 2021) 39

Figure 3.2: Laboratory idealization of axial ground movement 41

Figure 3.3: Schematic diagram of the test facility 45

Figure 3.4: Pipe placement (a) on the bedding ; (b) cross-sectional view 46

Figure 3.5: (a) Hand tamper; (b) Vibratory plate compactor 47

Figure 3.6: (a) Force–displacement response; (b) Normalized force–displacement curve 52

Figure 3.7: Normalized force vs. tank displacement 53

Figure 3.8: (a) Effect for different backfill compactions; (b) Peak normalized force vs. pipe diameter 56

Figure 3.9: Pipe elongation with tank displacement 57

Figure 3.10: Axial strain distribution at the restrained end 59

Figure 3.11: Peak pipe axial force with pulling rates..60

Figure 3.12: Normalized force vs. tank displacement 61

Figure 3.13: Soil pulling and pipe pulling comparison...63

Figure 4.1: Mohr–Coulomb failure criteria 74

Figure 4.2: (a) 4 × 2 × 1.225 m soil domain; (b) Finer mesh near pipe cross-section; (c) 4.5 m long pipe domain; (d) Pipe cross-section..80

Figure 4.3: Distribution of K along the springline level 82

Figure 4.4: Soil displacement in gravity step...83

Figure 4.5: Energy check for K model...84

Figure 4.6: Comparison of FE analysis and full-scale laboratory Test-3 (K model) 85

Figure 4.7: Development of plastic deformation zone around the pipe............................86

Figure 4.8: Distribution of normal stress (in kPa) around the pipe circumference at peak axial force (K model) 87

Figure 4.9: Distribution of normal stress with tank displacement (K model)....................88

Figure 4.10: Distribution of shear stress with tank displacement at 0.50L (K model) 89

Figure 4.11: Distribution of average shear stress at 0.25L, 0.50L, and 0.75L (K model) .90

Figure 4.12: Maximum von Mises stress at different pipe sections..................................91

Figure 4.13: Comparison of FE analysis and full-scale laboratory Test-3 (Compaction model) 95

Figure 4.14: Distribution of horizontal stress (after Reza and Dhar 2024)........................96

Figure 4.15: Applied temperature to soil domain (122 °C at springline level)..................97

Figure 4.16: Comparison of FE analysis and full-scale laboratory Test-3 (Compaction model) 98
Figure 4.17: Distribution of normal stress (in kPa) around the pipe circumference at peak axial force (Compaction model) 99
Figure 4.18: Distribution of normal stress with tank displacement (Compaction model) 100
Figure 4.19: Distribution of average shear stress at 0.50L, and 0.75L (Compaction model) 101
Figure 4.20: Lengthwise axial strain distribution on the crown 102
Figure 4.21: Expansion of pipe diameter (mm) 104
Figure 4.22: Comparison of FE analysis and full-scale laboratory Test-3 (Expansion model) 105
Figure 4.23: Distribution of normal stress (in kPa) around the pipe circumference at peak axial force (Expansion model) 106
Figure 4.24: Distribution of normal stress with tank displacement (Expansion model)..107
Figure 4.25: Distribution of average shear stress at 0.50L (Expansion model) 108
Figure 4.26: Force–displacement responses for oblique loading conditions 110
Figure 4.27: Bending strain distribution for the horizontal oblique condition 111
Figure 4.28: Effect of soil modulus on peak pipe axial force 113
Figure 4.29: Effect of friction angle on peak pipe axial force 114
Figure 4.30: Effect of dilation angle on peak pipe axial force 115
Figure 4.31: Effect of interface friction factor on peak pipe axial force 117

Figure A.1: Full-scale test facility developed at Memorial University of Newfoundland (Side view) 136

Figure A.2: Full-scale test facility developed at Memorial University of Newfoundland (Front view) 137

Figure A.3: Load cell connection 138

Figure A.4: Sand dumping process inside the tank 139

Figure A.5: Finished surface after the hand tamper compaction of the first layer 140

Figure A.6: Density measurement process using the sand-cone method (ASTM D1556) 141

Figure A.7: Pipe segment after the test 142

List of Tables

Table 2.1: Friction factor for different types of external pipe coatings (ALA 2005).........20

Table 3.1: Physical properties of the sand (after Saha et al. 2019)..................................42

Table 3.2: Physical properties of steel pipes...43

Table 3.3: Mechanical properties of steel pipes..43

Table 3.4: Test configuration...49

Table 4.1: Soil parameters used in FE analysis..78

Chapter 1: Introduction

1.1 Background

Energy pipelines play a pivotal role in the global infrastructure landscape, serving as safe, reliable, and highly efficient means for transporting crude oil, natural gas, and municipal water worldwide. Canada ranks as the second-largest nation with an extensive energy pipeline network, following the United States (Katebi et al. 2019). Most of the onshore pipelines are strategically buried underground to ensure physical support and protection against potential damage (Saberi et al. 2022). However, challenges arise when these pipelines are routed through unstable ground conditions. Various geological events, such as landslides, earthquakes, slope movement, and land subsidence, can lead to permanent ground deformation (PGD), making the ground unstable. Although PGDs are localized to specific pipeline zones, their potential for damage is significant, resulting in an unacceptable level of strain. This strain can cause pinhole leaks and local buckling, ultimately causing damage to the pipeline (O'Rourke and Nordberg 1992, Kunert et al. 2016). The environmental and economic consequences of pipeline failures can be severe, making it necessary to address the challenges caused by unstable soil conditions.

To understand and mitigate the impact of PGD on buried pipelines, current design guidelines (ALA 2005, PRCI 2009) suggest methods of analyzing soil-pipe interaction, considering (a) axial, (b) traverse-horizontal, (c) traverse-vertical upward, and (d) traverse-vertical downward relative ground movements. These guidelines use bilinear elasto-plastic models to describe the force–displacement behavior in these interactions. Several comprehensive investigations have been conducted in recent years to improve understanding of the force–displacement behavior, including full-scale laboratory tests and numerical modeling. Researchers have focused on a diverse range of pipeline materials, including straight and branched polyethylene pipes (Anderson 2004, Weerasekara and Wijewickreme 2008, Bilgin and Stewart 2009a, Muntakim and Dhar 2021, Reza and Dhar 2021, Chakraborty et al. 2021, Reza et al. 2023), ductile iron pipes (Murugathasan et al. 2021), cast iron pipes (Bilgin and Stewart 2009b), and steel pipes (Karimian 2006, Wijewickreme et al. 2009, Sarvanis et al. 2017, Meidani et al. 2018, Sheil et al. 2018, Andersen 2024). These studies provide valuable insights into the soil-pipe interaction for optimizing pipeline design and ensuring resilience against ground movements. Note that in most studies, the buried pipe is pulled through static soil masses. However, in real ground movement situations, the pipeline is often restrained in stable ground while the surrounding ground moves in different directions.

In response to this distinction, a full-scale laboratory test facility has been developed at Memorial University of Newfoundland. The facility achieves the relative axial displacement between the pipe and soil by moving the soil box at a constant rate while keeping the pipe fixed at one end. The current study specifically involves small-diameter steel pipes (26.7 mm, 60.3 mm, and 114.3 mm), contributing to ongoing efforts to enhance the safety and reliability of distribution pipeline systems.

1.2 Statement of the Problem

The mechanical design of the pipeline is generally based on the hoop stress induced by the internal pressure. According to the design code, this hoop stress should be maintained below a specified fraction of the minimum yield stress. However, a critical aspect often overlooked in this process is the influence of the surrounding soil on the pipeline (Saleh et al. 2021). The current design guidelines (ALA 2005, PRCI 2009) provide equations to estimate the ultimate soil resistance per unit length of the pipeline. Although these design equations have been successful in estimating the axial pullout resistance under loose backfill, they tend to underestimate the axial pullout resistance in dense backfill conditions due to the dilatancy effect caused by shearing at the pipe-soil interface (Bilgin and Stewart 2009, Wijewickreme et al. 2009, Murugathasan et al. 2021). It is important to note that most studies in this domain focus on the behavior of large-diameter transmission pipelines, leaving a gap in understanding the smaller-diameter distribution pipeline systems.

On the other hand, the backfill material should be compacted (uniformly) to avoid excessive deformation and failure of the soil surrounding shallow-buried pipes. Although the effect of compaction on vertical overburden stress is insignificant, it may induce additional horizontal pressure due to the development of a shear failure zone near the surface. The horizontal pressure may reach Rankine's passive pressure near the surface due to compaction (Duncan et al. 1991, Chen and Fang 2008). It is important to note that the horizontal pressure converges to Jaky's "at-rest" stress below the compaction-influenced zone. However, if heavy compaction equipment is used, the horizontal pressure can exceed the at-rest stress by up to a depth of 9 m (30 feet) or more below the ground surface (Duncan et al. 1991). The induced horizontal pressure remains unchanged for cohesionless backfill over time and becomes a function of lift thickness and compaction energy input for the same soil mass (Chen and Fang 2008). Duncan et al. (1991) estimated the maximum and residual horizontal pressure due to compaction using rollers, vibratory plate compactors, and rammer plates. For shallow-buried distribution pipelines, this compaction-induced horizontal pressure may significantly increase the normal stress at the pipe springline level and contribute to the ultimate soil resistance experienced by the pipeline during the axial pullout. Acknowledging these factors, it becomes crucial to thoroughly understand how dilatancy and the methods used for backfill compaction can affect distribution pipeline systems.

1.3 Research Objectives

This study aims to comprehensively investigate the behavior of small-diameter buried steel pipes subjected to axial ground movement. The specific objectives include:

- Conducting a series of full-scale laboratory tests on bare steel pipes with diameters of 26.7 mm, 60.3 mm, and 114.3 mm, under axial ground movement. The primary focus is to understand the mechanisms involved in soil-pipe interaction during these tests.
- Assessing the impact of two distinct backfill compaction methods, namely vibratory plate compaction and hand tamper compaction, on the overall response of the pipeline. This investigation aims to highlight the significance of the compaction process in influencing the pipeline's behavior.
- Understanding how different soil displacement rates (i.e., 0.5 mm/min, 1.0 mm/min, and 2.0 mm/min) influence the peak axial soil resistance on these pipe segments.

- Developing 3D numerical models to simulate the axial soil-pipe response. The model will be validated using the results of the conducted laboratory tests.
- Comparing the obtained test results with existing design guidelines and offering suggestions for enhancing the current approach to pipeline design. This comparative analysis aims to identify potential improvements in the design methodology based on the laboratory experiments.

1.4 Thesis Organization

This thesis is structured across five chapters and two appendices, each contributing to a comprehensive understanding of the research. Chapter 1 serves as an introduction, providing background information and explaining the significant objectives of the research work.

Chapter 2 delves into the current pipeline status in Canada, reviewing existing design guidelines related to soil-pipe interactions. This chapter also summarizes previous full-scale laboratory testing and numerical modeling on steel pipes under axial ground movement conditions. It concludes by presenting key observations derived from these research endeavors.

In Chapter 3, the focus shifts to the full-scale laboratory testing of bare steel pipes with diameters of 26.7 mm, 60.3 mm, and 114.3 mm, subjected to three axial ground movement rates (0.5 mm/min, 1.0 mm/min, and 2.0 mm/min). This chapter details the development of the full-scale test facility at Memorial University of Newfoundland, highlighting axial force distribution on the pipe restrained end to the ground movement and presenting pipe strain results. The interpretation of the test results, along with a comparison to existing design guidelines, is also incorporated into this chapter.

Chapter 4 introduces the 3D numerical modeling of axial ground movement effects on bare steel pipes. The development and validation of the finite element model are discussed in conjunction with the experimental results.

Chapter 5 concludes the study, offering an overall summary along with recommendations and suggestions for future research directions.

Appendix A includes some pictures taken during the tests to enhance the understanding of the test conditions.

1.5 Key Contribution

Conference Paper

Priyom, S.N., Dhar, A.S., and Reza, A. 2024. Assessing axial soil resistance in small-diameter steel pipes under different backfill compactions, In Proc., of the *77th Canadian Geotechnical Conference*, GeoMontréal 2024, Canada, September 15-18.

1.6 Co-authorship Statement

The research work presented in the conference paper was carried out by the author, Sudipto Nath Priyom, under the guidance of Dr. Ashutosh Sutra Dhar. The laboratory experiments presented in the paper were conducted by the first author, who also drafted the manuscript. The other authors supervised the research and reviewed the manuscript.

Chapter 2: Literature Review

2.1 Introduction

The use of small-diameter steel pipes for natural gas distribution lines is a widespread practice in Canada. These pipelines often encounter ground movement, significantly increasing the risk of distress or rupture over time. Recent research efforts have predominantly focused on investigating the mechanism of pipe pulling through static soil masses to study the effects of axial ground movements on pipes. This literature review aims to present the current status of pipelines in Canada while exploring the existing design guidelines. Full-scale laboratory testing and numerical modeling of previous research work on steel pipes subjected to axial ground movements will also be summarized as a part of this chapter. The concluding section of this chapter will highlight some key observations derived from previous studies.

2.2 Overview of Canada's Oil and Gas Industry and Transportation

The economy of Canada is significantly dependent on its oil and gas extraction industry. As of 2023, Canada ranked fourth globally in crude oil production and fifth in natural gas production (Statistical Review of World Energy 2024). On average, the country produced 5.1 million barrels of crude oil and 17.9 billion cubic feet of natural gas daily that year (CER 2024). In 2023, the oil and gas extraction industry made a substantial contribution of $71.4 billion (3.2%) to Canada's overall Gross Domestic Product (GDP) and generated approximately 0.9 million job vacancies nationwide (CAPP 2024).

In tandem with this economic reliance on the oil and gas industry, Canada has established an extensive pipeline network of 840,000 kilometers (CER 2024). This intricate system efficiently transports oil and gas to both domestic refineries and international export markets. It is widely considered a safe means of energy transportation, as incidents such as spills, leaks, and ruptures are less likely to occur in pipelines compared to vessels, railways, or trucks (NRC 2020). In 2023, approximately 92% of crude oil exports were transported through pipelines, with the remaining 8% relying on marine vessels and railways. The role of pipelines is even more pronounced in the transportation of natural gas (CER 2024).

The Canadian pipeline network mainly consists of four distinct types of pipelines, namely gathering, feeder, transmission, and distribution lines. Gathering, feeder, and transmission lines transport crude oil and natural gas from the well to the collection point, while the distribution lines deliver natural gas to customers. Gathering and distribution pipelines are typically constructed with small-diameter pipes, with diameters ranging from 100 to 300 mm (4 to 12 inches) for gathering and from 12.5 to 150 mm (½ to 6 inches) for distribution lines. In contrast, transmission lines, responsible for long-distance transport, utilize larger-diameter pipes, ranging from 100 to 1,200 mm (4 to 48 inches) (NRC 2020). These pipelines can be classified based on the fluids they transport, service requirements, and operational conditions. Mostly, gathering and transmission pipelines are made with steel in Canada, while plastic is used as the construction material for distribution pipelines. Figure 2.1 shows the typical pipeline infrastructure network of Canada.

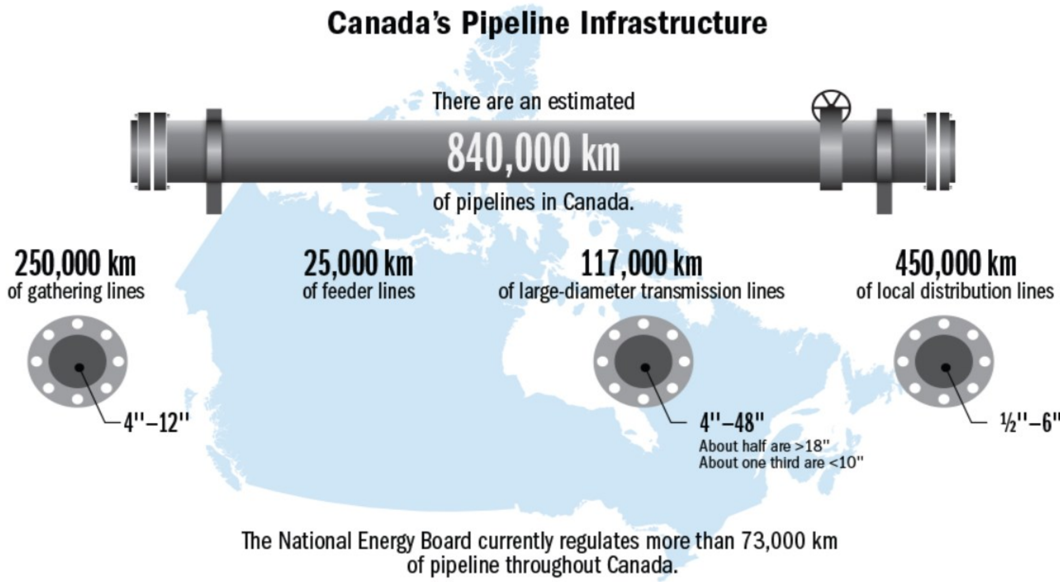

Figure 2.1: Canada's pipeline infrastructure (NRC 2020)

2.3 Pipeline Incidents in Canada

While pipelines are generally considered the safest and most environmentally friendly means of transporting oil and natural gas, recent years have seen several reported incidents related to pipeline failure (NRC 2020). In 2023, there were 68 federally regulated pipeline incidents reported to the Transportation Safety Board of Canada (TSB 2024). This marked a 20% decrease from the last five-year average. 25% of these incidents were linked to the release of crude oil and natural gas, with the majority involving non-release incidents. These incidents highlight the importance of understanding and addressing the various factors contributing to pipeline failures.

One of the most common causes of pipeline rupture and leaks is corrosion. The gradual deterioration of external surface coatings over time facilitates soil moisture contact with the pipeline surface, resulting in corrosion cracking. A 200 mm natural gas pipeline rupture in 2022 near Fox Creek, Alberta, underscored the impact of external corrosion on pipeline integrity. Furthermore, pipelines transporting heavier fluids can exhibit an increased potential for internal corrosion, as evidenced by a 900 mm transmission pipeline rupture in 2018 near Wonowon, British Columbia. Manufacturing and construction defects constitute additional factors contributing to pipeline failures. Sometimes, construction or excavation crews accidentally hit the pipeline and damage it. In 2023, 25% of incidents were reported under this category, underscoring the need for enhanced safety protocols and coordination among stakeholders. Geohazards associated with geotechnical (e.g., ground subsidence, slope movement, landslide, etc.), hydrotechnical (e.g., bank erosion, scour, channel degradation, etc.), tectonic (e.g., liquefaction, lateral spreading, surface fault rupture, etc.) and other environmental activities can significantly threaten the integrity of onshore pipelines. Over the last five-year average, the highest number of pipeline incidents (36%) was associated with geohazards (TSB 2024). However, this literature study will exclusively focus on understanding the geotechnical impacts of geohazards on pipeline infrastructure.

2.4 Pipeline Performances Subjected to Geotechnical Hazards

The increasing demand for pipelines sometimes results in routing them through challenging geotechnical areas. These areas may exhibit significant volume changes due to wetting-drying and freezing-thawing cycles, nonuniform consolidation settlement, ground subsidence, etc., potentially leading to pipeline cracking or buckling (Kouretzis et al. 2015). Additionally, seismic hazards can pose a significant threat to the structural integrity of pipelines. Pipelines must withstand these geotechnical hazards to ensure the safe transportation of oil and gas.

The seismic hazard faced by pipelines can be classified into the following two categories, namely, wave propagation hazard and permanent ground-induced deformation (PGD) hazard (ALA 2005). Wave propagation hazard typically does not cause damage to continuous pipelines, whereas PGD can have a substantial impact on their structural integrity. The following sections will briefly delve into these two sources of seismic hazard.

2.4.1 Wave Propagation Hazard

The wave propagation hazard mainly arises from the generation of body waves (P-waves and S-waves) and surface waves (L-waves and R-waves) during a seismic event. These waves can propagate through the ground in all directions. S-waves carry more energy and cause stronger ground motion among the body waves. In contrast, surface waves propagate more slowly but cause higher ground strain than body waves. It's important to note that R-waves induce significantly higher ground strain compared to L-waves (O'Rourke and Liu 2012, Shi 2015).

Ground strain due to wave propagation hazards can be directly correlated to peak ground velocity. When the ground moves parallel to the propagation direction (i.e., R-waves), it generates axial strain in the pipeline. The induced axial strain in the buried pipeline due to surface waves can be represented by Equation (2.1) (O'Rourke and Liu 2012).

$$\varepsilon_{\mathrm{a}} = \frac{V_{\max}}{C_{\mathrm{R}}} \qquad (2.1)$$

where $V_{\max}$ represents the maximum horizontal ground velocity, and C_{R} is the propagation velocity of R-waves.

S-waves generally propagate perpendicular to the ground motion, resulting in bending strain on the pipelines. However, when the S-waves propagate at an angle to the pipeline axis, they can induce axial strain in the pipeline. The bending strain is generally neglected as it is relatively smaller than the axial strain. It is reported that the upper bound of axial strain can be estimated when the S-waves make an angle of 45° with the pipeline axis (O'Rourke and Liu 2012, Shi 2015).

$$\varepsilon_a = \frac{V_{max}}{2C_S} \tag{2.2}$$

In Equation (2.2), C_s represents the apparent propagation velocity of S-waves. ALA (2005) conservatively suggests using 2 km/sec for C_s.

ALA (2005) also introduces Equation (2.3) to calculate the friction-induced axial strain at the pipe-soil interface. However, the axial strain calculated using the above equations should not exceed the friction-induced axial strain.

$$\varepsilon_a \leq \frac{T_U \lambda}{4AE} \tag{2.3}$$

where T_U is the maximum friction per unit length at the pipe-soil interface, λ is defined as the apparent wavelength of seismic waves (usually taken as 1.0 km), A is the pipe cross-sectional area, and E is the modulus of elasticity of the pipe.

2.4.2 Permanent Ground Deformation (PGD) Hazard

Permanent ground deformation (PGD) refers to various geological events such as surface fault offsets, landslides, seismic settlement, and liquefaction-induced lateral spread.

These PGDs can pose a threat to pipeline infrastructure, making it crucial to address the effects.

Note that both axial and bending strains are induced in the pipelines due to these PGD hazards. Longitudinal PGD primarily induces axial stress on the pipeline, with the induced axial strain being controlled by the zone length (L) for comparatively shorter PGD zones (ALA 2005). Figure 2.2 illustrates the axial force in the pipeline for such scenarios. In such a case, the maximum displacement of the pipeline will be less than the ground displacement.

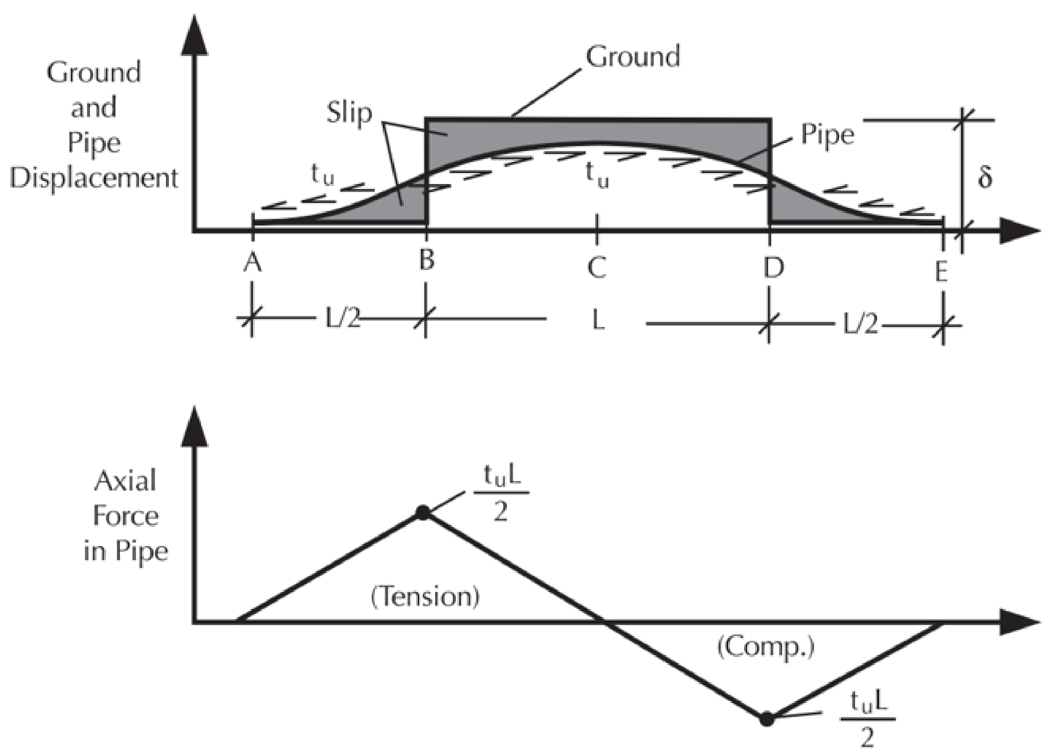

Figure 2.2: Axial force in the pipe for shorter PGD zone (O'Rourke and Liu 2012)

For larger PGD zones, the induced axial strain becomes a function of the ground displacement. The pipe stretches on either side (L_e) of the PGD zone to accommodate ground movement. Figure 2.3 illustrates the zones of compression and tension for the larger PGD zone. Note that there will be no axial force or strain for the middle zone since the pipeline displacement matches the ground movement.

The induced axial strain on the pipeline due to longitudinal PGD can be expressed by following the Ramberg-Osgood model (O'Rourke and Liu 2012):

$$\varepsilon(\mathrm{x}) = \frac{\beta_P x}{E}\left\{1+\frac{n}{1+r}\left(\frac{\beta_P x}{\delta_y}\right)^r\right\} \qquad (2.4)$$

where β_P is termed as pipe burial parameter (kN/m^3), E is the modulus of elasticity of pipeline material, n and r are the Ramberg-Osgood parameters, and δ_y is the effective yield stress.

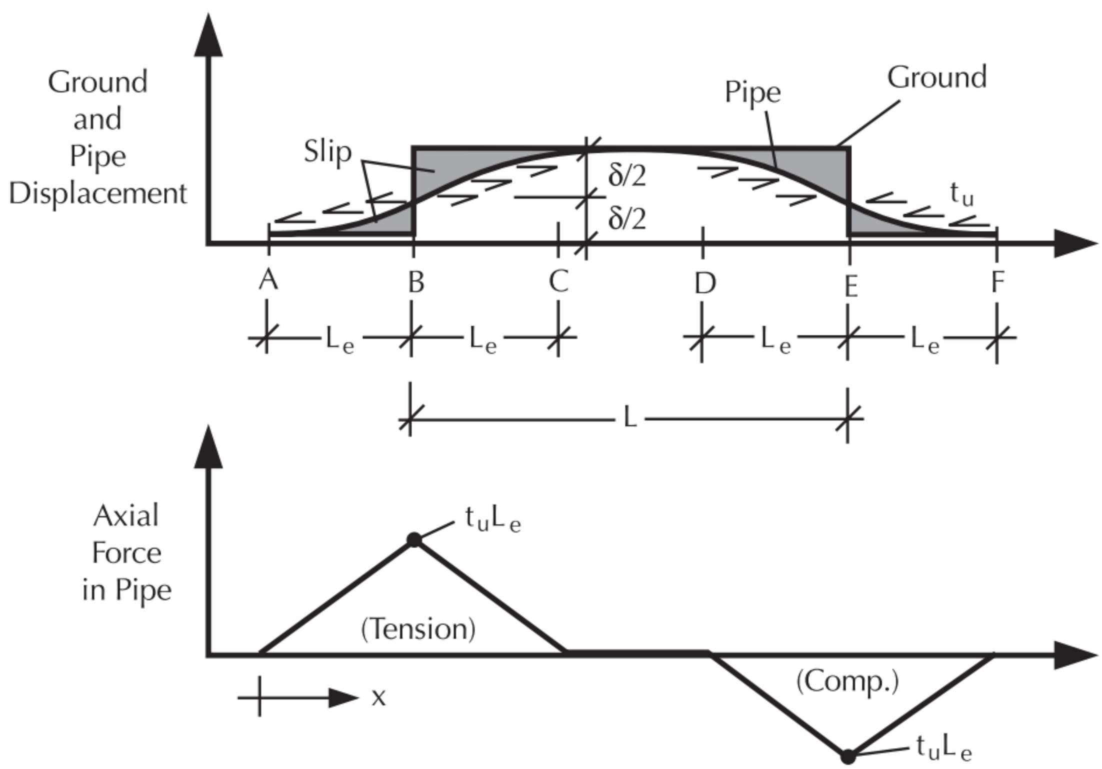

Figure 2.3: Axial force in the pipe for larger PGD zone (O'Rourke and Liu 2012)

Traverse PGD introduces both axial and flexure strains in the pipeline. Within this PGD zone, the pipeline behaves like a fixed-fixed beam, resulting in flexure strain. The pipeline also acts as a flexure cable in part, stretching to meet ground displacement and leading to axial tension. This axial tension at the edge of the PGD zone is resisted by the frictional forces at the soil-pipe interface. Note that the spatial distribution of ground movement also plays a significant role in the traverse PGD scenarios. For example, if the ground movement is uniform, the strain distribution will be relatively large at the edges of the PGD zone, as shown in Figure 2.4.

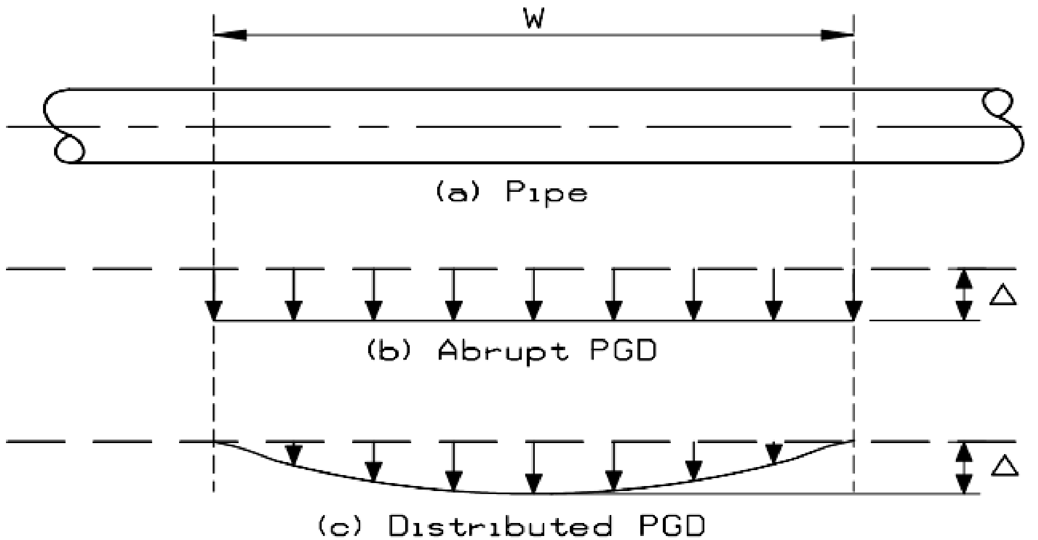

Figure 2.4: Traverse PGD (ALA 2005)

O'Rourke (1989) proposed Equations (2.5) and (2.6) to estimate the maximum bending strain in the pipeline subjected to spatially distributed traverse PGD. Note that when the width of the PGD zone is wide, the pipeline is flexible and in such cases, the pipe deformation matches the ground deformation. For narrower PGD zones, the pipeline is relatively stiff, and the pipe deformation is less than the ground deformation.

$$\varepsilon_b = \pm\frac{\pi^2 \delta D}{W^2} \qquad \text{[for wide PGD zone]} \qquad (2.5)$$

$$\varepsilon_b = \pm\frac{P_u W^2}{3\pi E t D^2} \qquad \text{[for narrow PGD zone]} \qquad (2.6)$$

where P_u denotes the maximum lateral force per unit length at the pipe-soil interface (kN/m), δ is the magnitude of ground deformation, W denotes the PGD zone, t is the pipe wall thickness, and D is the pipe diameter.

Both wave propagation and PGD hazards can introduce axial forces and bending moments in the pipeline, thereby generating strains in the pipe-soil interface. It is important to understand how the pipeline interacts with the surrounding soil during an event of ground movement. The subsequent sections will provide a concise exploration of the interface behavior between the pipeline and the surrounding soil, discussing the critical factors that influence the overall performance of pipelines.

2.5 Modeling of Soil-Pipe Interaction

During ground movement events, both normal and frictional forces are generated at the soil-pipe interface. The interaction of pipe and soil significantly influences the behavior of buried pipelines, giving rise to a force–displacement relationship commonly known as 'p-y curves' in geotechnical engineering. To conceptualize soil-pipe interaction, the pipeline is often idealized as a beam supported by soil springs, employing elasto-plastic models to describe its behavior.

In these models, ground deformation is categorized into axial, transverse-horizontal, and transverse-vertical components, as shown in Figure 2.5. Specifically, ground movement within ± 22.5° aligned with the pipeline axis is defined as axial, and movement within ± 22.5° across the axis is considered traverse (Dewar 2019). The force–displacement behavior in each direction is then expressed using independent soil springs. Key parameters in these elasto-plastic models include the maximum soil resistance at the interface and the maximum elastic deformation.

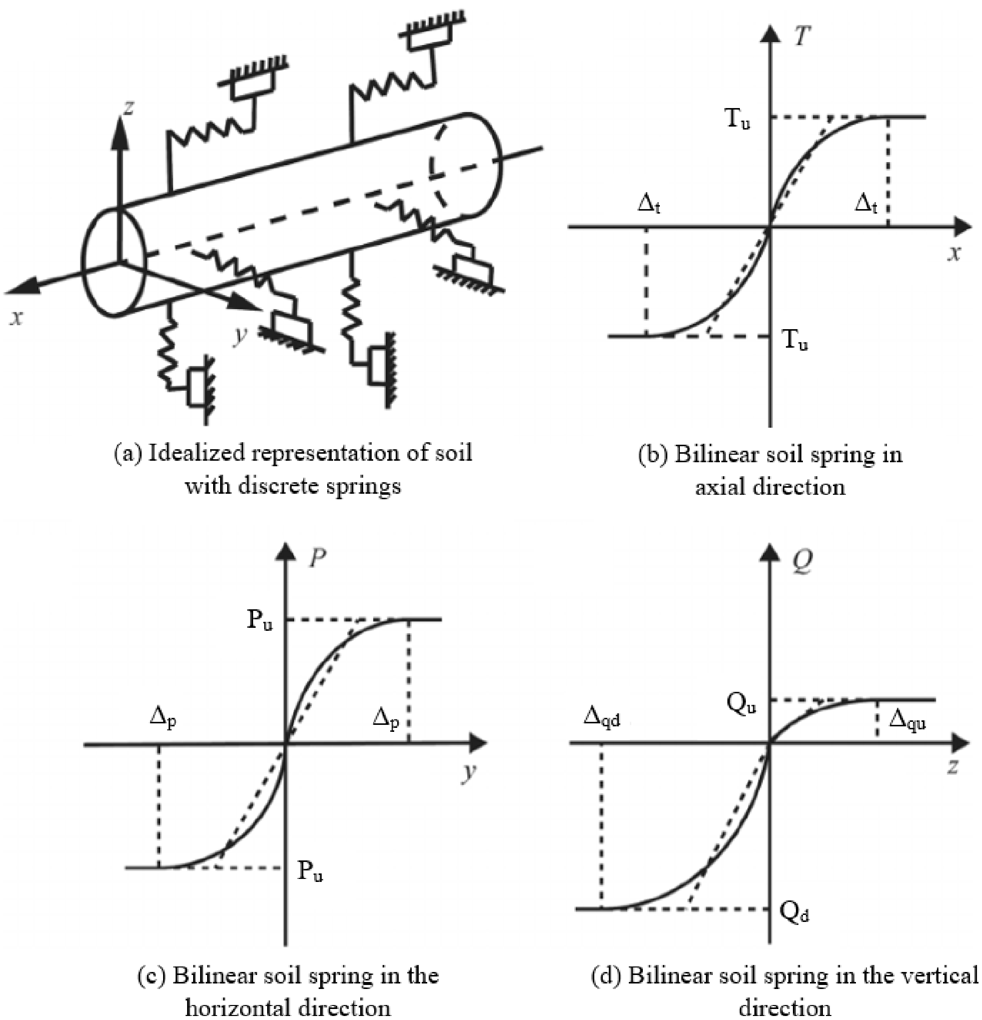

Figure 2.5: Pipe on Winkler foundation (after ALA 2005)

However, a limitation of these models is their assumption that the soil force remains constant once it reaches its maximum value. Contrary to this assumption, test results indicate that the maximum soil force decreases for larger relative displacements. It is important to note that these elasto-plastic models might underestimate the 'effective stiffness' since they idealize the actual 'roundhouse' curve (ASCE 1984). To address this limitation, ASCE (1984) recommends using twice the 'spring coefficient' (i.e., the maximum soil resistance to the maximum elastic deformation) to better represent the 'effective stiffness' for axial springs. The subsequent sections will provide brief descriptions of axial and transverse soil-pipe interaction to further explore these considerations.

2.5.1 Axial Soil-Pipe Interaction

The relative ground movement parallel to the pipeline axis gives rise to axial forces at the soil-pipe interface. The ALA (2005) guidelines provide the following equations to estimate the ultimate axial soil resistance per unit length transferable to the pipe:

$$T_u = \pi D H \bar{\gamma} \left(\frac{1+K_0}{2}\right) \tan\delta \qquad \text{[for sand]} \qquad (2.7)$$

$$T_u = \pi D \alpha c_u \qquad \text{[for undrained clay]} \qquad (2.8)$$

Here, H represents the burial depth of the pipe, K_0 is the coefficient of lateral earth pressure at rest, $\bar{\gamma}$ is the effective unit weight of soil, δ is the interface friction angle, α is the adhesion factor, and c_u denotes the undrained cohesion of the backfill soil. In most practical scenarios, loading is considered for relatively short periods; therefore, undrained conditions are assumed for clayey soil. However, the ground displacement required to achieve the ultimate axial soil resistance varies between 3 to 5 mm for dense to loose sand conditions and 8 to 10 mm for stiff to soft clay conditions (ALA 2005).

The term $\pi DH\bar{\gamma}\left(\frac{1+K_0}{2}\right)$ in Equation (2.7) denotes the 'average effective normal stress' acting around the outer perimeter of the pipeline at rest condition. Several empirical correlations are available to estimate K_0. However, the value of K_0 generally varies from 0.35 to 0.5 for cohesionless soil (Al-Hussaini and Townsend 1975). But when there is a relative movement between dense backfill and the pipeline, lateral strains develop in the soil, leading to increased normal stress around the outer diameter of the pipe. As a result, Equation (2.7) was found to underpredict the ultimate axial soil resistance in dense sand conditions due to soil dilation caused by shearing at the interface. To address this, Wijewickreme et al. (2009) proposed to use the effective lateral earth pressure coefficient, K, of value 2.0 rather than K_0 in Equation (2.7). Additionally, Meidani et al. (2018) proposed Equation (2.8) for the estimation of ultimate axial soil resistance using the modified coefficient of earth pressure, K^*, instead of K_0 in Equation (2.7).

$$K^* = 2.75 \times (1 - \sin\varphi) \times \left(\frac{E}{\gamma H}\right)^{0.38} \times \left(\frac{\varphi}{45}\right)^{1.39} \times \left(\frac{\Delta t}{D}\right)^{0.42} \qquad (2.9)$$

In Equation (2.8), Δt represents the thickness of the active shear zone, which depends on the median grain size (d_{50}) of the soil and can be estimated as, $\Delta t = 10d_{50}$.

The interface friction angle between pipe and soil (δ) is a function of the internal friction angle of the soil and the friction factor (f) and can be estimated as, $\delta = f\varphi$. ALA (2005) provides Table 2.1 to estimate the interface friction angle for different types of external pipe coatings.

Table 2.1: Friction factor for different types of external pipe coatings (ALA 2005)

Pipe coating	**Friction factor, *f***
Concrete	1.0
Coal tar	0.9
Rough steel	0.8
Smooth steel	0.7
Fusion bonded epoxy	0.6
Polyethylene	0.6

For the pipelines buried in cohesive soil, the adhesion factor (α) can be estimated from undrained shear strength as shown in Figure 2.6.

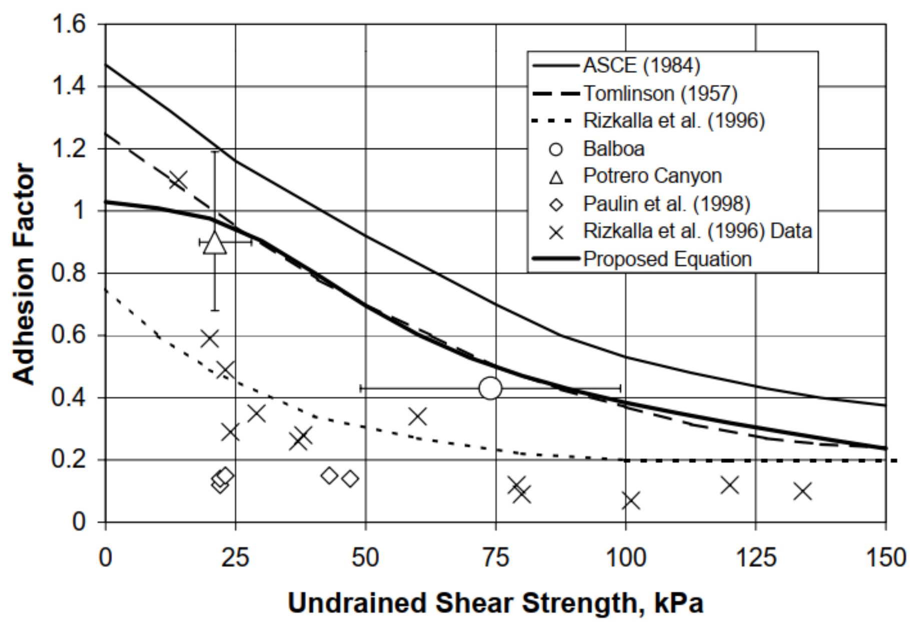

Figure 2.6: Variations of adhesion factor with undrained shear strength (ALA 2005)

2.5.2 Traverse-Horizontal Soil-Pipe Interaction

The relative ground movement perpendicular to the pipeline axis in the horizontal plane gives rise to traverse-horizontal forces at the interface. The ALA (2005) guidelines provide Equations (2.9) and (2.10) to estimate ultimate lateral soil resistance per unit length transferable to the pipe:

$$P_u = N_{qh}\bar{\gamma}HD \qquad \text{[for sand]} \qquad (2.10)$$

$$P_u = N_{ch}c_uD \qquad \text{[for undrained clay]} \qquad (2.11)$$

Here, N_{qh} and N_{ch} are the horizontal bearing capacity factors for sand and clay, respectively. These factors can be estimated based on the depth-to-diameter ratio and internal friction angle (Hansen 1961) as illustrated in Figure 2.7.

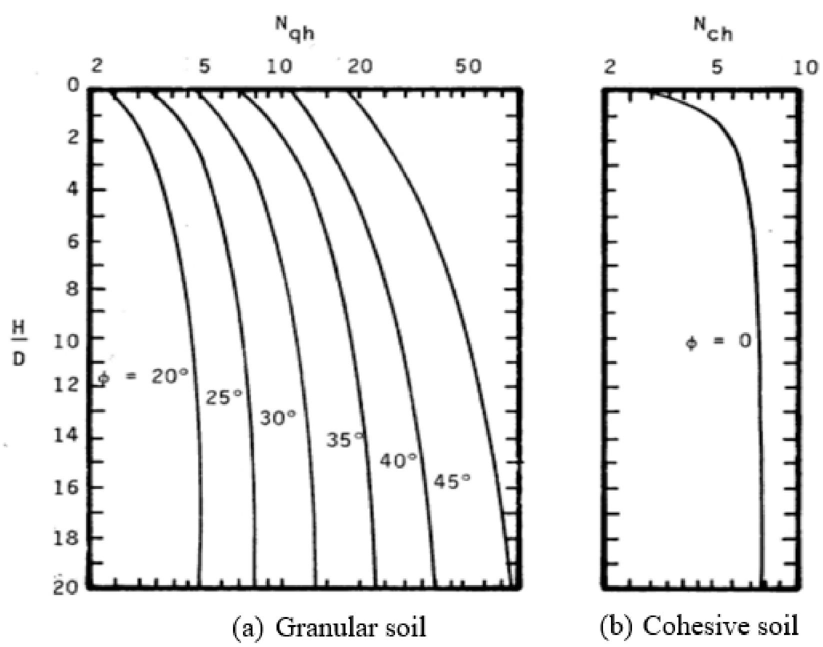

Figure 2.7: Horizontal bearing capacity factors (Hansen 1961)

The peak ground displacement required to achieve the ultimate lateral soil resistance can be estimated by the following formula (ALA 2005):

$$\Delta_p = 0.04\left(H + \frac{D}{2}\right) \leq 0.10D \text{ to } 0.15D \qquad (2.12)$$

2.5.3 Traverse-Vertical Upward Soil-Pipe Interaction

When the ground moves upward relative to the pipeline axis in the vertical plane, it establishes a force–upward displacement relationship at the interface. The guidelines provided by ALA (2005) present Equations (2.13) and (2.14) for estimating the ultimate soil resistance per unit length, which can be applied to the pipe:

$$Q_u = N_{qv}\bar{\gamma}HD \qquad \text{[for sand]} \qquad (2.13)$$

$$Q_u = N_{cv}c_u D \qquad \text{[for undrained clay]} \qquad (2.14)$$

where N_{qv} and N_{cv} are the vertical uplift factors for sand and clay, respectively. These factors are also soil-specific and depend on the pipeline's dimensions, specifically the ratio of the pipe burial depth to its diameter. Figure 2.8 shows the variations in vertical uplift factors with the depth-to-diameter ratio.

ALA (2005) suggests that the ground displacement at the peak resistances varies from $0.01H$ to $0.02H$ for dense to loose sand. However, the maximum value should be restricted to $0.1D$. For stiff to soft clays, the ground displacement at the peak force varies from $0.1H$ to $0.2H$ and must be limited to $0.2D$.

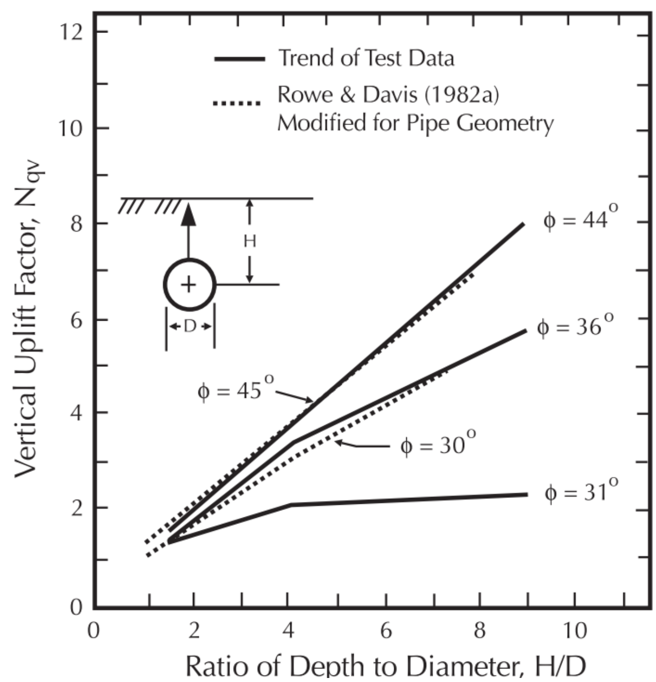

(a) Granular soil

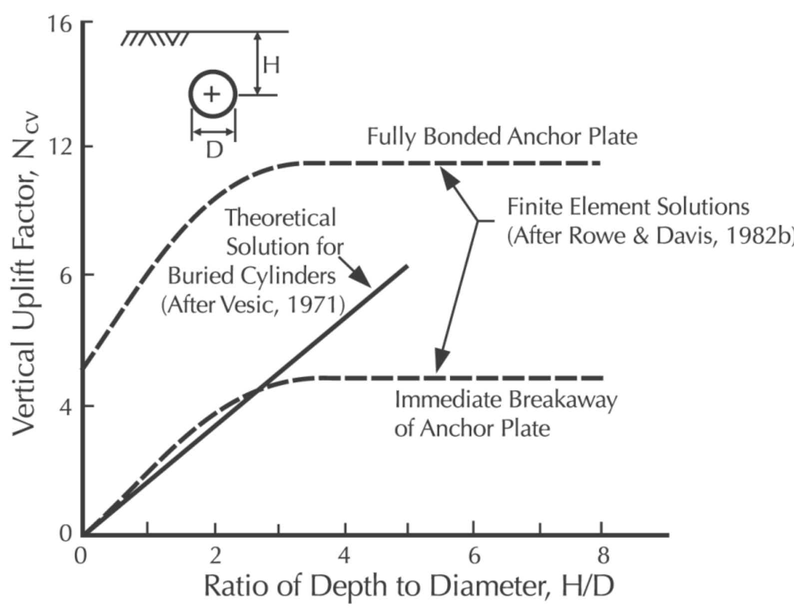

(b) Cohesive soil

Figure 2.8: Vertical uplift factors (ALA 2005)

2.5.4 Traverse-Vertical Downward Soil-Pipe Interaction

When there is relative ground movement perpendicular to the pipeline axis in the downward direction, it induces vertical forces at the interface. ALA (2005) provides the following equations to estimate the maximum vertical force per unit length of the pipeline:

$$\mathrm{Q_d} = N_q \bar{\gamma} H D + N_\gamma \gamma \frac{D^2}{2} \qquad \text{[for sand]} \qquad (2.15)$$

$$Q_d = N_c c_u D \qquad \text{[for undrained clay]} \qquad (2.16)$$

Here, γ is the total unit weight of soil, and N_q, N_γ, and N_c are the bearing capacity factors for horizontal strip footings.

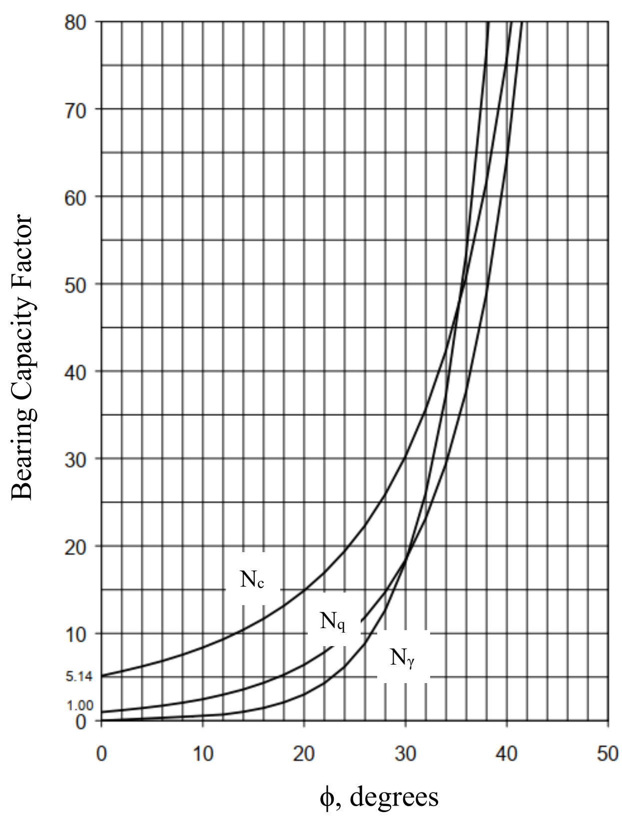

Figure 2.9: Bearing capacity factors (ALA 2005)

These factors can be estimated based on the friction angle as shown in Figure 2.9. ALA (2005) suggests the ground displacement corresponding to Q_d is 0.1D for granular soil and 0.2D for cohesive soil.

In recent decades, research on pipeline responses to PGD hazards has been conducted through a combination of laboratory experiments and numerical modeling. Notably, axial loading on distribution pipelines has received comparatively less attention based on the existing literature domain. However, the following sections will provide a detailed presentation of test results and numerical modeling, specifically focusing on axial soil-steel pipe interaction.

2.6 Full-Scale Laboratory Testing on Axial Soil-Steel Pipe Interaction

Wijewickrme et al. (2009) conducted full-scale laboratory testing on 457 mm diameter steel pipes. They used locally available 'Fraser River Sand' as backfill material in the study. The peak friction angle of Fraser River sand ranged from 43.5° to 45°. The pipes were pulled axially at 120 mm/min (AB-4, AB-5, and AB-6 tests) and 1200 mm/min (AB-3 test) for the initial loading phase to measure the axial soil loads (Karimian 2006). For tests AB-3, AB-4, and AB-6, the backfill sand was mechanically compacted (with a 200 mm lift thickness) to maintain a target relative density of 75% with moisture content less than 1%. The burial depth was chosen as 1140 mm (H/D = 2.5) for these tests. However, test AB-5 was conducted on uncompacted (loose) soil conditions, with a reported relative density of 20% and a burial depth of 1235 mm (H/D = 2.7). Tests AB-3, AB-4, and AB-5 were completed within a day after filling the soil tank. No noticeable effect of pulling rates on test results was reported. The peak normalized axial forces ($N_a = \frac{T_u}{\pi D H \bar{\gamma} L}$) for AB-3 and AB-4 tests were recorded as 1.02. Test AB-6 was conducted after 45 days of filling the soil tank to observe the aging effects of backfill soil on steel pipe response. An increase in peak axial force was observed for the AB-6 test, with the recorded peak normalized force being 1.13. The peak normalized axial force for the loose sand condition was approximately 0.42, but it dropped to 0.37 for a 175 mm pipe displacement. To compare the test results with the ALA approach, they chose the K_0 values as 0.37 and 0.42 for loose and dense sand conditions, respectively. Although the test result for loose sand showed 'good agreement' with ALA prediction, the dense sand test results indicated a significantly higher axial peak resistance than ALA prediction. As a solution, they proposed to use the K value instead of K_0, with the prediction that the K value would fall within the range of 1.8 to 2.2 for an interface friction angle of 36°.

Bilgin and Stewart (2009b) investigated the pullout resistance of the cast iron pipes within a trench measuring 1220 mm in width. The test pipe was collected from the field, and its surface was thoroughly cleaned before conducting the axial pull-out test. The average outside diameter of cast iron pipes was 175 mm, with a nominal diameter of 150 mm. The burial depth for the tests was set at 760 mm. For the loose backfill condition, sand was dumped in the trench without any compaction. The average dry unit weight of loose backfill was recorded as 14.76 kNm^{-3}, with an average moisture content of 5.3%. To achieve 95% relative compaction, the backfill soil was compacted in layers of 50-75 mm using a gas-operated mechanical jumper and hand tampers. Under these compacted conditions, the dry density and moisture content were reported as 18.4 kNm^{-3} and 5.8%, respectively. The results showed that the level of compaction had a noticeable impact on the shear resistance of the soil. The maximum shear resistance after the first 25 mm push was found to be 10.1 kPa for compacted backfill and 4.6 kPa for loose backfill conditions. Repeated pushes led to a decrease in peak shear resistance in both conditions. Furthermore, the researchers proposed a simple model to estimate the peak shear resistance for cast iron pipes. The peak shear resistance (in kPa) could be estimated as 6.0H, 9.3H, and 14.0H for loose, medium, and dense backfill conditions, respectively, with H representing the burial depth of the pipe in meters up to springline level.

Sarvanis et al. (2017) investigated the axial soil-pipe interaction on a 219.6 mm steel pipe buried at a depth of 750 mm. The pipe was pulled axially at a very slow and constant speed. Two different noncohesive soils were used in this study. 'Sand 1' had a peak friction angle of 45° and a peak dilation angle of 8°. In contrast, 'Sand 2' had a higher friction angle (48.2°) but a lower dilation angle (6.5°) than Sand 1. Both coated (AX3 test) and noncoated (AX1 and AX2 tests) steel pipe sections were used in their research. The test results showed that the axial pipe-soil interaction was significantly impacted by soil dilatancy. Notably, Sand 1 (AX1 test) exhibited higher axial resistance than Sand 2 (AX2 test). The maximum pulling force recorded during the AX1 test was around 33.5 kN, surpassing the recommended and current ASCE design guidelines. It was also clear from the test findings that the noncoated steel pipe (AX1 test) experienced greater axial pullout resistance than the coated one (AX3 test).

Sheil et al. (2018) conducted a study on a heavy steel pipe with a 350 mm diameter that had been buried in various trench conditions. To mitigate the boundary effects of the soil tank, the steel pipe was divided into three sections. The end pipe sections, each measuring 405 mm, were left uncoated, while the central section, with a length of 500 mm, was coated with Nap Gard7-2610 (R_{max} = 0.04 mm). They employed two different backfill soils, ‘Hostun HN31’ and ‘Sand K’, in their study. It was reported that Hostun sand had a higher peak friction angle compared to Sand K (37.9° vs 36.8°). Hostun sand was prepared by the ‘raining with no compaction’ method, maintaining a target relative density of 35% ± 2%. Sand K was collected from a field project site and directly dumped into the testing tank, maintaining a loose condition for the K1 test. However, a commercial plate compactor was used on Sand K (with a 100 mm lift thickness) to achieve a dense condition for the K2, K3, and K4 tests. The burial depths at pipe springline level were varied from 525 mm to 1355 mm under different overburden pressure conditions (0-83 kPa). The axial pipe pulling tests included both large-amplitude and small-amplitude cycle sets, with pulling rates of 14 mm/min and 4 mm/min, respectively, for the two sets of cycles. The normalized test results highlighted the significance of pipe weight, trench effect, and backfill compaction conditions on peak axial resistance. In the same narrow trench condition, pipe weight significantly contributed to total axial resistance in the H1 test, despite having a shallower burial depth compared to the H2 test. The trench effect was evident through the results of the H2 and H3 tests, showing a higher progressive normalized resistance in relatively narrower trench conditions. The findings of the study indicated that the normalized peak pullout resistances were 0.39 and 0.35 for the K2 and K3 tests, respectively, for the central pipe section. For the K1 test, there was no clear, identifiable peak pullout force observed during the initial 20 mm displacement (Cycle A) of the pipe. Nevertheless, the recorded normalized pullout resistance for the K1 test was approximately 0.48 for the coated section before reaching the peak, suggesting that the magnitude of the normalized pullout forces was influenced by the compaction level of the backfill soil. In addition, ALA predictions were also made by considering two different K_0 values (0.5 and 1) to compare with the test results. However, the variations in predicting the peak axial force were expected to arise because of the trench and the pinching effect.

Al-Khazaali and Vanapalli (2019) studied the axial force-displacement behavior of 114.3 mm buried steel pipe under various matrix suction conditions. The pipe surface was knurled, with a roughness (R_{max}) of 0.25 mm to enhance interlocking with the surrounding soil. The backfill material was poorly graded 'Unimin 7030 quartz silica' sand, manually compacted to maintain an average relative density of 69%. The peak and residual friction angles, measured using Direct shear tests, were 35.3° and 31.6°, respectively. It was believed that the mobilized axial skin friction was significantly affected by matrix suction and interface dilatancy. Test results indicated a linear increase in skin friction with matrix suction up to the Air Entry Value (AEV) in the boundary effect zone, followed by a non-linear trend in the transition and residual zones. The non-linearity became more pronounced after reaching the residual suction. However, the minimum skin friction (1.7 kN) was recorded when the soil was fully saturated. In unsaturated soil, the maximum axial skin friction occurred at a matrix suction value of 7.25 kPa, which was 2.5 times higher than that of saturated soil. Although the design guidelines typically assume a uniform distribution of skin friction along the pipe length, dilatancy was more pronounced in the compression zone under unsaturated conditions. This was primarily due to the large volumetric and shear deformation in the vicinity of the soil tank. Additionally, the study proposed two analytical approaches for predicting peak and residual skin friction, considering both matrix suction and interface dilatancy.

Murugathasan et al. (2021) investigated the pullout response of 178 mm diameter ductile iron pipes. The ductile iron pipes were subjected to axial pulling at rates of 1 mm/min (T5 test), 30 mm/min (T2, and T3 tests), and 60 mm/min (T1 test). They selected a burial depth of 690 mm for T1 and T2 tests and 825 mm for T3, T4, and T5 tests. Notably, the T4 test represented a loose backfill condition with no compaction. In contrast, for other tests, the backfill sand was manually compacted to achieve relative compaction levels ranging from 80% to 90%. Their findings indicated that the peak pullout force increased as the burial depth increased. They reported that the peak normalized pullout resistance ($N_a = \frac{T_u}{\pi D H \bar{\gamma} L}$) was approximately 1.0 for both T2 and T3 tests. Conversely, the peak normalized forces for medium dense (T1 test) and loose sand (T4 test) were reported as 0.86 and 0.36, respectively. They found that the ALA equation with a K_0 value of 0.42 provided a close match in predicting the peak axial pullout resistance for loose sand. However, significantly higher peak pullout resistances were observed for dense sand conditions, leading to the introduction of a K_1 value of 1.6 instead of K_0 in the ALA equation to match the test results.

Guo and Zhou (2024) investigated the effect of surface roughness and coating hardness on the pullout response of 102 mm hot-rolled seamless steel pipes. Three non-coated pipe segments (herein referred to as smooth, intermediate, and rough) and two coated pipe segments (FBE and EA surface treatments) were used in this study. The authors introduced a sleeve of 132 mm diameter at each pipe end to minimize boundary effects, resulting in a 0.7 m soil-pipe interaction zone. To prevent soil leakage, a rubber membrane (100 mm inner diameter and 1.5 mm nominal thickness) was inserted between the pipe and the sleeve. Five piezoresistive sensors were placed at different soil depths to measure vertical stress, while eighteen piezoresistive sensors were distributed across three sections of the pipe to measure contact pressure. The backfill material had a peak friction angle of 39.6° and a critical state friction angle of 32.8°. The backfill material was prepared using the pluviation method, maintaining a lift thickness of 25 mm. The dry unit weight of backfill material was 17 kN/m^3, maintaining a target relative density of 85%. The nominal pressure at the pipe crown varied from 17 to 50 kPa. The pipes were pulled at a constant speed of 1 mm/min to achieve a target displacement of 20 mm. For rough steel pipes (R_n = 1.01), the peak normalized force at the pipe springline level varied from 0.84 to 1.01, with a higher normalized force at the lower burial depth, indicating the more pronounced dilatancy behavior at lower pressure. For the intermediate pipe surface roughness (R_n = 0.21), the peak normalized force was reported as 0.63. No strain-softening behavior was observed for the smooth pipes (R_n = 0.04) due to limited dilatant behavior and the peak normalized force was almost one-third (0.30-0.35) of that for rough steel pipes. The epoxy asphalt (EA) surface-coated pipe (R_n = 0.01) behaved similarly to rough steel pipes (due to particle embedment), whereas the fusion-bonded epoxy (FBE) surface-coated pipe (R_n = 0.01) behaved similarly to smooth pipes (no embedment or scratches). The peak normalized forces at the pipe springline level for EA and FBE surface-treated pipes were 0.88 and 0.30, respectively. The authors reported that surface roughness increased the peak pullout resistance by 72-79%, whereas shear-induced dilation increased the resistance by 21-28%. The authors estimated the soil-pipe interface friction angle as 37.9° for rough, and 18.4° for smooth steel pipes from the Direct shear test under 17-100 kPa effective normal stress and reported that the change in friction coefficient (μ) from smooth to rough pipe was around 8 times higher than estimated from the design guidelines (1.34 vs. 0.17). For the rough steel pipes, the contact pressures at the invert and crown increased sharply due to constrained interface dilation during the axial pullout test. The maximum contact pressures at the invert and crown were reported as 70 kPa and 55 kPa, respectively, whereas the maximum increase in contact pressure was around 8 kPa at the pipe springline level. The FSRs also indicated a significant vertical soil pressure increase above (~45%) and below (~40%) the rough pipe and a slight decrease (~8%) in vertical pressure at the pipe sides for rough steel pipes. In contrast, the increase in contact pressure for smooth pipes was only observed at the pipe springline level. The authors proposed a new equation to estimate the maximum pullout resistance considering constrained interface dilation, self-weight of the pipe, and interface friction angle as a function of surface roughness.

Andersen (2024) explored the behavior of small-diameter steel pipes subjected to axial ground movement. In his tests, a soil mass was moved against a static pipe restrained at one end, while in most of the tests discussed above, the pipe is pulled through a static soil mass. The soil tank initially underwent a displacement of 35 mm at a rate of 0.5 mm/min, followed by a stationary phase. The peak normalized axial forces for his tests were significantly higher than those calculated using the method recommended in the current design guidelines. The current research is based on this study and explores further the effects of compaction on the behavior of the pipes.

2.7 Numerical Modeling of Axial Soil-Steel Pipe Interaction

Researchers employed numerical modeling to understand soil-pipe interaction during axial pullout. It was a general understanding that shear-induced dilation of the pipe-soil interface significantly influences the axial pulling force for pipes in dense sand. Wijewickrme et al. (2009) performed a 2D plain strain analysis by applying 0.7 to 1.0 mm radial expansion of a steel pipe to artificially apply the dilation effects on the pipes. The distribution of dimensionless normal stress obtained from their numerical modeling, particularly at and above the springline level, exhibited a favorable agreement with test results.

Sarvanis et al. (2017) performed a 3D FE analysis where the soil was modeled as 8-node linear 'brick' elements (C3D8R) and the steel pipe as 4-node 'shell' elements (S4R). They utilized a modified Mohr-Coulomb plasticity model to account for post-peak response. They developed a contact algorithm considering the dilatancy effect and implemented it in ABAQUS to simulate the interface behavior. Their parametric study on strike-slip crossing configuration suggested using a 'bilinear friction law' corresponding to peak or residual friction value to predict the actual behavior.

Meidani et al. (2018) used 3D discrete element analysis to explore the behavior of buried steel pipe under axial ground movement. The sand particles were modeled using 265,000 homogenous spherical particles with up-scale factors of 90 and 140. The smaller upscale factor was specifically applied to simulate the soil particles in close proximity to the pipe, enhancing the accuracy of the contact between the soil and the pipe. For the pipe, a configuration of 1,216 facet discrete elements arranged in a hexdecagonal pattern was employed. A parametric study on the friction angle of facet elements revealed that a 30° friction angle yielded numerical results closely aligned with experimental findings. They also recommended the use of a modified earth pressure coefficient (K^*) instead of the earth pressure coefficient (K), based on their parametric investigation involving pipe burial depth, friction angle, soil Young's modulus, and pipe diameter.

Murugathasan et al. (2021) utilized 3D finite element analysis to study the influence of dilation on the peak pullout force for ductile iron pipes. They modeled the soil and the pipe as deformable bodies using 8-node reduced integration 'brick' (C3D8R) elements to simulate the soil and the pipe. They employed a conventional Mohr-Coulomb plasticity model for simulating the peak soil-pipe interface frictional resistance. This study focused on evaluating the 'average normal stress' around the pipe circumference. The circumferential distribution of normal stress indicated increased stress at the pipe crown and invert, attributed to a 'negative arching effect'.

2.8 Summary of Key Observations

This chapter provides a brief overview of the response of buried steel pipes under axial ground movement conditions. The following observations can be drawn from the research studies presented above on axial soil loads:

- The response of buried steel pipes in loose sand conditions aligns well with predictions from design guidelines. However, in dense sand conditions, there is an underprediction of soil resistance by the design guidelines.

- The underprediction of soil resistance in dense sand conditions is likely attributable to the increase in average normal stress, which is linked to the dilatancy effect within the interface shearing zone.
- Researchers commonly recommend using a modified earth pressure coefficient instead of the traditional earth pressure coefficient to account for dilation-induced normal stress increase. This modified coefficient is a function of pipe burial depth, friction angle, soil Young's modulus, and pipe diameter.
- The axial load–displacement behavior of buried steel pipes may be influenced by matrix suction. The transferred axial load from the soil onto the pipe under unsaturated conditions is found to be several times higher than under saturated conditions.

In response to the insights derived from the above observations, a new test facility developed at Memorial University of Newfoundland was used in the current study to explore the behavior of steel pipes subjected to axial ground movements. The facility is specifically designed to investigate the response of buried distribution pipes by restraining one end of the pipe while enabling axial movement of the soil mass. Full-scale laboratory testing on steel pipes with diameters of 26.7 mm, 60.3 mm, and 114.3 mm was conducted under axial ground movement conditions. This study aims to enhance the fundamental understanding of the soil-pipe interaction and collect valuable data to improve the design guidelines, thus contributing to advancements in pipeline design.

Chapter 3: Full-Scale Laboratory Testing on Small-Diameter Steel Pipes

3.1 Abstract

This Chapter investigates the axial soil resistance of small-diameter steel pipes in compacted sand. The structural integrity of buried pipelines can be threatened each time a ground deformation event occurs along the pipeline route. In general, the effects of axial ground movement on buried steel pipes are investigated in the laboratory or field by pulling a pipe through static soil masses. However, a soil mass moves during landslides when the pipe can be restrained on stable ground. No study investigates the axial force on a static pipe against moving soil. Besides, while most of the studies focused on large-diameter transmission pipelines, small-diameter pipes are frequently used as distribution lines for transporting natural gas to consumers within local communities. Test results for small-diameter pipes are also not available in the public domain. Furthermore, pipe backfills are often compacted using different compaction methods when pipelines pass closer to any infrastructure or beneath road pavements. The effect of the compaction method on pipe behavior has not been studied before. This study conducted full-scale laboratory tests on 26.7 mm, 60.3 mm, and 114.3 mm diameter steel pipes using the test facility developed at the Memorial University of Newfoundland. The backfill soils were compacted using either a vibratory plate compactor or a hand tamper to achieve the target soil density. The relative axial displacement between the pipe and soil was applied by moving the soil box at a constant rate while keeping the pipe fixed at one end. During testing, axial strain at the pipe's restrained end was monitored using a discrete strain gauge, and pipe elongation was measured using LVDTs attached to both ends. The results highlight the significant impact

of the compaction technique on measured axial resistance, indicating higher resistance in tests compacted with a vibratory plate compactor. The difference in resistance between the two methods increases with pipe diameter, likely due to the higher compaction-induced stresses acting around the perimeter of the pipe.

3.2 Introduction

Buried pipelines are often considered safe, durable, and energy-efficient mediums for transporting crude oil and natural gas across the nation. According to the Pipeline and Hazardous Materials Administration (PHMSA 2015), the choice of materials for pipelines is based on the fluids they transport, service requirements, and operational conditions. The majority of gathering and transmission pipelines are made of steel, while the primary material for distribution lines is plastic.

Recent years have witnessed a significant number of pipeline incidents across North America. According to the Transportation Safety Board of Canada (TSB 2024), there were 68 reported pipeline incidents in 2023 involving federally regulated pipelines routing over 73,000 kilometers. The primary reasons behind pipeline ruptures and leaks include external interferences, corrosion, manufacturing and construction defects, as well as natural hazards such as erosion, flooding, and landslides (Ferreira and Blatz 2021). In 2023, PHMSA reported about 60 gas distribution pipeline incidents in the United States. These failures resulted in 21 fatalities and 30 injuries, with a total cost of $39.5 million.

Permanent ground deformation (PGD), such as lateral spreading, surface faulting, landslides, soil creep, and seismic settlement, is reported to be one of the major causes of structural damage to pipelines and associated service failures in post-incident analysis (O'Rourke et al. 1991). Historical seismic events have clearly shown the significant vulnerability of the gas and water distribution systems to earthquakes. For example, the 1989 Loma Prieta M6.9 earthquake in San Francisco resulted in the failure of 25 distribution mains due to liquefaction and subsequent slope failure (Eguchi and Seligson 1994). In 1994, Balboa Boulevard, California, faced an M6.7 seismic event that ruptured a 168-mm diameter steel distribution main due to block-type longitudinal soil displacements (Bain et al. 2024), as shown in Figure 3.1. Similarly, during the 1995 Hyogoken-Nambu M7.2 earthquake, most water pipeline failures occurred in smaller-diameter pipes (Kitaura and Miyajima 1995). The 2020 Magna M5.7 earthquake also caused significant damage, including the leakage of 1 polyethylene main (50 mm), 11 lateral service branch pipes (25 mm or smaller), and 468 gas meter components (Eidinger et al. 2023). These incidents highlight the importance of vulnerability assessments for the integrity of the distribution pipelines subjected to PGD.

Pipe responses (e.g., pipe wall strain) to ground movements are generally calculated using beam-on-spring analysis for a known (measured) ground displacement (ALA 2005, PRCI 2017). The soil springs in the three orthogonal directions (axial, lateral, and vertical) are characterized by the elastic-perfectly plastic soil parameters. The axial spring parameter is defined using Equation (3.1) to calculate the ultimate axial force per unit length on the pipe (T_u) due to axial ground movement in cohesionless soil, as follows:

$$T_u = \pi D H \bar{\gamma} \frac{1+K_0}{2} \tan\delta \qquad (3.1)$$

where H is the pipe burial depth, K_0 is the coefficient of earth pressure at-rest condition, $\bar{\gamma}$ is the effective unit weight of soil, and δ is the interface friction angle for soil and pipe.

Figure 3.1: Pipeline failure during the 1994 Northridge earthquake (USGS 2021)

Several studies have confirmed that the ultimate soil resistance in loose sand conditions can be accurately predicted using Equation (3.1) (Bilgin and Stewart 2009, Wijewickreme et al. 2009, Murugathasan et al. 2021). However, Equation (3.1) has been reported to underpredict the axial pullout resistance measured in laboratory and field tests for pipes buried in dense sand. The higher pullout resistances observed during the experiments are mainly attributed to the soil dilation caused by shearing at the interface between the pipe and the soil (Wijewickreme et al. 2009). To address this issue, Wijewickreme et al. (2009) proposed using the equivalent lateral earth pressure coefficient, K, rather than K_0 in Equation (1). Following the findings reported by Wijewickreme et al. (2009), PRCI guidelines recommended using K as high as 2.0 in Equation (3.1) for pipes buried in dense sand conditions.

Despite this, note that backfill materials for distribution pipes are typically compacted to reduce adverse effects on nearby infrastructure, such as highway embankments. The backfill compaction has a significant impact on the stress fields surrounding the pipe (Moore and Taleb 1999, Dezfooli et al. 2014, Wang et al. 2015, Prabhu et al. 2020). Several compaction techniques, including hand tamping, mechanical jumping, surface vibration, and rolling, are generally used to compact the backfill material. ASTM D2321-20 specifies the embedment compaction methods for flexible thermoplastic sewer pipes for Class I (manufactured aggregate, i.e., crushed stone) and Class II (clean sand and gravel) materials. In gas distribution pipeline construction, the backfill surrounding the pipe is usually compacted using hand tampers or light compaction equipment to prevent pipe damage and ensure uniform compaction around the pipe. Compressed air tampers or hand tampers are often used in the haunch zone to ensure firm contact with the entire bottom of the pipe (Jayawickrama et al. 2001, PPI 2008, NCSPA 2018). Previously, it was found that for shallowly buried pipes, soil compaction caused additional horizontal earth pressure on the pipe wall (Wang et al. 2015). However, at larger depths, the horizontal earth pressure converged to Jaky's state of stress (i.e., at-rest condition). Duncan et al. (1991) also developed earth pressure charts and tables for different compaction equipment to estimate the compaction-induced horizontal pressure at various depths. Therefore, it is necessary to understand how compaction methods affect the distribution pipeline during placement and their potential effects on the pipe's response to ground movements.

In recent years, many laboratory experiments have been performed to investigate the effects of axial ground movement on buried steel pipes. Most of the studies focused on large-diameter steel pipes, and only a few focused on small-diameter distribution mains (Karimian 2006, Bilgin and Stewart 2009, Wijewickrme et al. 2009, Sarvanis et al. 2017, Sheil et al. 2018). Typically, laboratory idealizations involve axially pulling pipes through stable soil masses. However, in real field conditions, the pipeline is often fixed in stable ground, whereas the soil mass moves along its length. Furthermore, bends, thrust blocks, or other anchors can also restrain pipe movement. The pipeline encounters soil load at the interface when unstable soil masses move. A full-scale laboratory test facility was developed at Memorial University of Newfoundland to address this. The facility allows relative ground movement by restraining one end of the pipe while enabling axial movement of the soil mass, as illustrated in Figure 3.2. In this study, steel pipes with diameters of 26.7 mm, 60.3 mm, and 114.3 mm were examined under axial ground movement conditions. Two compaction techniques, hand tamping and vibratory plate compaction, were employed to examine the significance of the compaction process in the pipeline behavior of PGDs.

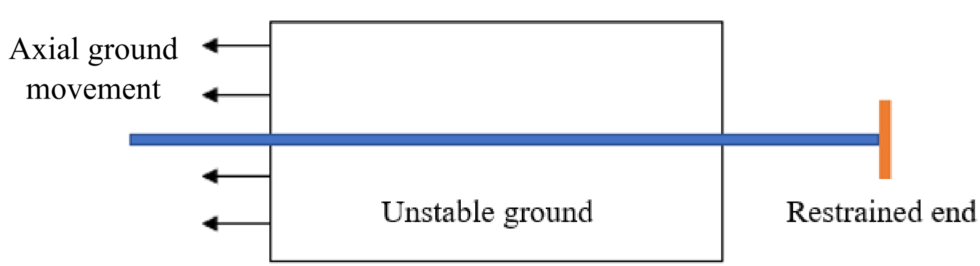

Figure 3.2: Laboratory idealization of axial ground movement

3.3 Experimental Program

3.3.1 Pipes and Backfill Material

In this study, locally manufactured, well-graded sand was used as the backfill material. The sand had a fines content of 1.3% and a gravel content of 0.87%. The maximum dry density, determined through the Standard Proctor compaction test (ASTM D698-12), was measured as 18.8 kN/m^3. The mechanical properties of the sand were determined using the direct shear test and triaxial test and documented in Saha (2021). It was reported that the peak friction angle of the soil varied with moisture content. The optimum moisture content for this sand was found to be 0% (Saha et al. 2019). It was observed that the dry density initially decreased with increasing moisture content, reaching a minimum at 4%, attributed to the dominance of capillary tension over the lubricating effect of water. The properties of the sand are summarized in Table 3.1.

Table 3.1: Physical properties of the sand (after Saha et al. 2019)

Property	Value
Mean particle size, D_{50} (mm)	0.742
Uniformity coefficient, C_u	5.81
Coefficient of curvature, C_c	2.04
Specific gravity, G_s	2.63
Peak friction angle (dry condition), ϕ (°)	49
Critical state friction angle, ϕ_{cv} (°)	35

Steel pipes with three different diameters, typically used for natural gas distribution networks, were used in the present study. The mass density of steel pipes was 7850 kg/m^3. Various physical and mechanical properties of the control lot, as provided by the manufacturer, are summarised in Tables 3.2 and 3.3.

Table 3.2: Physical properties of steel pipes

Diameter (mm)	Schedule	ASTM standard	Wall thickness (mm)
26.7	XH	A106B	3.912
60.3	STD	A106B	3.912
114.3	STD	A53	6.020

Table 3.3: Mechanical properties of steel pipes

Property	Value
Young's modulus (GPa)	210
Yield strength (MPa)	373
Tensile strength (MPa)	529
Elongation (%)	32
Hardness test (Scale: HV)	150
Absorbed energy (J)	31

3.3.2 Test Facility

A full-scale laboratory test facility has been developed at Memorial University of Newfoundland, St. John's, NL. This facility was designed to allow the soil tank to move against a pipe restrained at one end, thus simulating a landslide scenario. The test facility includes a steel box (inside dimensions of $4.0 \times 2.0 \times 1.5$ m), an actuator to pull the steel tank using hydraulic controls, a data acquisition system, and instrumentation to record the responses. To control lateral soil movement, the rigidity of the steel box is increased by adding vertical and horizontal stiffeners to the outside wall. The effect of the boundary wall of the current facility on the pipe response under axial ground movement was found to be negligible (Murugathasan 2021). Each side of the shorter wall (i.e., the 2.0 m wall) has an adjustable circular opening, fitted with a steel plate and rubber gasket, to allow for the proper placement and alignment of the steel pipes. The frictional resistance of the rubber gasket was found to be negligible (Reza and Dhar 2021). Further details on the test facility can be found in Andersen (2024).

The pipe is restrained at one end within the back-stop frame and connected to a load cell. The other end remains unrestrained and is attached to a linear velocity displacement transducer (LVDT) to monitor the axial pipe movement. Despite the pipe being restrained at the back-stop frame, an additional LVDT was placed behind the frame to monitor whether the restrained end of the pipe moves with the frame during soil tank displacement. The elongation of the pipe could then be precisely measured by comparing the readings of the two LVDTs. The schematic diagram of the test facility is illustrated in Figure 3.3.

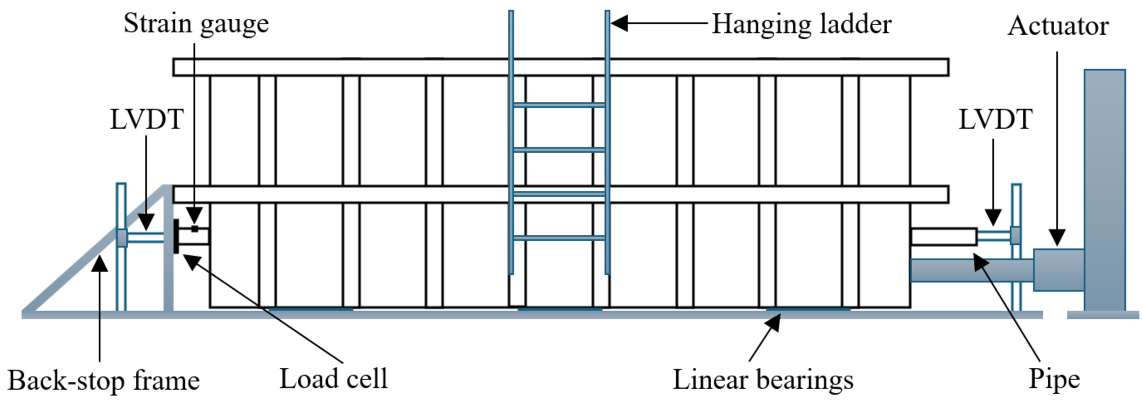

Figure 3.3: Schematic diagram of the test facility

3.3.3 Test Preparation

The steel pipes were directly placed on the prepared bed, aligned parallel to the longer side of the test box, and passed through its adjustable circular openings. The straightness of the pipe was confirmed using a 1.0 m long spirit level. The backfill material was deposited using sandbags into the tank, maintaining a drop height of 1.5 m with an overhead crane. A wooden spreader was used to evenly spread the sand, keeping a lift thickness of 130–160 mm. The backfill sand was compacted in each layer using either a customized hand tamper or a vibratory plate tamper, with the moisture content targeted to 1–1.5% to minimize dust in the lab environment. The burial depth (measured from the pipe springline to the soil top surface) for the pipes was 625 mm for all tests, which is a typical soil cover used in the gas distribution network in Canada. An illustration of backfilling and pipe placement is shown in Figure 3.4.

(a)

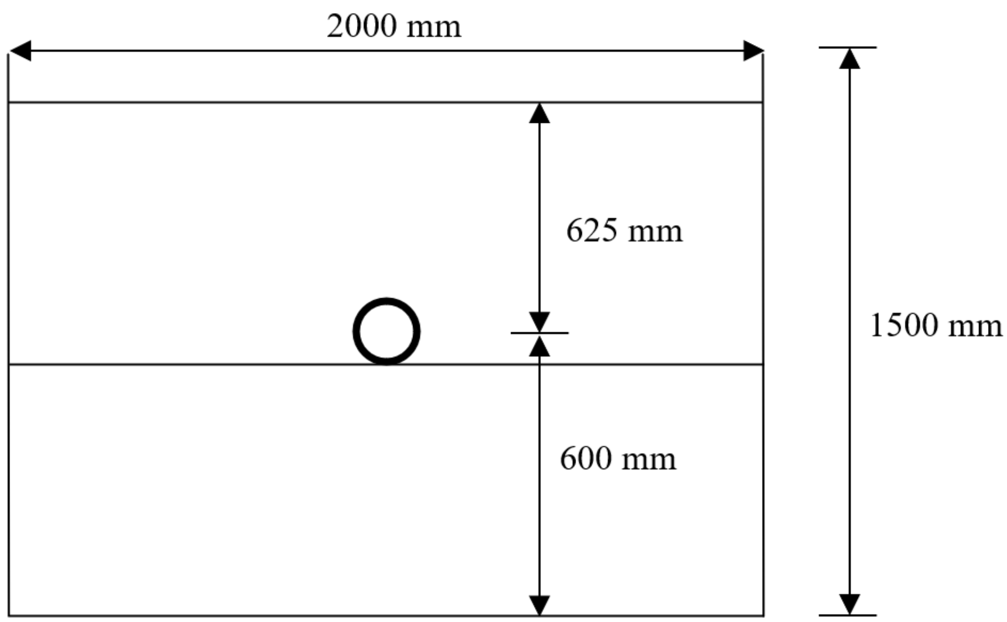

(b)

Figure 3.4: Pipe placement (a) on the bedding ; (b) cross-sectional view

The hand tamper used to compact the backfill weighed approximately 4.5 kg, with a steel base plate size of about 287.5 × 112.5 mm. It was dropped freely twice in an alternative pattern from a height of approximately 125–150 mm at each location within a layer to ensure uniform compaction of the backfill soil. The sand-cone method (ASTM D1556) was used to measure the density of backfill material at the top surface. The average dry unit weight of the backfill soil was found to be 17.5 kN/m^3. Additionally, a battery-powered, single-direction vibratory plate compactor (Model: Wacker Neuson APS 1135e) was used in separate sets of tests to assess the effect of the compaction technique on the pipe's response to movement (Figure 3.5). This method yielded an average dry unit weight of 17.9 kN/m^3. It is important to note that the relative compaction (Standard Proctor) did not significantly differ between the two different compaction methods, with values reaching around 93% for the hand tamper compaction and 95% for the vibratory plate compactor.

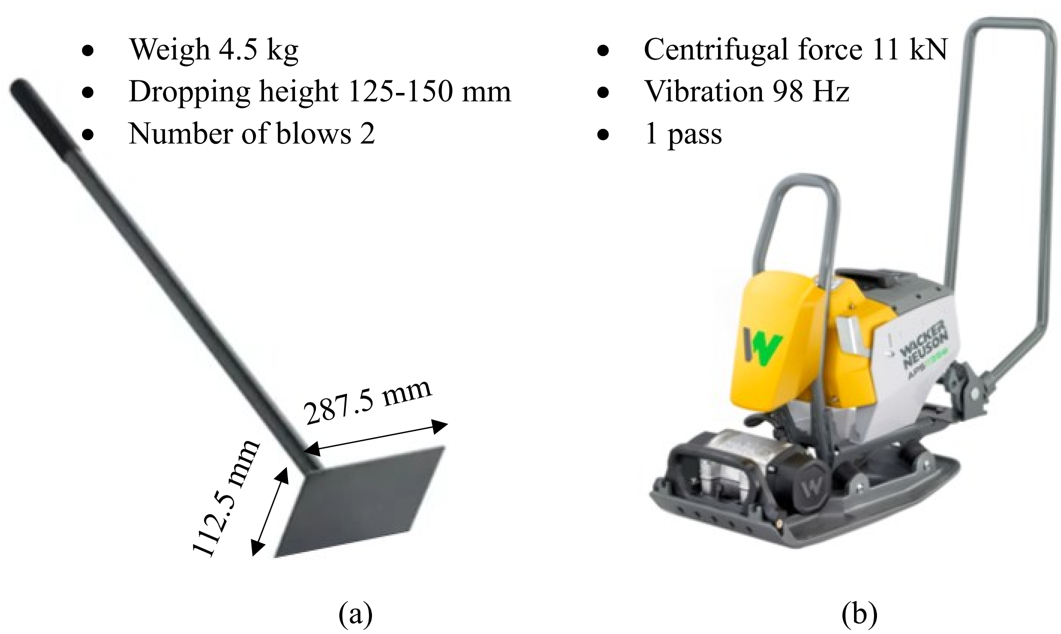

Figure 3.5: (a) Hand tamper; (b) Vibratory plate compactor

To prepare the backfill conditions for loose sand, the sand was poured into the tank and spread with no compaction at all. The average dry unit weight of loose backfill was measured to be 14.2 kN/m^3. The laboratory minimum density tests, conducted according to ASTM D4253-00 (Method 1A) guidelines, provided the dry unit weight of the sand at its 'loosest' state as 16.6 kN/m^3. The difference may be due to different water content in pipe backfill and minimum density tests. The sand used in the minimum density tests was dry. However, the backfill material in the test facility had a moisture content of around 1.2%. This indicates that the field density of sand can be less than the minimum density obtained using standard laboratory tests. Thus, the relative density defined based on the laboratory minimum and maximum density tests can sometimes be misleading. Note that the density measured using the sand cone method can also be affected by the shape and depth of the excavated hole (Park 2010).

Although pipelines can be routed through the 'dormant' to 'very slow' ground-moving zones (Porter et al. 2022), in the current study, a 'moderate' ground-moving (0.3–30 mm/min) zone was chosen considering the feasibility in lab settings. Three distinct ground movement rates (0.5 mm/min, 1 mm/min, and 2 mm/min) were chosen to monitor the response of buried pipelines to ground movement rates. The steel pipe was restrained at one end while free at the other. The soil tank was pulled at the specified rates for 30 mm of displacement towards the unrestrained end of the pipe. The peak pullout force was observed within the displacement of 30 mm. One uniaxial strain gauge (length 5 mm and resistance 119.8 ± 0.2 Ω) was installed at the pipe crown in the restrained end (i.e., outside of the test box) to monitor the variation of strains for compacted and loose sand conditions with the soil tank movement. The details of the test program are shown in Table 3.4.

Table 3.4: Test configuration

Test ID	Diameter (mm)	Pulling rate (mm/min)	Compaction method
Test-1	26.7	0.5	Hand Tamping
Test-2	60.3	0.5	Hand Tamping
Test-3	114.3	0.5	Hand Tamping
Test-4	114.3	0.5	Uncompacted
Test-5 (Andersen 2024)	26.7	0.5	Vibratory Plate
Test-6 (Andersen 2024)	60.3	0.5	Vibratory Plate
Test-7 (Andersen 2024)	114.3	0.5	Vibratory Plate
Test-8	26.7	2.0	Hand Tamping
Test-9	60.3	1.0	Hand Tamping
Test-10	60.3	2.0	Hand Tamping
Test-11	114.3	2.0	Hand Tamping
Test-12	26.7	2.0	Vibratory Plate

3.4 Results and Discussion

3.4.1 Force–Displacement Response

Figure 3.6(a) represents the force–displacement responses of buried steel pipes obtained from Tests 1–3. As the soil tank moves against the static pipe, axial force is applied to the pipe, resulting from interface friction. The axial force gradually increases as the soil moves until the interface bond is completely broken (i.e., the shear strength of the interface soil is fully mobilized). The axial force reaches its peak value when the shear strength is mobilized over the full pipe length. Beyond the peak, the axial force decreases and would probably reach a residual value at a larger displacement. The axial forces beyond the peak value would be affected by the length of the pipe sample and, therefore, are not the focus of the current study. Note that all the peak pipe axial forces are achieved within 6 to 8 mm of tank displacement. After the peak load, the axial resistances decreased nearly 30% in all three tests for an additional 22 to 24 mm of tank displacements.

As seen in Figure 3.6(a), the axial force is higher for pipes with larger diameters due to a larger contact area at the interface. The weight of the pipe could also contribute to the higher force, resulting in higher shearing resistance of the interface soil. Figure 3.6(b) plots the nondimensional force N_a against soil displacement for Tests 1–3 to eliminate the effect of contact area. The force was normalized by pipe diameter, burial depth, buried pipe length, and soil density according to Equation (3.2), as below.

$$N_a = \frac{T_u}{\pi D H \bar{\gamma} L} \qquad (3.2)$$

where Tu is the axial force of the pipe, and L is the buried pipe length. The rest of the parameters in Equation (3.2) are defined earlier.

Figure 3.6(b) reveals that the peak N_a is higher for the 26.7 mm diameter pipe (N_a = 2.81), indicating that the shearing resistance of the interface soil is relatively higher for pipes with smaller diameters. It might be due to a larger dilation of the interface soil for the small-diameter pipes (Reza et al. 2023). During shearing, dense sand tends to dilate (expand radially in the current case), which is resisted by the surrounding soils, resulting in a higher normal pressure on the pipe surface. According to the elastic cavity expansion theory (Boulon and Foray 1986, Johnston et al. 1987), the increase in normal pressure on the pipe due to soil dilation is inversely proportional to the pipe diameter.

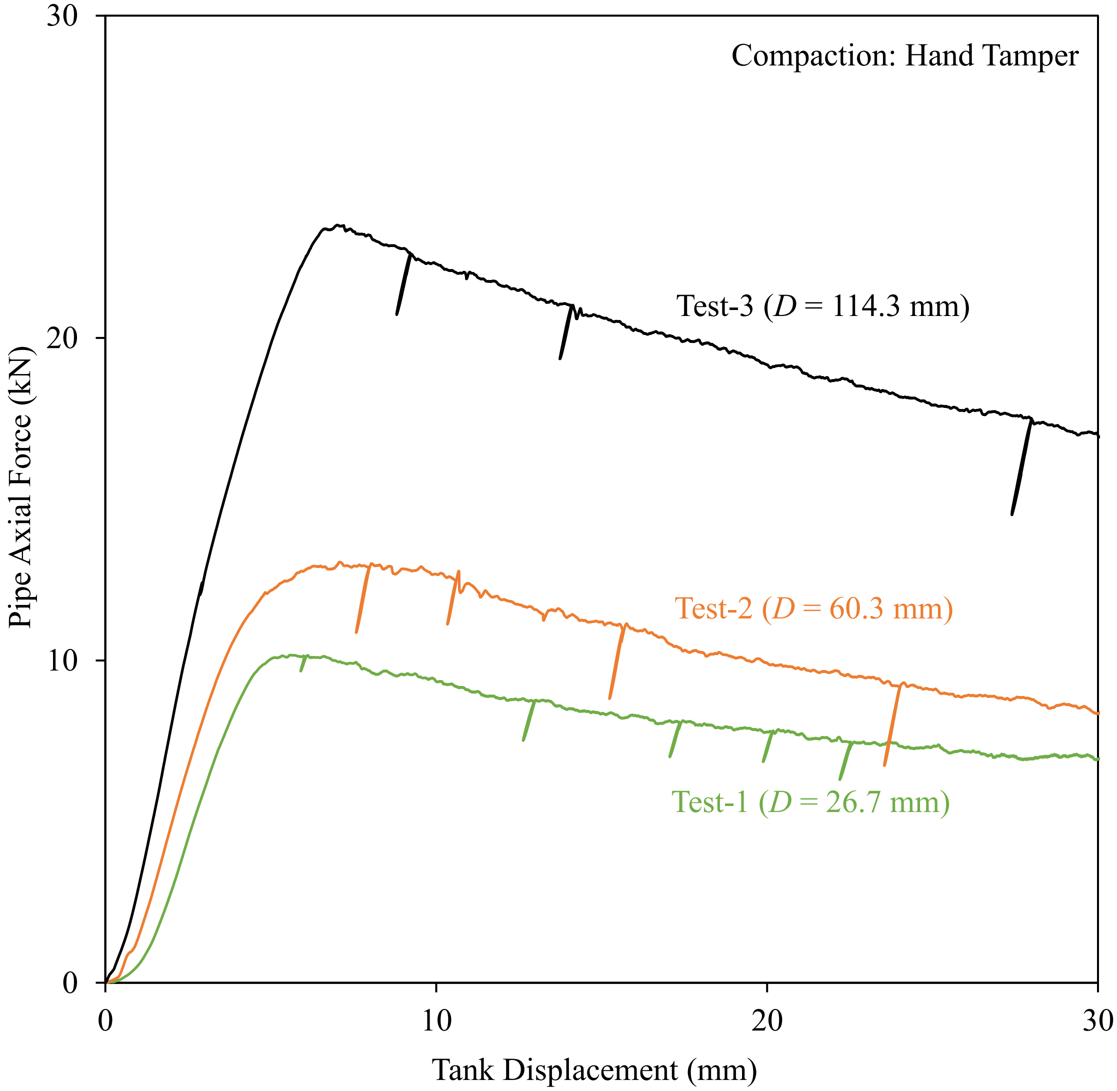

(a)

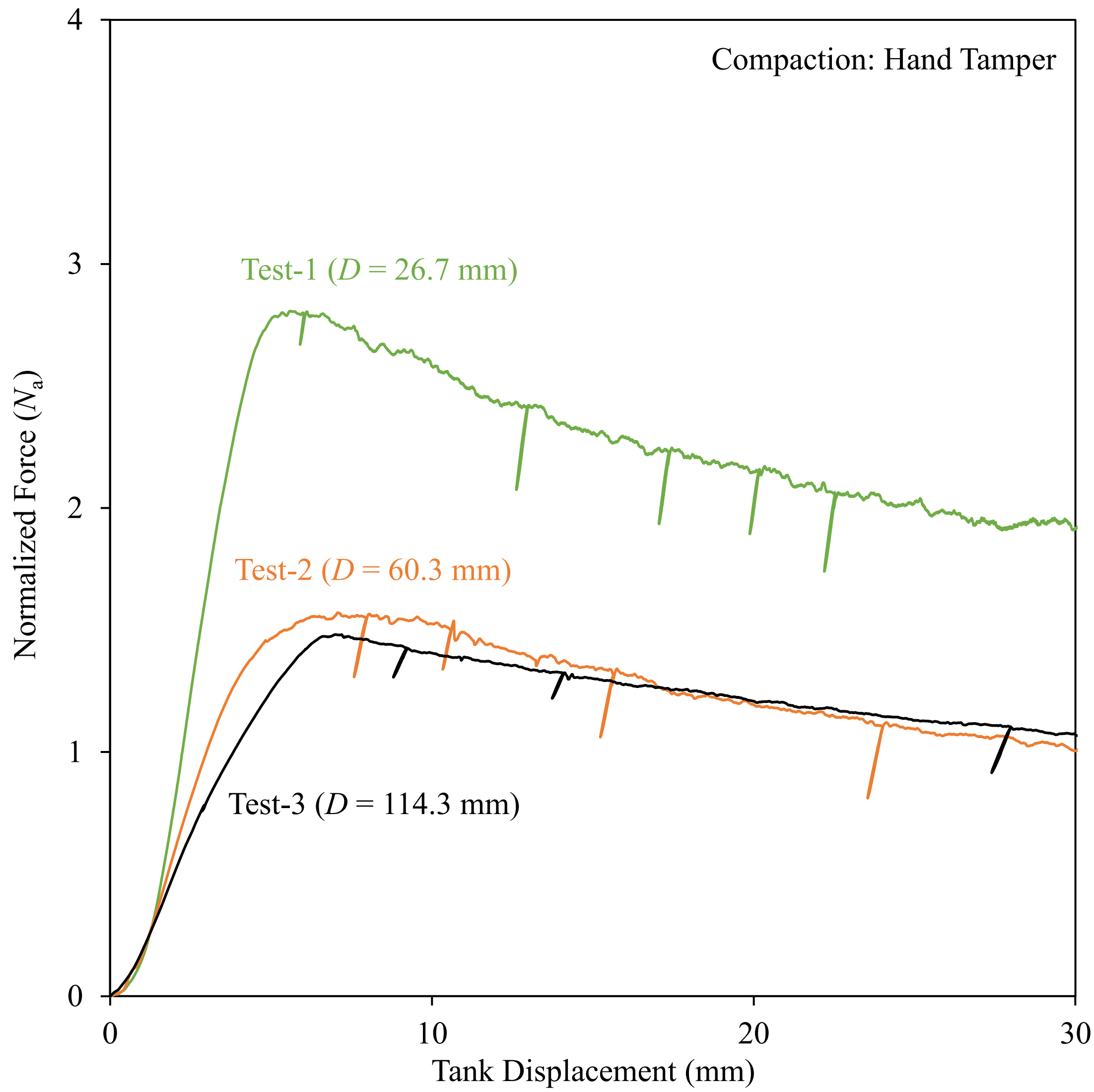

(b)

Figure 3.6: (a) Force–displacement response; (b) Normalized force–displacement curve

A similar observation was found from numerical modeling performed by Meidani et al. (2018). The peak normalized forces for the 60.3 mm and 114.3 mm pipes are calculated as 1.57 and 1.48, respectively. Sarvanis et al. (2018) and Wijewickrme et al. (2009) conducted axial pullout tests of 219.6 mm and 457 mm diameter steel pipes and found the peak normalized forces as 1.30 and 1.02, respectively. The lower peak normalized forces for larger diameter pipes are attributable to the relatively lower normal stresses acting on the pipe from soil dilation. Note that a pipe was pulled against static soil in Sarvanis et al. (2018) and Wijewickrme et al. (2009), while a soil mass was moved against a static pipe in the tests conducted in this study.

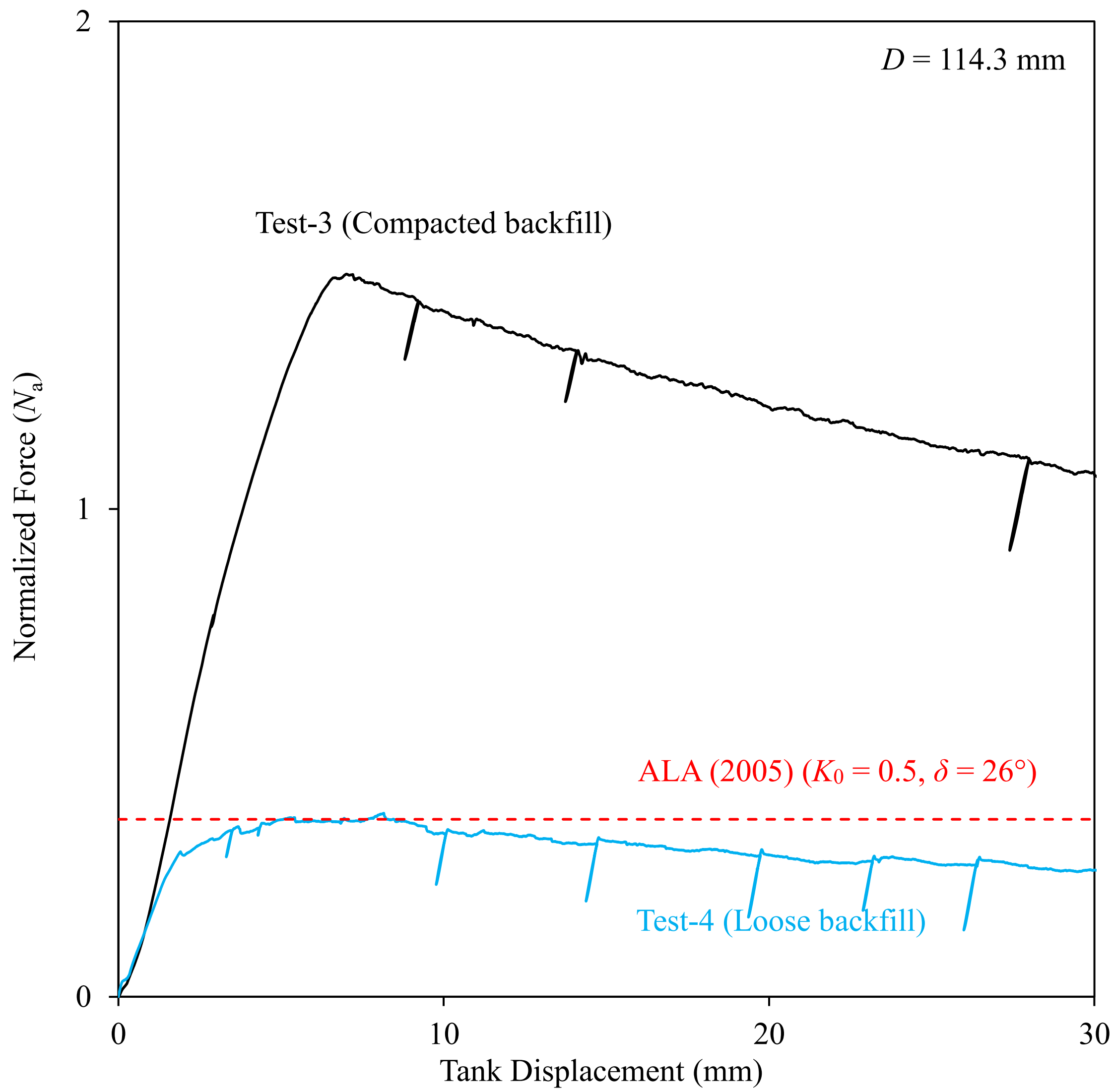

Figure 3.7: Normalized force vs. tank displacement

Figure 3.7 compares the nondimensional force–displacement responses for 114.3 mm pipe in loose backfill (Test-4) and dense backfill (Test-3). For Test 4, the peak normalized force is calculated as 0.38, which is one-fourth of the peak normalized force observed for dense backfill. The figure also shows that the current design guideline provides a close match for predicting the peak normalized axial force in loose sand. Similar observations were also reported by Wijewickrme et al. (2009) and Sheil et al. (2017), who pulled pipes through static soil. Thus, the test results based on pulling a pipe through static soil and pulling a soil mass relative to a static pipe are not significantly different in terms of maximum pulling force for the steel pipes investigated in loose sand. Information for pipes in dense sand is not available for comparison.

3.4.2 Effects of Backfill Compaction

The effect of the different compaction techniques on the axial soil resistance in the present study is illustrated in Figure 3.8(a). Tests 1–3 correspond to the backfill compaction with the hand tamper, while in Tests 5–7, a vibratory plate compactor was used to compact the backfill soil. Although the relative compaction (R) between Tests 1–3 and 5–7 was similar, the impact of the vibratory plate compactor on increasing the soil axial resistance is clearly evident for the pipes tested.

Figure 3.8(b) plots the peak normalized force (N_a) with pipe diameters for Tests 1–3 and 5–7. As seen in the figure, for pipes with diameters of 26.7 mm, 60.3 mm, and 114.3 mm, the vibratory plate compactor increases the peak normalized force by 27%, 64%, and 67%, respectively, compared to those from the hand tamper compaction. The increase is significantly higher for 60.3 mm and 114.3 mm pipes than for 26.7 mm pipes. This might be due to the lateral forces generated by the backfill compaction increasing with the middle arc section area of the pipes, as mentioned in Masada and Sargand (2007). However, the rate of increase does not differ significantly for 60.3 mm and 114.3 mm pipes due to the difficulty in compacting the backfill soil in the haunch zone and above the shoulder zone for larger pipes.

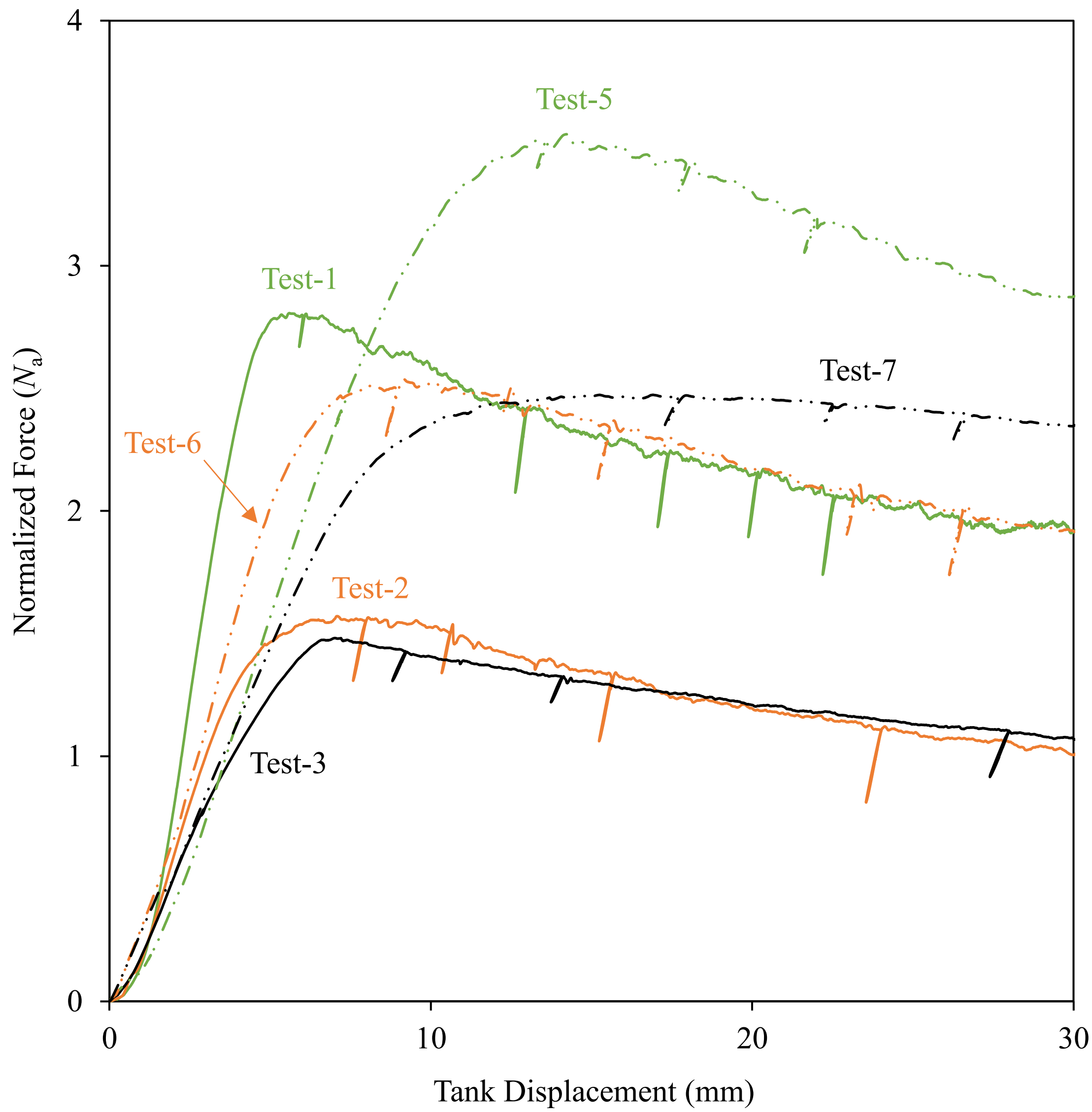

(a)

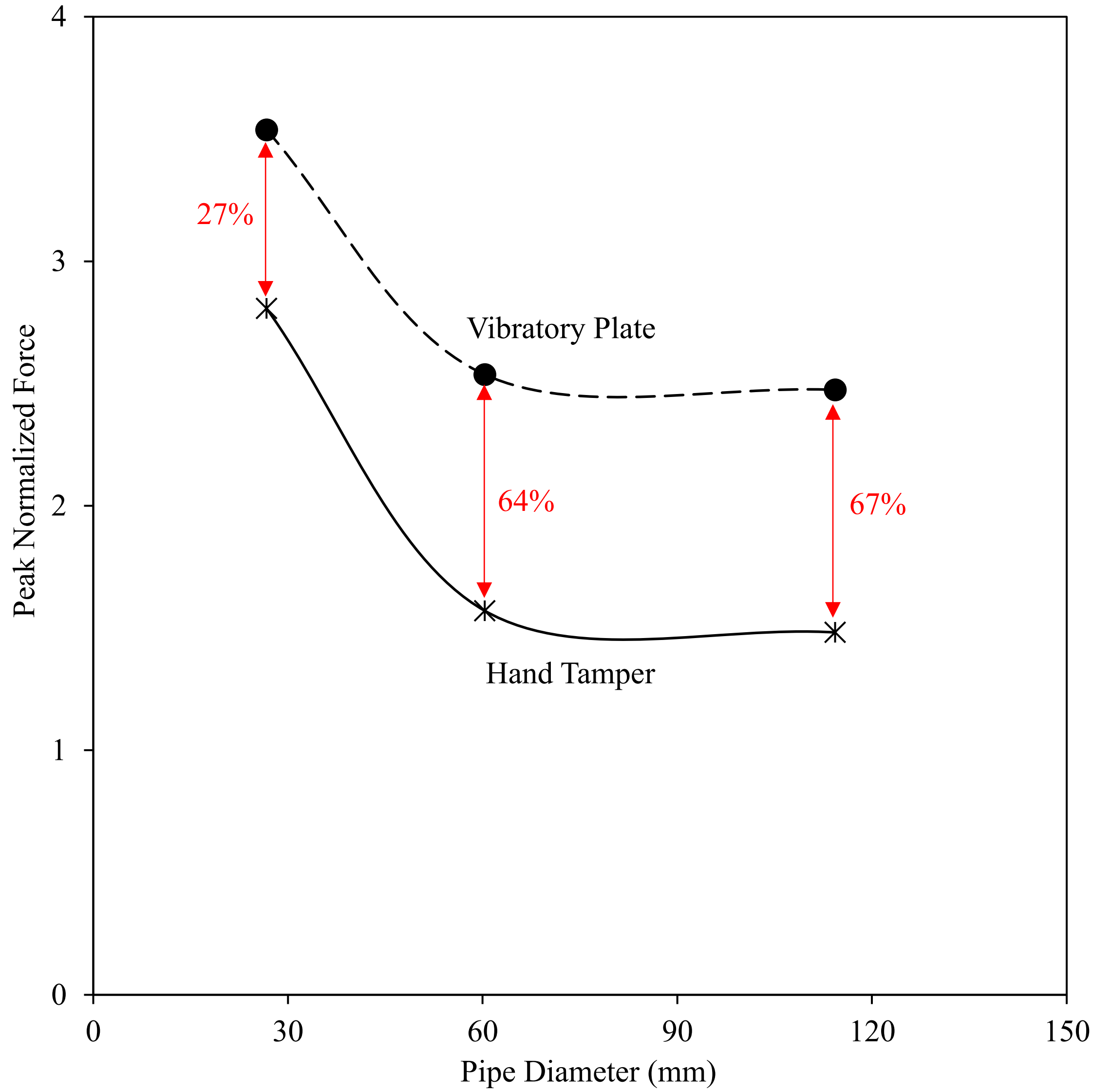

(b)

Figure 3.8: (a) Effect for different backfill compactions; (b) Peak normalized force vs. pipe diameter

As mentioned earlier, field measurements of compaction-induced earth pressure indicate that the residual horizontal earth pressure of compacted backfill remains larger than the horizontal earth pressure at rest and does not significantly change with time (Sowers et al.

1957, Duncan et al. 1991). Thus, when the backfill soil undergoes compaction, additional soil stresses as "locked-in" compaction-induced stresses can increase the normal stresses on the pipe circumference. The increase in normal stress can then essentially increase the shearing resistance of the pipe-soil interface, resulting in higher axial pipe resistance. Duncan et al. (1991) developed earth pressure charts and tables to estimate residual horizontal pressure due to compaction by rollers, vibratory, and rammer plates.

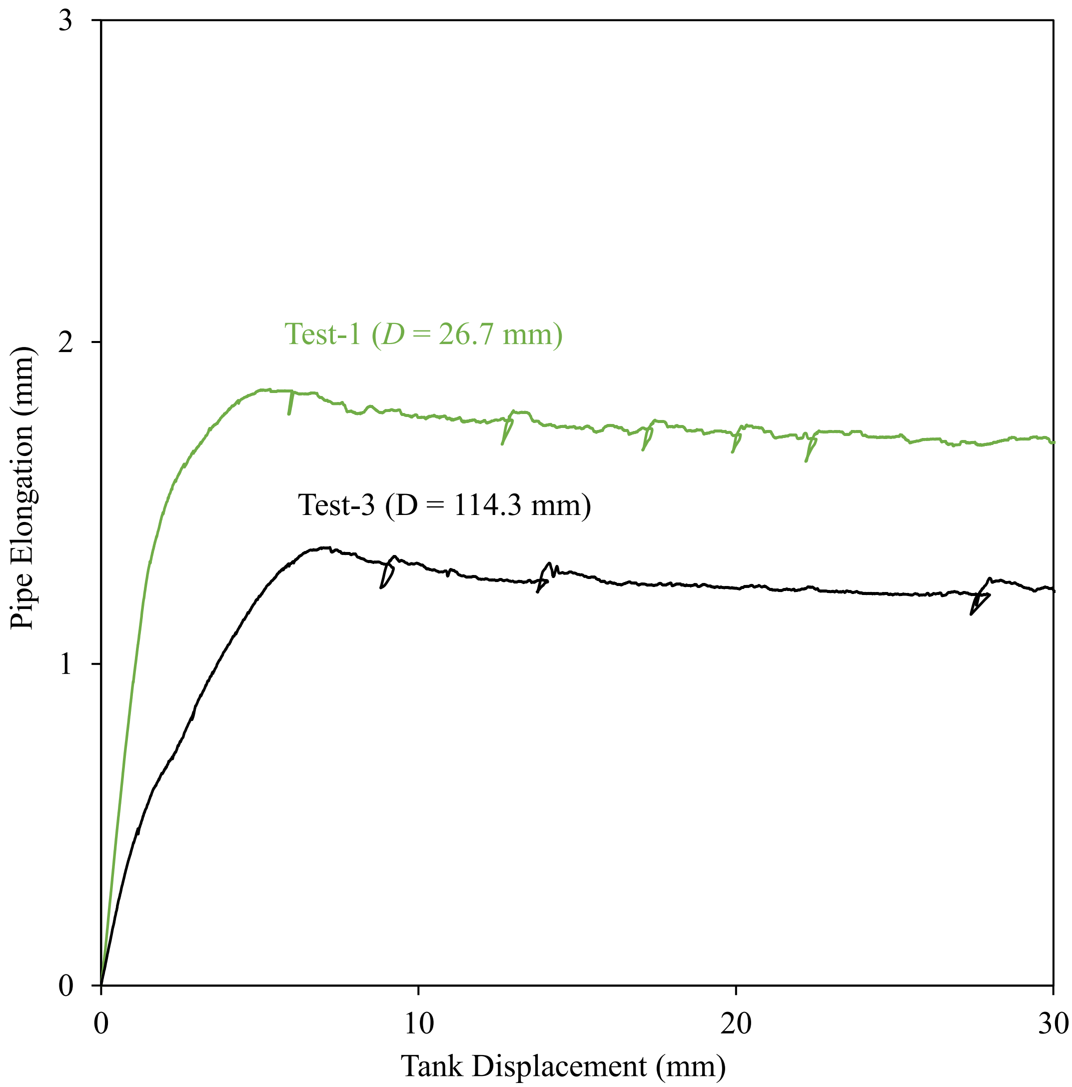

Figure 3.9: Pipe elongation with tank displacement

Figure 3.9 shows the pipe elongations obtained in Tests 1–3, estimated based on the difference between the two LVDT readings. Pipe elongations gradually increase with tank displacement and peak at the displacements corresponding to peak axial forces, showing similar patterns like load–displacement curves. The maximum pipe elongation ranged between 1 and 2 mm, which is not very significant. Hence, the tests described in this study can be considered rigid pipe tests (i.e., element-level tests). However, longer steel pipelines subjected to axial ground deformation may experience higher elongation in the field. As seen in the figure, pipe elongation is less for the pipe with a larger diameter (i.e., the pipe with higher rigidity).

During testing, the axial strain of pipes was also monitored near the restrained end at the pipe crown. Figure 3.10 shows the measured strains for Tests 3 (compacted backfill) and 4 (loose backfill). As seen in the figure, the maximum strain was almost double that of compacted sand compared to loose sand. However, the maximum strain values are significantly lower (~0.005%) and are well below the typical yield strain of 0.2% for steel pipes subjected to longitudinal ground movement (Chan and Wong 2004; Weerasekara and Rahman 2019). The low strain values also support the negligible elongation in the pipe, as discussed above.

Figure 3.11 shows how different soil displacement rates affect the pipe's axial resistance to ground movement when the backfill soil is compacted using a hand tamper. A decrease in the maximum axial force was observed with increasing the tank displacement rate for all the pipes. When pulling rates were increased from 0.5 mm/min to 2 mm/min, the peak axial forces experienced by 26.7 mm and 60.3 mm pipes decreased by approximately 20% (Tests

8-10). Even more significant reductions in resistances were observed for the 114.3 mm pipe, with the peak axial force decreasing by approximately 30% (Test-11) when subjected to a pulling rate of 2 mm/min compared to a pulling rate of 0.5 mm/min. This variation in the peak resistance may be due to non-uniform compaction along the pipe length by the hand tamper.

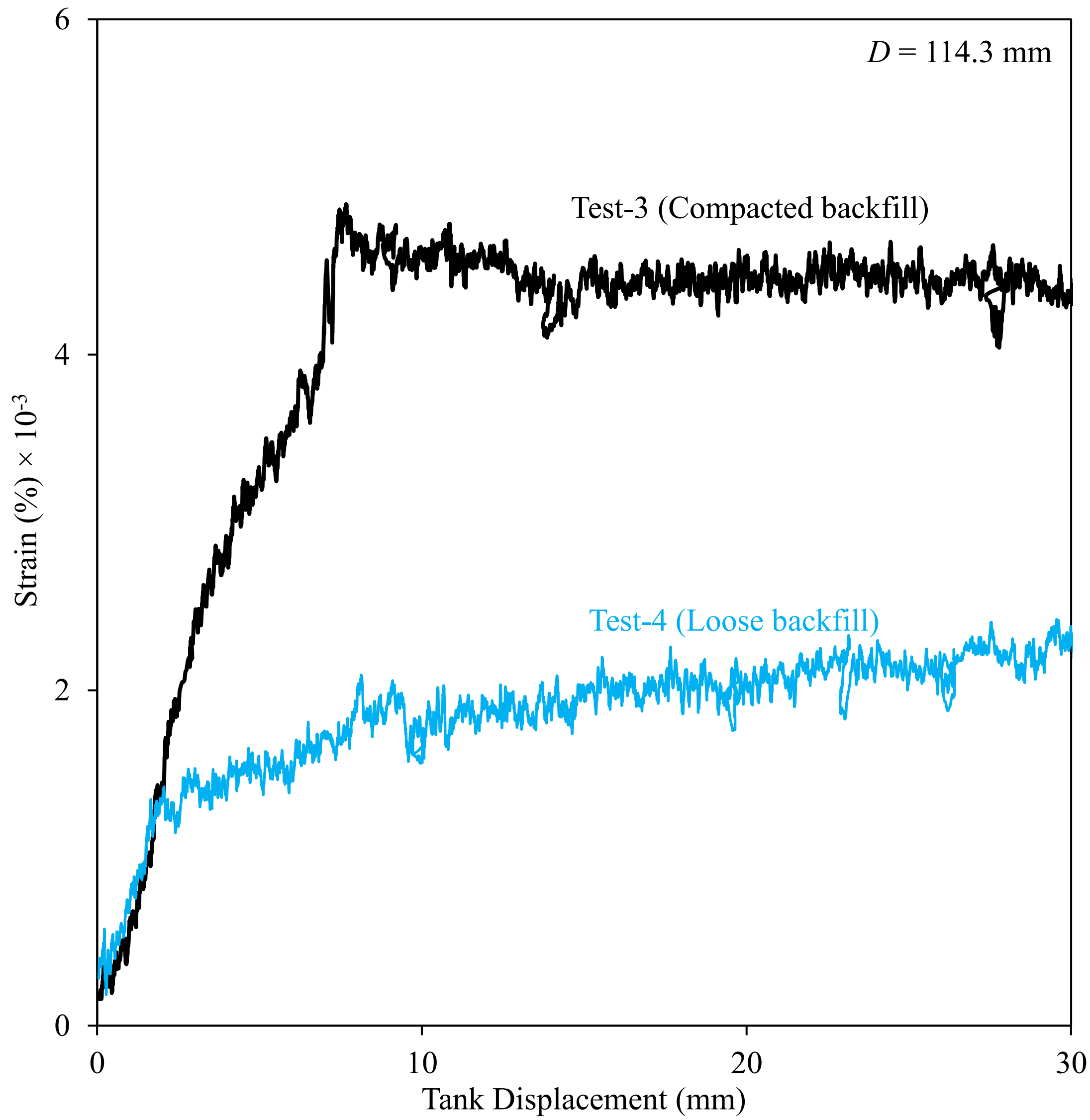

Figure 3.10: Axial strain distribution at the restrained end

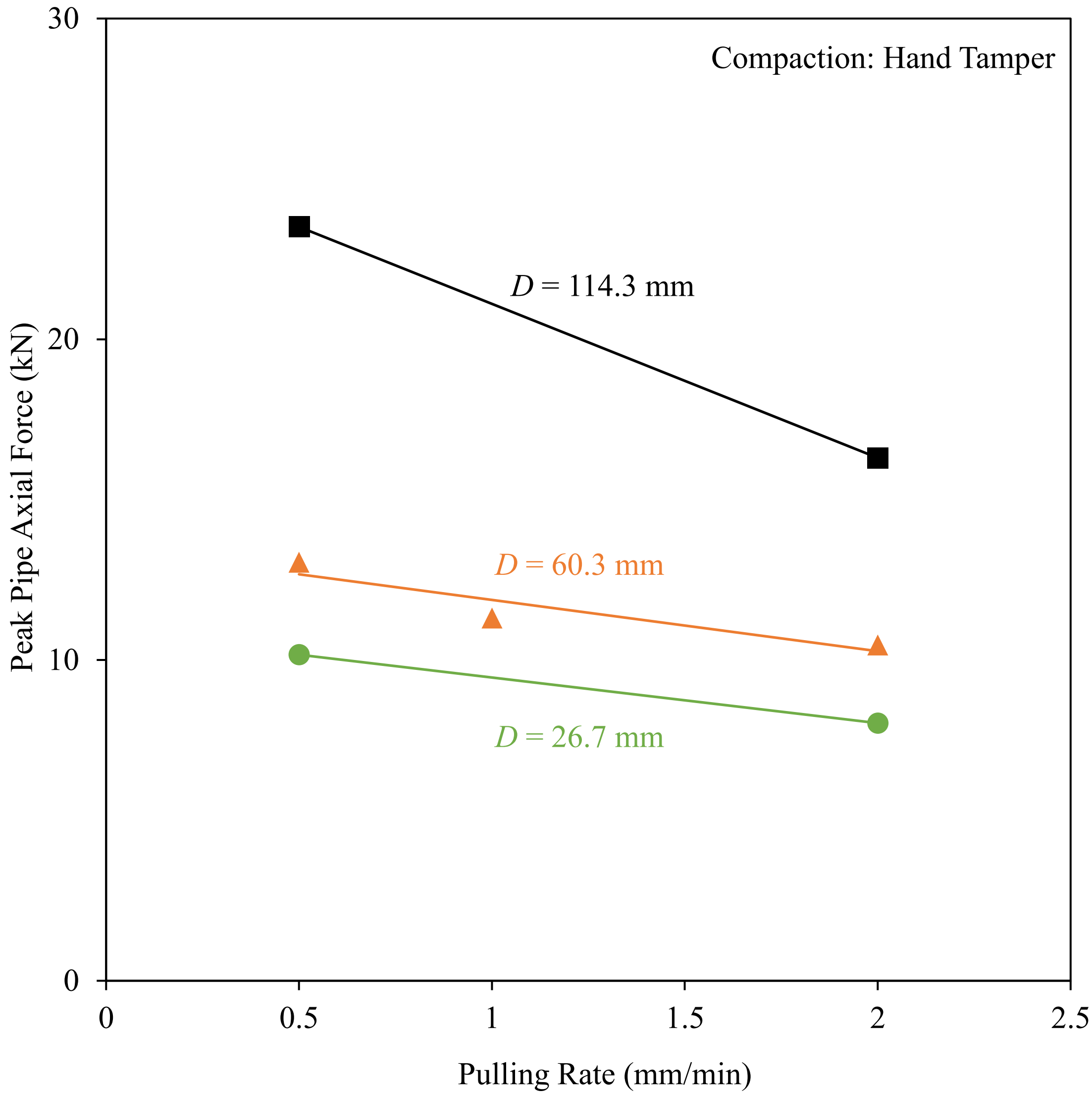

Figure 3.11: Peak pipe axial force with pulling rates

An additional test (Test-12) was performed by compacting the backfill using a vibratory plate compactor at a soil-pulling rate of 2 mm/min. Figure 3.12 shows the variation of normalized forces at different soil displacement rates for 26.7 mm pipes. It is clear that as the soil displacement rates increase, the normalized forces acting on the pipe decrease. This reduction in normalized forces can be attributed to the fact that when the soil moves at a faster rate, it may not have sufficient time to develop its full frictional resistance against the pipe. Note that Wijewickreme et al. (2009) reported no noticeable impact of pipe pullout rates on the axial force for rates from 120 to 3000 mm/min. However, the force–displacement response or the peak magnitude of the load was not reported in that study. More experimental studies with varying pipe diameters are needed to observe the effect of different soil displacement rates on the pipe's axial resistance to ground movement.

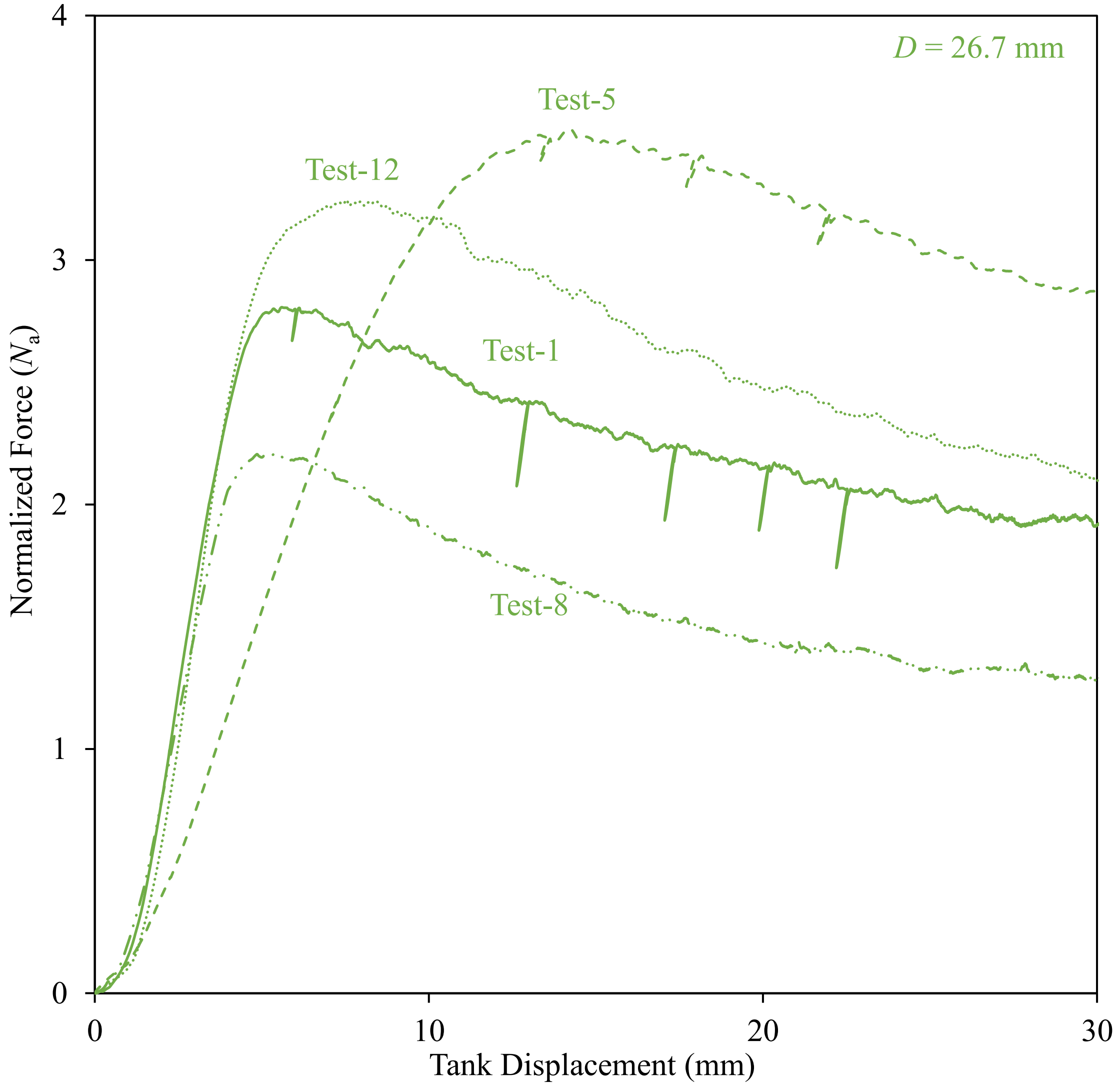

Figure 3.12: Normalized force vs. tank displacement

Figure 3.13 presents the comparison of nondimensional peak axial forces between soil tank pullout and pipe pullout tests in relation to pipe diameters. Note that no pullout tests of small-diameter pipes are available in the literature for direct comparison with the current study. Also, all previous studies were conducted by pulling a pipe through a static soil mass, unlike those in the current study. It is evident in the figure that the peak normalized forces developed during tank displacements are significantly higher than those developed by pipe pullout for pipes in dense sand. The higher forces in the tank pullout tests are likely attributable to factors associated with the current test configurations.

Firstly, the effect of soil dilation is prominent for smaller pipe sizes, as discussed earlier. Besides, different studies adopted different types of soil, compaction techniques and used different compactors. Consequently, the magnitude of the lateral force for these studies would also be different. Furthermore, the compaction effects depend significantly on the pipe burial depths, where the lateral compaction force decreases with burial depths. Most data from pipe pullout tests shown in Figure 3.13 were for higher burial depths than those used in this study. In addition, particles at the interface may exhibit non-uniform particle displacement around the pipe during soil box pulling, while soil particles at the interface may not move at all during pipe pull. Therefore, the contact pressure between the soil and the pipe could differ significantly, specifically for relatively smaller diameter pipes in each scenario. Further study is recommended to explore these mechanisms for a better understanding of the soil-pipe interaction.

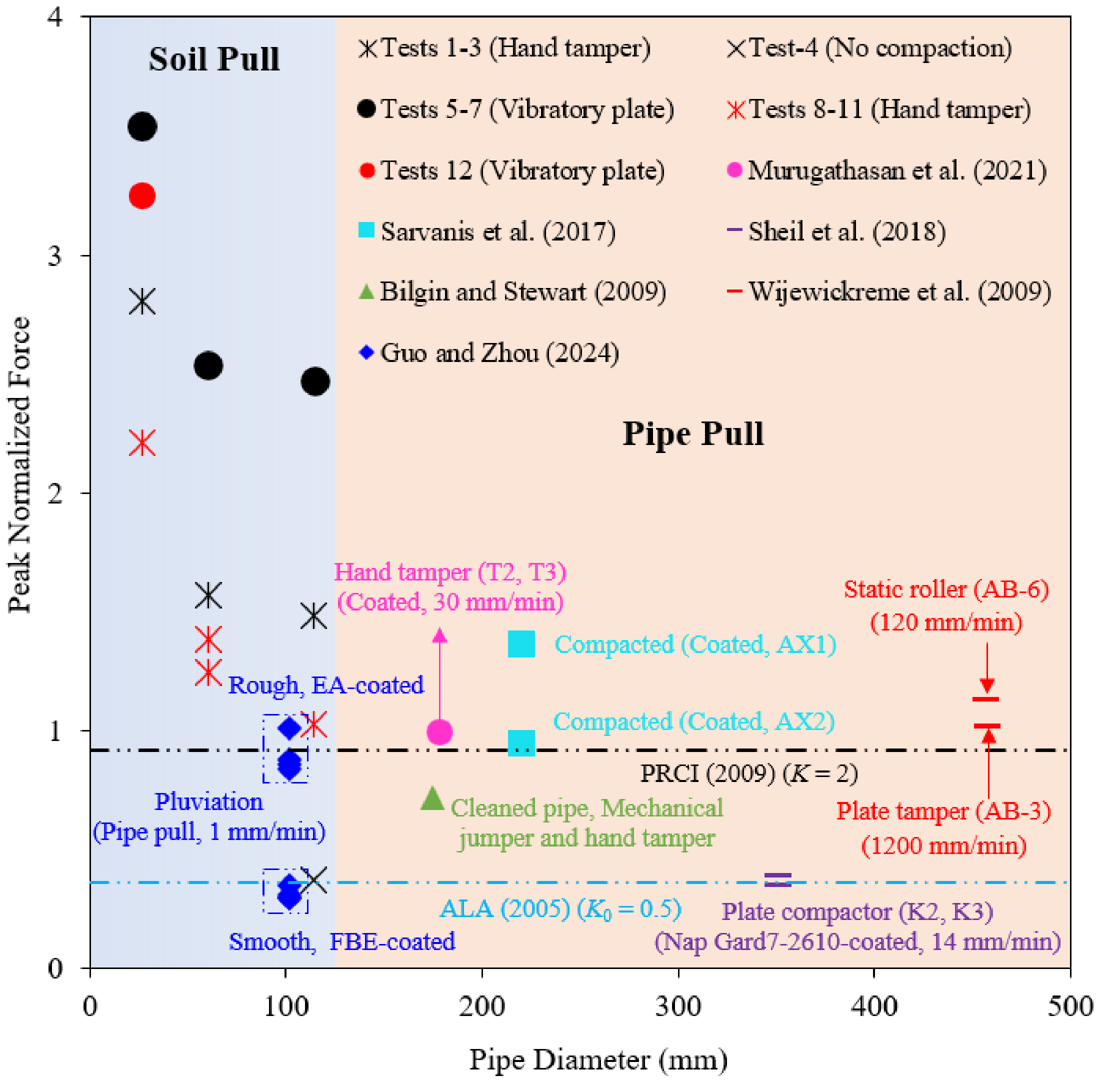

Figure 3.13: Soil pulling and pipe pulling comparison

3.5 Conclusions

This study highlights the laboratory observations of small-diameter buried gas distribution pipes subjected to axial ground movement. A 4-meter-long box was moved parallel to the pipe's longitudinal axis to simulate the moving soil in the laboratory. Steel pipes with three different diameters (26.7 mm, 60.3 mm, and 114.3 mm) were used during the tests. Two different backfill compaction methods were applied to explore the effects of compaction-induced stress on the pipe axial force. The following conclusions are drawn from this study:

- The axial force of the pipe linearly increased with ground movement. The peak forces were reached when the shearing resistance of the interface soil was mobilized over the pipe length.
- Pipe diameter has a significant effect on the axial pipe–soil interaction. The normalized peak forces are higher for pipes with small diameters.
- Axial forces are higher for pipes with backfills compacted using vibratory compactors than for backfills compacted using a hand tamper.
- A maximum of 1.8 mm of pipe elongation was recorded for the 26.7 mm diameter pipe. The axial strain of the pipe was also negligible, confirming that the steel pipes used in the tests behaved like rigid pipes.
- A 20-30% decrease in peak axial force was observed when the soil pulling rate increased from 0.5 mm/min to 2 mm/min. The variations in pipe axial forces due to different pulling rates were most likely due to the non-uniform compaction achieved by the hand tamper.
- The field density of backfill sand can be less than the minimum density obtained using standard laboratory tests, leading to uncertainty in the relative density defined based on the laboratory minimum and maximum density tests.

3.6 Acknowledgment

This research study received funding from the Alliance Grants program of the National Science and Engineering Research Council of Canada. Financial and in-kind support from FortisBC Energy Inc. and SaskEnergy Canada Inc. and in-kind support from WSP Canada Inc. are gratefully acknowledged. The authors would like to express their gratitude for the valuable technical and laboratory assistance provided by the research group and laboratory technicians.

3.7 References

ALA (American Lifelines Alliance). 2005. Guidelines for the design of buried steel pipe, Reston, VA, USA.

Andersen, D. 2024. Behavior of small-diameter buried steel pipes subjected to axial ground movement, *M.Eng. thesis*, Memorial University of Newfoundland, Canada.

Andersen, D., and Dhar, A.S. 2023. Investigation of small-diameter steel pipes subjected to axial ground movement, In proc., GeoSaskatoon 2023, *76th CGS Annual Conference*, Canada: Canadian Geotechnical Society.

ASTM D698-12. 2021. Standard test method for laboratory compaction characteristics of soil using standard effort (12,400 ft-lbf/ft^3 (600 kN-m/m3)), ASTM International.

ASTM D1556. 2015. Standard test method for density and unit weight of soil in place by sand-cone method, ASTM International.

ASTM D2321-20. 2020. Standard recommended practice for underground installation of flexible thermoplastic sewer pipe, ASTM International.

ASTM D4253-00. 2006. Standard test methods for maximum index density and unit weight of soils using a vibratory table, ASTM International.

Bain, C.A., O'Rourke, T.D., and Bray, J.D. 2024. Pipeline response to seismic displacement at Balboa Boulevard during the 1994 Northridge earthquake, *Journal of Geotechnical and Geoenvironmental Engineering*, 150 (2): 04023139.

Bilgin, Ö. and Stewart, H. E. 2009. Pullout resistance characteristics of cast iron pipe, *Journal of Transportation Engineering*, 135 (10): 730–735.

Boulon, M., and Foray, P. 1986. Physical and numerical simulation of lateral shaft friction along offshore piles in sand, In Proc., *3rd Int. Conf. on Numerical methods in offshore piling*. Institut Francais du Petrol, Nantes, France.

Chan, P.D.S., and Wong, R.C.K. 2004. Performance evaluation of a buried steel pipe in a moving slope: a case study, *Canadian Geotechnical Journal*. 41 (5): 894-907.

Dezfooli, M.S., Abolmaali, A., and Razavi, M. 2015. Coupled nonlinear finite-element analysis of soil–steel pipe structure interaction, *International Journal of Geomechanics*, 15 (1).

Duncan, J.M., Williams, G.W., Sehn, A.L., and Seed, R.B. 1991, Estimation earth pressures due to compaction, *Journal of Geotechnical Engineering*, 117 (12): 1833-1847.

Eguchi, R.T., and Seligson, H.A. 1994. Lifeline perspective, *Practical Lessons from the Loma Prieta Earthquake*, Edited by National Academies Press, Washington, DC, 135-163.

Eidinger, J. M., Maison, B. F., and McDonough, P. W. 2023. Natural gas system performance in Magna M5.7 2020 earthquake, *Earthquake Spectra*, 39 (1): 103-118.

Ferreira N.J., and Blatz, J.A. 2021. Measured pipe stresses on gas pipeline in landslide areas, *Canadian Geotechnical Journal*, 58 (12): 1855-1869.

Moore, I.D., and Taleb, B. 1999. Metal culvert response to live loading: performance of three-dimensional analysis, *Transportation Research Record*, 1656 (1): 37-44.

Jayawickrama, P., Amarasiri, A.L., and Regino, P.E. 2001. Evaluation of backfill materials and installation for high density polyethlene pipe, Project number: 0-1809, Report number: 1809-3, Texas Tech University.

Johnston, I.W., Lam, T.S.K., and Williams, A.F. 1987. Constant normal stiffness direct shear testing for socketed pile design in weak rock, *Géotechnique*, 37 (1): 83–89.

Karimian, S. A. 2006. Response of buried steel pipelines subjected to longitudinal and transverse ground movement, *Ph.D. thesis*, University of British Columbia, Canada.

Kitaura, M. and Miyajima, M. 1996. Damage to water supply pipelines, *Soils and Foundations*, 36 (Special): 325-334.

Masada, T., and Sargand, S. 2007. Peaking deflections of flexible pipe during initial backfilling, *Journal of Transportation Engineering*, 133: 105-111.

Meidani, M., Meguid, M.A., and Chouinard, L.E. 2018. Estimating earth loads on buried pipes under axial loading condition: insights from 3D discrete element analysis, *Geo-Engineering*, 9:5.

Murugathasan, P., Dhar, A.S., and Hawlader, B. (2021). An experimental and numerical investigation of pullout behavior of buried ductile iron water pipes in sand. *Canadian Journal of Civil Engineering*, 48 (2): 134–143.

NSCPA (National Corrugated Steel Pipe Association) 2018. Corrugated steel pipe design manual, *National Corrugated Steel Pipe Association*, Dallas, TX 75244.

O'Rourke, T.D., Gowdy, T.E., Stewart, H.E., and Pease, J.W. 1991. Lifeline and geotechnical aspects of the 1989 Loma Prieta earthquake, In Proc., *2nd International Conference on Recent Advances in Geotechnical Earthquake Engineering and Soil Dynamics*, St. Louis, Mo., 1601–1612.

Park, S.S. 2010. Evaluation of the sand-cone method for determination of the in-situ density of soil, *Géotechnique*, 60 (9): 701–707.

PHMSA (Pipeline and Hazardous Materials Administration). 2015. Fact sheet: pipeline materials, Retrieved February 10, 2024, from https://primis.phmsa.dot.gov/comm/FactSheets/FSPipelineMaterials.htm

Porter, M., Hove, J.V., and Barlow, P. 2022. Analysis of dynamic system risks where pipelines cross slow-moving landslides, In Proc., *ASME 2022 14th International Pipeline Conference*, Calgary, Alberta, Canada.

PPI (Plastics Pipe Institute) 2008. Underground installation of PE piping, *Handbook of Polyethylene Pipe*, Edited by Plastics Pipe Institute, 265-303.

Prabhu, S., and Qui, T. 2021. Effects of lift thickness, backfill material, and compaction energy on utility trench backfill compaction using hydraulic plate compactors, *Journal of Pipeline Systems Engineering and Practice*, 12 (1).

PRCI (Pipeline Research Council International) 2009. Guidelines for constructing natural gas and liquid hydrocarbon pipelines through areas prone to landslide and subsidence hazards, Report prepared for the Design, Material, and Construction committee, Pipeline Research Council International, Inc.

Reza, A., and Dhar, A.S. 2021. Axial pullout behavior of buried medium-density polyethylene gas distribution pipes, *International Journal of Geomechanics*, 21(7).

Reza, A., Dhar, A.S., and Rahman, M. 2023. Strain assessment of polyethylene pipes in dense sand subjected to axial displacement, *Geosynthetics International*, 31 (4):469-486.

Saha, R.C. 2021. Shear strength assessment of a manufactured well-graded sand, *M.Eng. thesis*, Memorial University of Newfoundland, Canada.

Saha, R.C., Dhar, A.S., and Hawlader, B.C. 2019. Shear strength assessment of a well graded clean sand, In Proc., GeoSt. John's 2019, *72nd Canadian Geotechnical Conference*, St. John's, NL, Canada.

Sarvanis, G.C., Karamanos, S.A., Vazouras, P., Mecozzi, E., Lucci, A., and Dakoulas, P. 2017. Permanent earthquake-induced actions in buried pipelines: numerical modeling and experimental verification, *Earthquake Engineering & Structural Dynamics*, 47 (4): 966-987.

Sheil, B.B., Martin, C.M., Byrne, B.W., Plant, M., Williams, K., and Coyne, D. 2018. Full-scale laboratory testing of a buried pipeline in sand subjected to cyclic axial displacements, *Géotechnique*, 68 (8): 684–698.

Sowers, G.F., Robb, A.D., Mullis, C.H., and Glenn, A.J. 1957. The residual lateral pressures produced by compacting soils, In Proce., *4th International Conference on Soil Mechanics and Foundation Engineering*, 2: 243-247.

TSB (Transportation Safety Board of Canada). 2024. Pipeline occurrence statistics for 2022, Retrieved February 10, 2024, from https://www.bst-tsb.gc.ca/eng/stats/pipeline/2022/ssep-sspo-2022.html

USGS (U.S. Geological Survey). 2021. 1994 Northridge, Retrieved February 06, 2024, from https://www.usgs.gov/media/galleries/1994-northridge

Wang, F., Han, J., Khatri, D.K., Parsons, R.L., Brennan, J.J. and Guo, J. 2015. Field installation effect on buried steel-reinforced high density polyethylene pipes, *Journal of Pipeline Systems Engineering and Practice*, ASCE, 7 (1): 0401503.

Weerasekara, L. and Rahman, M. 2019. Framework for assessing the integrity of natural gas distribution pipes in landslide areas, In Proc., GeoSt. John's 2019, *72nd Canadian Geotechnical Conference*, St. John's, NL, Canada.

Wijewickreme, D., Karimian, H., and Honegger, D. 2009. Response of buried steel pipelines subjected to relative axial soil movement, *Canadian Geotechnical Journal*, 46 (7): 735–752.

Chapter 4: Finite Element Modeling of Axial Soil-Pipe Interaction for Small-Diameter Steel Pipes

4.1 Introduction

This chapter briefly discusses the development of three-dimensional (3D) finite element (FE) models to investigate the axial soil-pipe interaction for small-diameter steel pipes. The FE method is particularly effective for addressing complex engineering problems by discretizing the domain of interest into numerous small elements connected by nodes. Each element is defined by partial differential equations that describe its behavior under various conditions. Once formulated, the equations are solved for each element to obtain local responses. By combining these responses, the FE method approximates the overall response of the body to applied loads. The FE method is also recommended by design guidelines (ALA 2005, PRCI 2009) to account for nonlinear soil and pipeline interactions.

The beam-on-spring approach has been widely used to understand the underlying mechanics of soil-pipe interaction problems (Andersen 2024, Reza and Dhar 2024, Sinha and Dhar 2023, Al-Khazaali and Vanapalli 2019, Roy et al. 2016, Jung et al. 2013). This method is ideal for analyzing pipe lengths of several kilometers; however, identifying spring parameters to represent soil-pipe interaction is often challenging. Recent studies have successfully employed a 3D continuum-based FE approach to investigate the load transfer mechanism of buried pipelines (Anzum and Dhar 2024, Reza and Dhar 2021, Barrett and Phillips 2020, Muntakim and Dhar 2020, Almahakeri et al. 2019, Robert et al. 2016). This approach enables regorous modeling of both the pipe and the surrounding soil.

However, challenges can arise when using a 3D FE approach, particularly due to the large scale of the PGD zone and uncertainties involved in selecting material parameters. Nonetheless, a continuum-based 3D FE modeling approach was employed to simulate the test conditions described in Chapter 3. Commercially available FE software, Abaqus (Dassault Systèmes 2019), was used to perform the quasi-static analysis. The analysis type was dynamic with an implicit solution technique using the full Newton method. The selection of the appropriate constitutive model and material parameters are crucial for accurately simulating the results and will be discussed further in the subsequent sections.

4.2 Constitutive Modeling of Soil

The conventional linear elastic–perfectly plastic Mohr–Coulomb model was employed to simulate the stress–strain relationship and shear failure of soil. This model was found to be effective in predicting peak soil resistance during axial pullout tests (Reza and Dhar 2021, Muntakim and Dhar 2020, Murugathasan et al. 2020). In this model, failure is defined when the shear stress on any point reaches a maximum value (τ_f), which depends on the normal stress in the same plane, as illustrated in Figure 4.1. Elastic deformation of soil is considered until the stress state reaches the yield surface, after which plastic deformation develops. The soil is assumed to dilate at a constant dilation angle at that point.

The Mohr–Coulomb criterion is defined as,

$$\tau_f = c' + (\sigma_n')_f \tan\phi' \qquad (4.1)$$

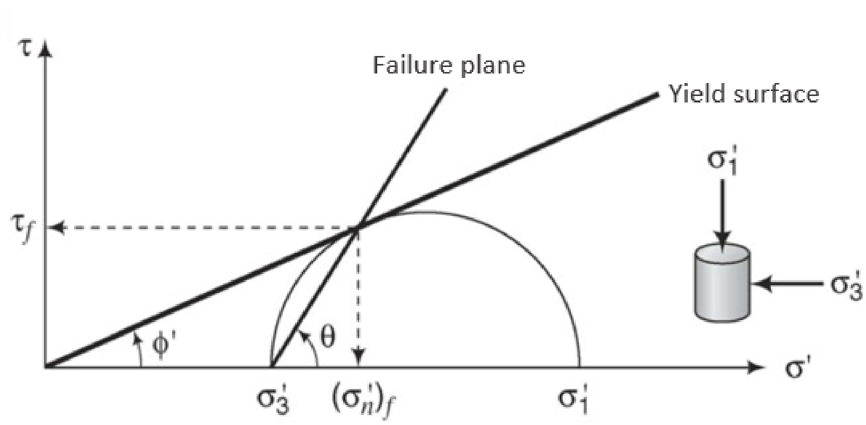

Figure 4.1: Mohr–Coulomb failure criteria

where c' denotes the cohesion, and ϕ' represents the angle of internal friction of soil in terms of effective stress. However, in real field conditions, the soil may experience plastic strain before reaching the yield surface, and a non-constant dilation angle may be observed. For axial soil-pipe interaction problems, plastic strain is generally expected within a thin zone of the soil surrounding the pipe (Murugathasan et al. 2020). Therefore, the built-in Mohr–Coulomb plasticity in the Abaqus/Standard package was employed to simulate the test conditions described in Chapter 3. The input soil parameters include Young's Modulus (E_s), Poisson's ratio (v), cohesion (c'), angle of internal friction (ϕ'), dilation angle (ψ), and soil density (γ), which are often estimated based on the available information in the existing literature domain.

4.3 Soil Parameters

The Young's Modulus (E_s) of soil can be estimated using the stress-dependent power function, as shown in Equation (4.2) (Janbu 1963).

$$E_s = Kp_a \left(\frac{p'}{p_a}\right)^n \qquad (4.2)$$

In Equation (4.2), K is the material constant, p_a is the atmospheric pressure (i.e., 100 kPa), p' is the mean effective confining pressure experienced by the soil, and n is the exponent used for the calculation. The mean effective confining pressure can be computed by Equation (4.3) at the springline level. Young's modulus can be estimated with $K = 150$ and $n = 0.5$ for the triaxial test condition, as expected for the present study (Roy et al. 2016). Thus, at the pipe springline level, Young's modulus was approximated as 5 MPa (Murugathasan et al. 2020).

$$p' = \frac{\gamma H(1 + 2K_0)}{3} \qquad (4.3)$$

where H is the burial depth of the pipe, and K_0 is the lateral earth pressure coefficient at-rest condition.

The other elastic parameter of an isotropic material is the Poisson's ratio (v). The value of Poisson's ratio usually varies from 0.15 to 0.35 for loose to dense sand and 0.2 to 0.4 for stiff to soft clay (Budhu 2010). In this study, Poisson's ratio was assumed to be constant with a value of 0.3.

Although cohesionless soil ($c' = 0$) was used in this study, a non-zero cohesion (c') value was often necessary for the Mohr–Coulomb plasticity in the Abaqus/Standard package to avoid possible convergence issues. Therefore, a small value of $c' = 0.1$ kPa was selected to ensure numerical stability during analysis, as this will not affect the credibility of the test results.

Saha et al. (2019) conducted a series of direct shear tests to estimate the shear strength parameters for compacted sand used in this study. The maximum friction angle (49°) was reported for the dry sand (i.e., 0% moisture) condition, which was reduced eventually with the increase in moisture content. Several empirical relations are also available to estimate the peak friction angle as a function of test type. The peak plane strain friction angle (ϕ'_{PS}) can be estimated from direct shear tests (ϕ'_{DS}) by assuming co-axiality of stresses and incremental strains using Equation (4.4) (Davis 1968).

$$\tan\phi'_{DS} = \frac{\cos\psi \sin\phi'_{PS}}{1 - \sin\psi \sin\phi'_{PS}} \qquad (4.4)$$

Lings and Dietz (2004) provided a conservative way of estimating the peak friction angle for plane strain (ϕ'_{PS}) condition from direct shear (ϕ'_{DS}) test data using Equation (4.5).

$$\phi'_{PS} = \phi'_{DS} + 5° \qquad (4.5)$$

Kulhawy and Mayne (1990) proposed Equation (4.6) to estimate the peak friction angle for the triaxial (ϕ'_{TX}) test condition estimated based on the plain strain (ϕ'_{PS}) condition. They reported that the peak friction angle for triaxial compression conditions was approximately 10% lower than the peak plane strain compression friction angle. Thus, the peak friction angle for triaxial compression conditions can be estimated as 42° for the hand tamper compaction method. The vibratory plate compactor increased the density of compacted backfill, as discussed earlier. Under triaxial test conditions, the peak friction angle was estimated as 44° for the vibratory plate compaction method.

$$\phi'_{PS} = 1.12\, \phi'_{TX} \qquad (4.6)$$

Chakraborty and Salgado (2010) provided Equations (4.7) to (4.9) to calculate the peak dilation angle under very low confining pressure.

$$\psi_{max} = \phi'_{max} - \phi'_{cv} = 3.8 I_R \tag{4.7}$$

$$I_R = I_D \left(Q - \ln \frac{100\sigma'_{mp}}{p_a} \right) - R \tag{4.8}$$

$$Q = 7.4 + 0.60 \ln\sigma'_c \tag{4.9}$$

where I_R is the relative dilatancy index, I_D $(= \frac{D_R}{100})$ is relative density, σ'_{mp} is the mean effective stress (in kPa), σ'_c is the confining pressure (in kPa), Q and R (where R = 1) are the fitting parameters, and p_A is the reference stress (100 kPa). Using these relationships, the peak dilation angle was approximated as 12°.

4.4 Interface Parameter

The 'general contact' algorithm was chosen to ensure all potential contact between the interacting soil surface and the pipe surface. Considering the material stiffness, the pipe surface is modeled as a 'master' surface, while the interacting soil surface is modeled as a 'slave' surface. A 'hard contact' pressure-overclosure relationship was chosen to minimize the penetration of the slave surface. In the general contact algorithm, sliding occurs when the shear stress at the interface reaches the maximum value. Note that the interface shear stress is only limited within a thin shear zone surrounding the pipe. A 'penalty' algorithm was used to model tangential contact behavior with a friction coefficient. The design guidelines specify the 'friction factor' for smooth to rough steel pipe to estimate the friction coefficient, as shown in Table 2.1. A friction factor of 0.80 was used for numerical modeling, considering the surface roughness of the steel pipe. Table 4.1 summarizes the soil parameters used in the FE analysis.

Table 4.1: Soil parameters used in FE analysis

Property	**Value**
Modulus of Elasticity, E_s (MPa)	5
Poisson's ratio, v	0.3
Mass density, γ (kg/m^3)	1780
Cohesion, c' (kPa)	0.1
Peak friction angle, ϕ (°)	42
Dilation angle, ψ (°)	12
Interface friction factor, f	0.8

4.5 Model Geometry and Meshing

In the FE analysis, the soil and the pipe were modeled as 3D deformable bodies. The dimensions of the models matched those of the physical models. A soil box measuring 4 × 2 × 1.225 m and a steel pipe segment measuring 4.5 m in length with a diameter of 114.3 mm were used for the numerical modeling. To save computational time, the steel tank was not included in the FE analysis. It is important to note that the strain in the steel tank wall was found to be negligible (Murugathasan et al. 2020), and thereby the tank can be considered rigid.

To model both the soil and the pipe, eight-node linear hexahedral elements with reduced integration and hourglass control (C3D8R) were used. In the reduced integration technique, there is only one integration point at the center of the element, which simplifies calculations and reduces computational time. Hourglass control is necessary for preventing insufficient stiffness in certain directions, enhancing stability, and improving stress representation in reduced integration elements.

A finer ‘structured’ mesh was applied in the immediate vicinity of the pipe, within a radial distance of 3.25 times the pipe diameter (3.25D), since this is the zone of interest. Beyond this zone, a coarser mesh was employed to save computational time, as shown in Figure 4.2. The steel pipe was divided into 48 elements along the perimeter and 2 elements along the thickness. Notably, no significant change in the load–displacement response was observed when the pipe thickness was divided into 4 layers. Along the length, the maximum pipe element size was 80 mm.

Initially, a zero-displacement boundary condition was applied to the bottom and four sides of the soil box, while a fully constrained boundary condition was applied at one end of the pipe. In the pulling step, a 30 mm displacement in the axial direction was applied to the bottom and four sides of the soil box.

Three different modeling techniques, namely, the K model, Expansion model, and Compaction model, were used to simulate the compaction-induced lateral earth pressure encountered in Test-3. The following sections will briefly discuss each of the models developed for the numerical simulation of Test-3.

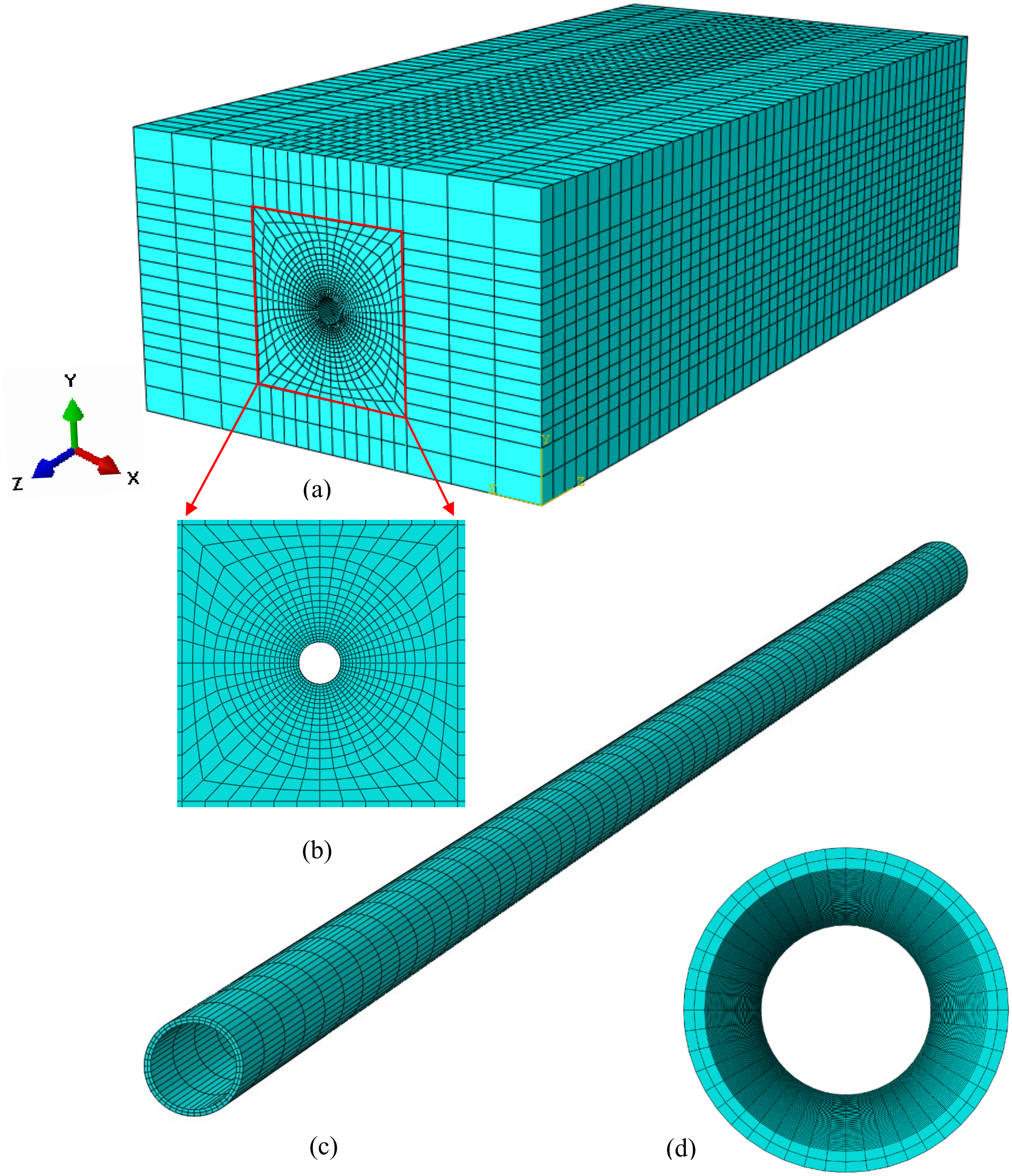

Figure 4.2: (a) 4 × 2 × 1.225 m soil domain; (b) Finer mesh near pipe cross-section; (c) 4.5 m long pipe domain; (d) Pipe cross-section

4.6 Use of Higher Lateral Earth Pressure Coefficient (K Model)

As discussed earlier, the shear-induced dilation associated with the relative movement of dense sand and the pipe leads to an increase in normal stress on the pipe. This stress remains higher than the arithmetic mean of the vertical overburden stress and the horizontal stress at rest condition. Additionally, compaction energy and lift thickness can also affect the stress levels on the pipe. In particular, denser soil at the soil-pipe interface level plays a significant role in developing passive earth pressure conditions. PRCI (2009) suggests using the earth pressure coefficient of value 2. Meidani et al. (2018) proposed Equation (4.1) to use a modified earth pressure coefficient (K) rather than the coefficient of earth pressure at rest (K_0) to account for the normal stress increase.

$$K = 2.75 \times K_0 \times \left(\frac{E}{\gamma H}\right)^{0.38} \times \left(\frac{\varphi}{45}\right)^{1.39} \times \left(\frac{\Delta t}{D}\right)^{0.42} \quad (4.1)$$

In Equation (4.1), E is the soil Young's modulus, γ is the soil unit weight, H is the pipe burial depth, φ is the soil friction angle, Δt is the thickness of the shear zone, and D is the pipe diameter. The thickness of the active shear zone depends on the median grain size (d_{50}) of the soil and can be estimated as $\Delta t = 10d_{50}$. Notably, the effect of compaction energy was not considered in this equation. Based on the test conditions described in Chapter 3, the modified earth pressure coefficient can be calculated as 4.06 for the 114.3 mm diameter pipes.

A predefined field was created initially in the load module to apply this modified earth pressure coefficient. The distribution of the modified earth pressure coefficient along the pipe springline level is shown in Figure 4.3.

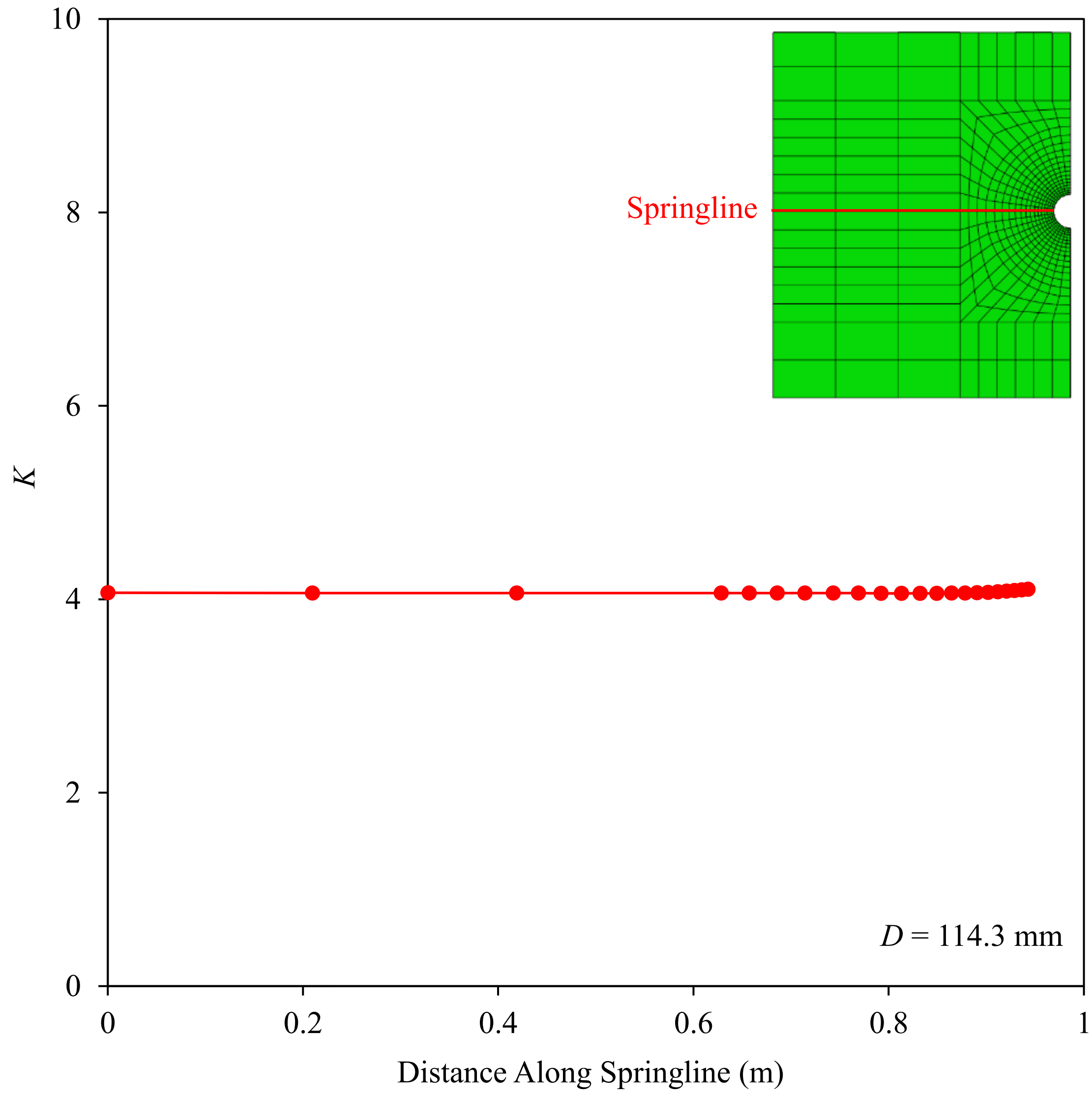

Figure 4.3: Distribution of *K* along the springline level

The vertical soil displacement in the gravity step was also checked and found to be very small (maximum displacement 0.015 mm), indicating that the system reached an equilibrium under the applied gravitational force. Figure 4.4 shows the vertical displacement of the soil domain after the end of the gravity step.

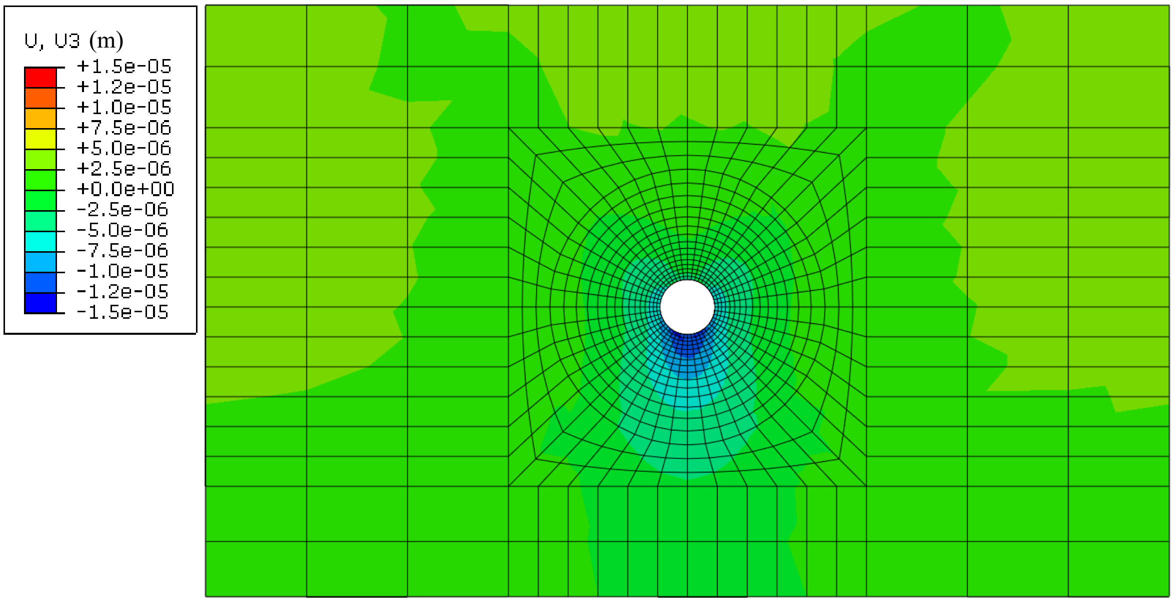

Figure 4.4: Soil displacement in the gravity step

For numerical stability, the kinetic energy of a quasi-static model should remain within 5-10% of the total internal energy. This ensures that the model behaves as expected within a quasi-static regime, as recommended by the Abaqus documentation (Dassault Systèmes 2019). In this study, the kinetic energy of the finite element (FE) model was monitored and found to be significantly less than 10% of the internal energy. This indicates that inertial effects were minimal compared to the internal energy of the system, as shown in Figure 4.5.

Figure 4.6 compares the axial soil resistance obtained from the 3D FE analysis with the laboratory test results. As expected, the Mohr–Coulomb model was unable to capture the post-peak softening behavior observed in the test. However, it reasonably predicted the peak axial resistance, which is the primary focus in axial soil–pipe interaction problems.

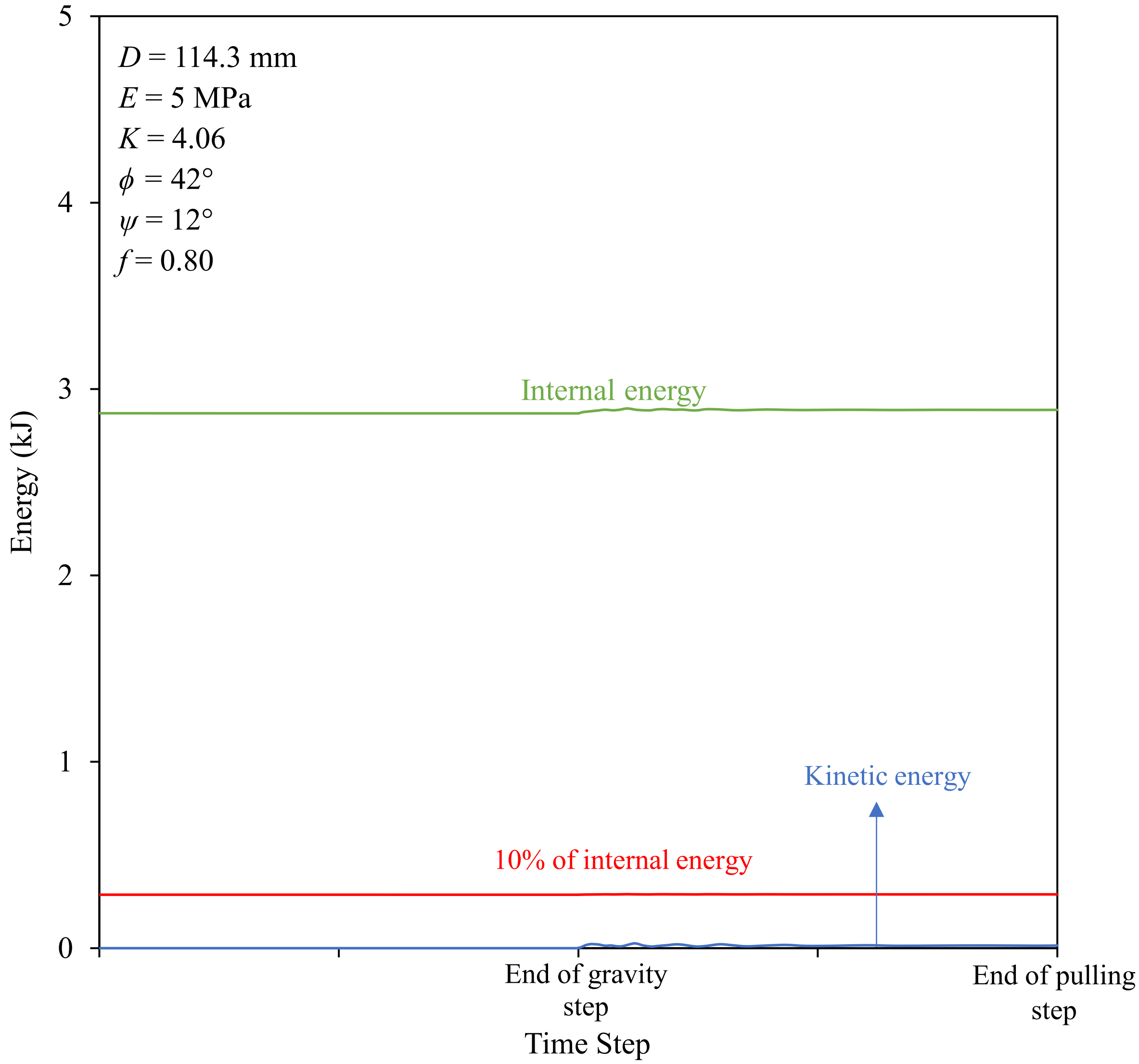

Figure 4.5: Energy check for K model

It is also worth noting that the initial slope of the numerical model differed from that of the experiment. This discrepancy is likely due to the use of a constant Young's modulus in the analysis. In real field conditions, soil may exhibit complex elasto-plastic behavior during loading, influenced by factors such as density, stress history, stress level, and load path, none of which are fully captured by the simplified elastic model.

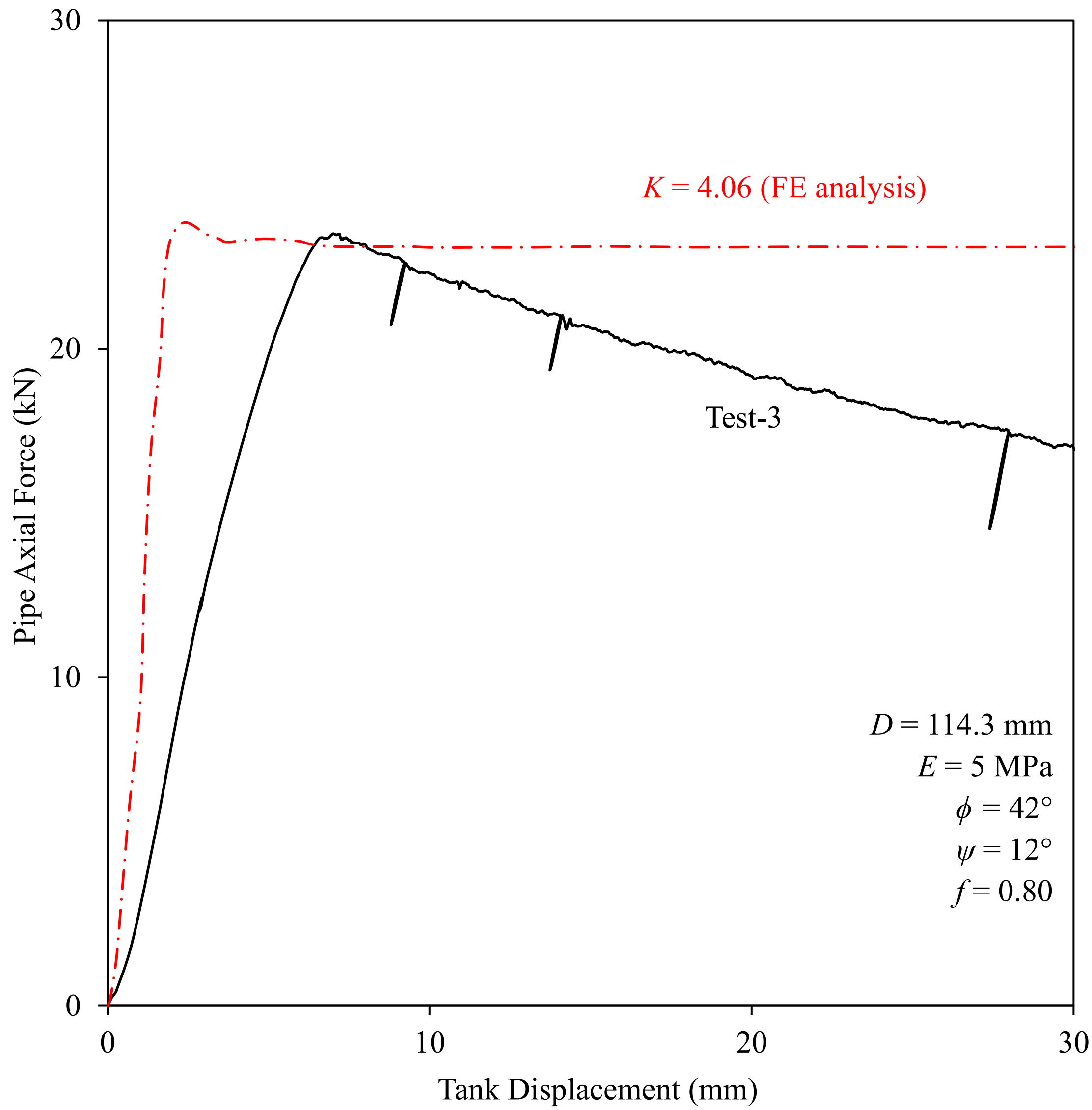

Figure 4.6: Comparison of FE analysis and full-scale laboratory Test-3 (K model)

As mentioned earlier, plastic deformation of the soil is concentrated near the pipe surface, with dilation occurring in this narrow zone (Murugathasan et al. 2020). The distribution of plastic shear strain around the pipe circumference at mid-section is shown in Figure 4.7. The maximum plastic strain was concentrated at the springline level, which can be attributed to the higher value of the modified earth pressure coefficient.

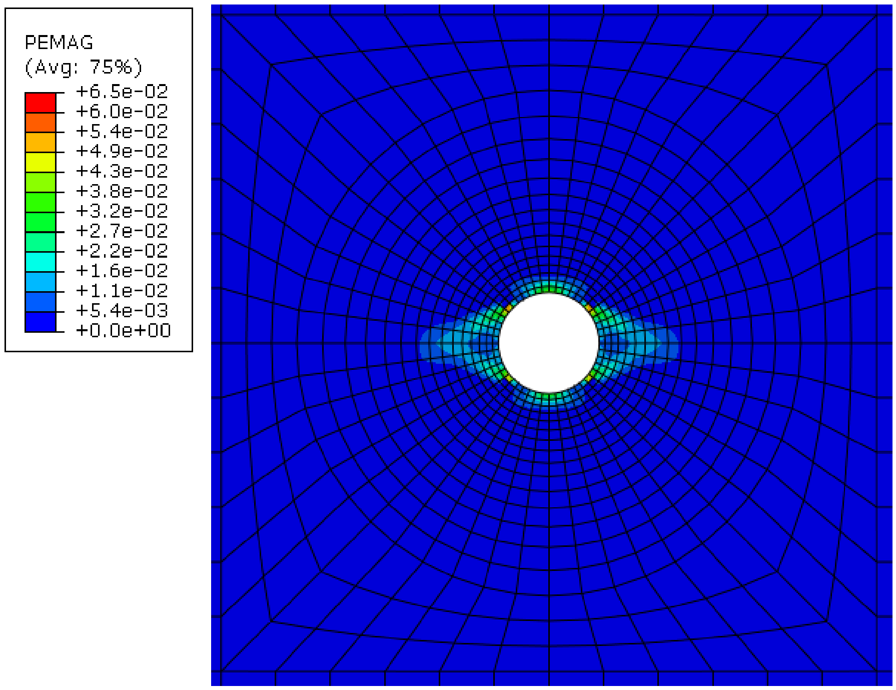

Figure 4.7: Development of plastic deformation zone around the pipe

Figure 4.8 shows the distribution of normal stress around the pipe circumference at the peak axial load. The distribution was almost uniform along the length of the pipe. However, relatively higher normal stress was observed at a distance of 0.90L (towards the trailing end of the pipe), which might be due to the effect of the boundary wall. Compared to the crown and invert, a higher normal stress distribution was observed at the pipe springline level for each of the pipe sections. Wijewickreme et al. (2009) placed pressure transducers at various locations on the pipe, and a higher dimensionless normal stress was also observed at the pipe springline level.

The variations in normal stress with tank displacement are shown in Figure 4.9. As expected, the normal stress at the springline level increased significantly during the pulling step due to locked-in compaction-induced stress, applying a constraint to shear-induced dilation. At the pipe crown and invert, the normal stress decreased, which might be due to the loss of contact between the soil and the pipe. However, the overall average stress remained almost the same during the tank-pulling step, indicating minimum effects of the dilation-induced stress. The increase in pipe axial force for dense sand conditions (Test-3) might be attributed to several factors, most likely the compaction-induced stress or the surface roughness of the pipe.

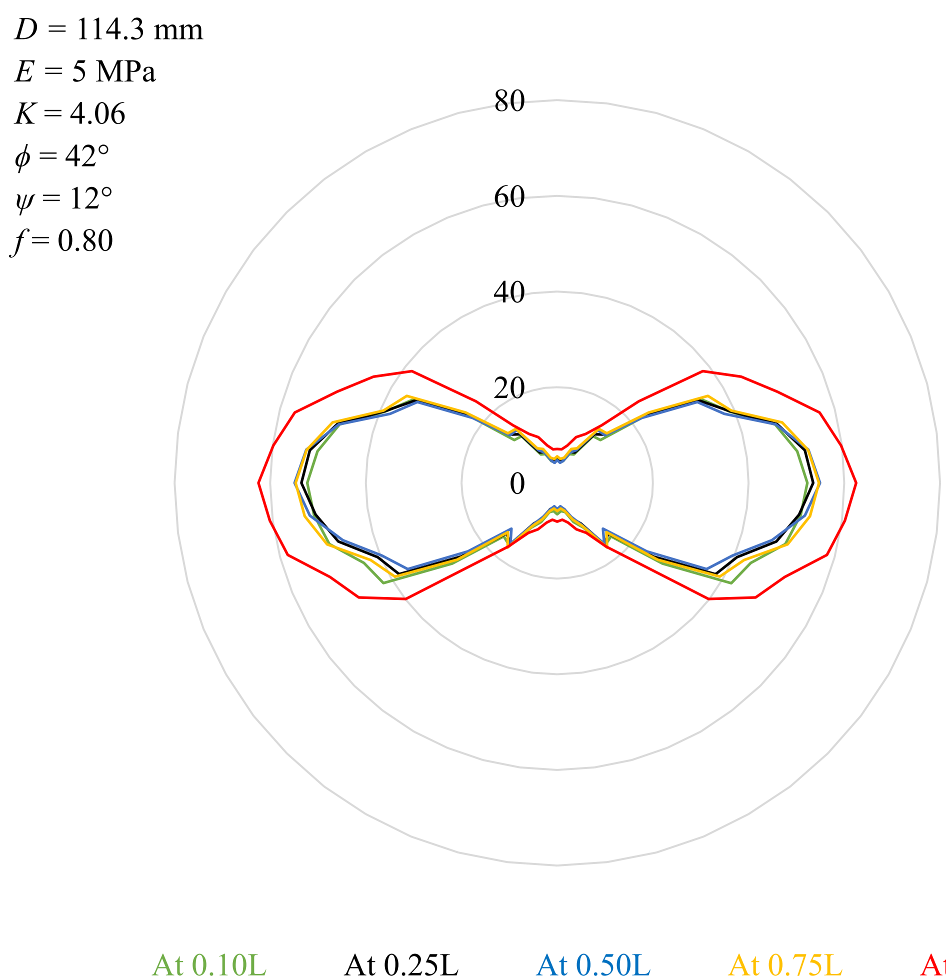

Figure 4.8: Distribution of normal stress (in kPa) around the pipe circumference at peak axial force (K model)

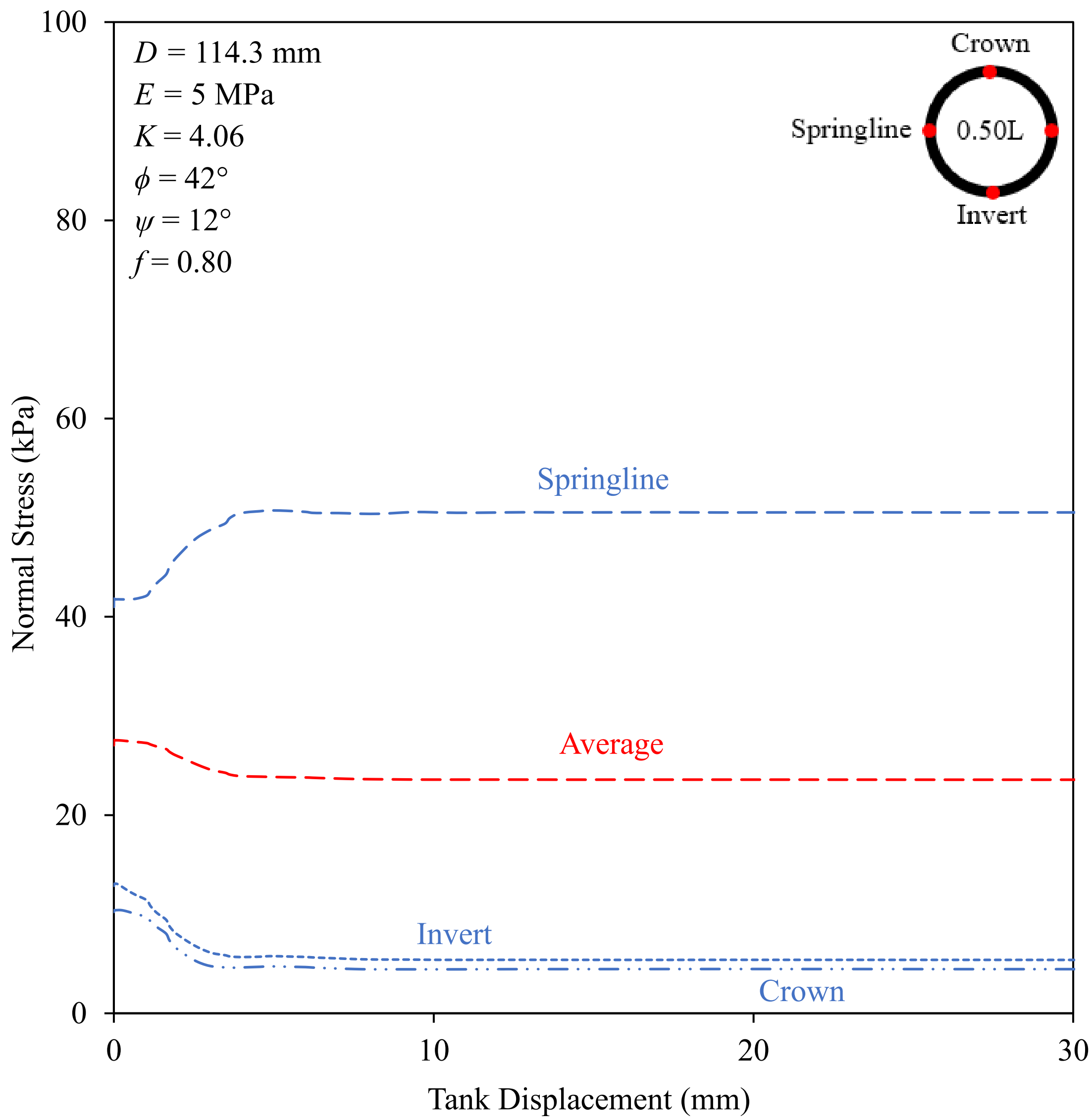

Figure 4.9: Distribution of normal stress with tank displacement (K model)

The average shear stress at a distance of 0.50L (pipe's midspan) of the pipe was also examined through FE analysis (Figure 4.10). It is evident that the distribution of shear stress was consistent with the distribution of normal stress, with higher shear stress observed at the springline level. Notably, the interface shear strength mobilization was not significant at the pipe crown and invert, and beyond the peak, the shear stress was reduced, which might be due to the lower contact pressure on the pipe, as mentioned earlier.

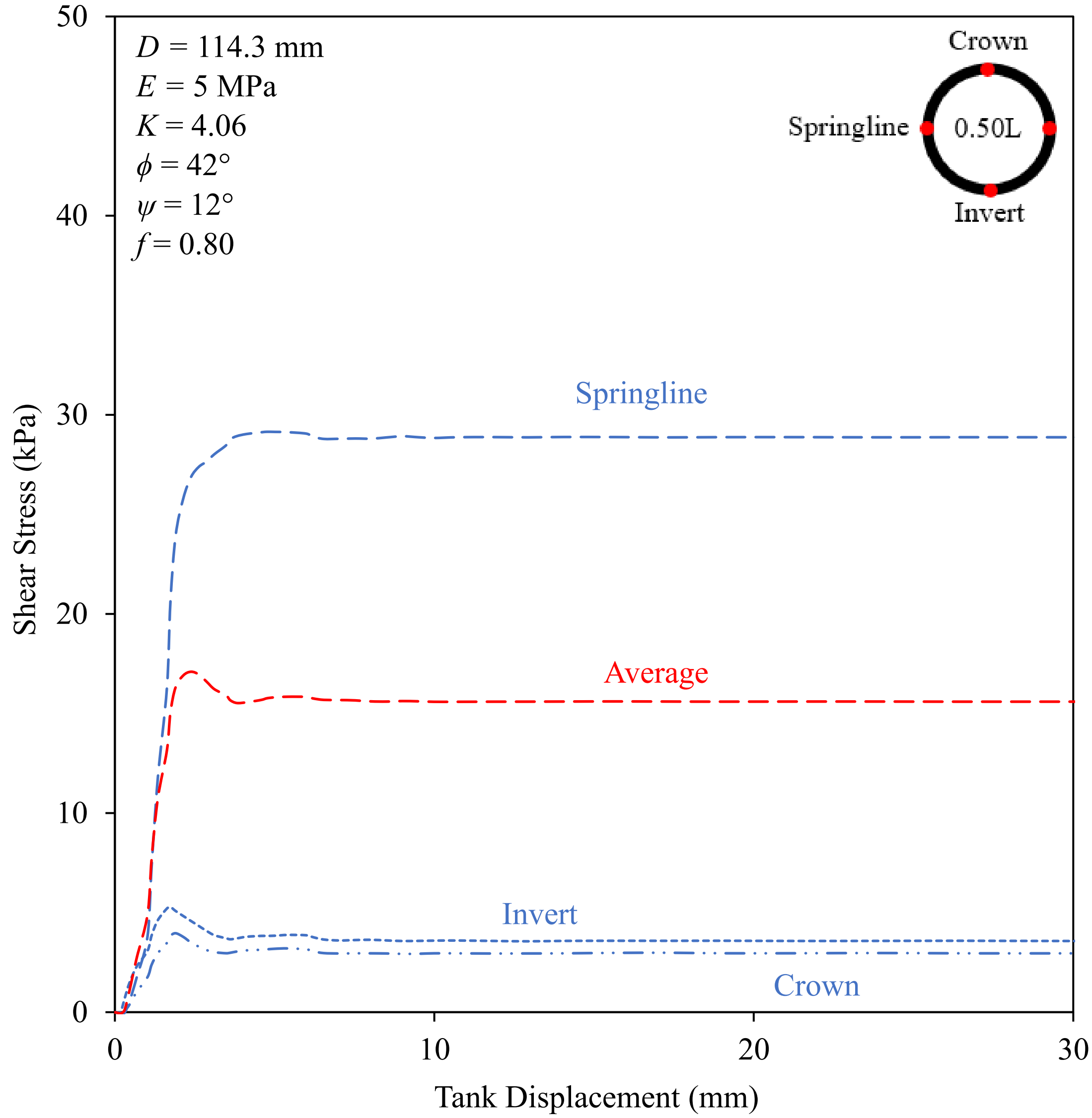

Figure 4.10: Distribution of shear stress with tank displacement at 0.50L (K model)

The average shear stresses at distances of 0.25L and 0.75L were also examined; however, no noticeable change was observed in these sections, with the peak average shear stress varying from 15 kPa to 17 kPa (Figure 4.11).

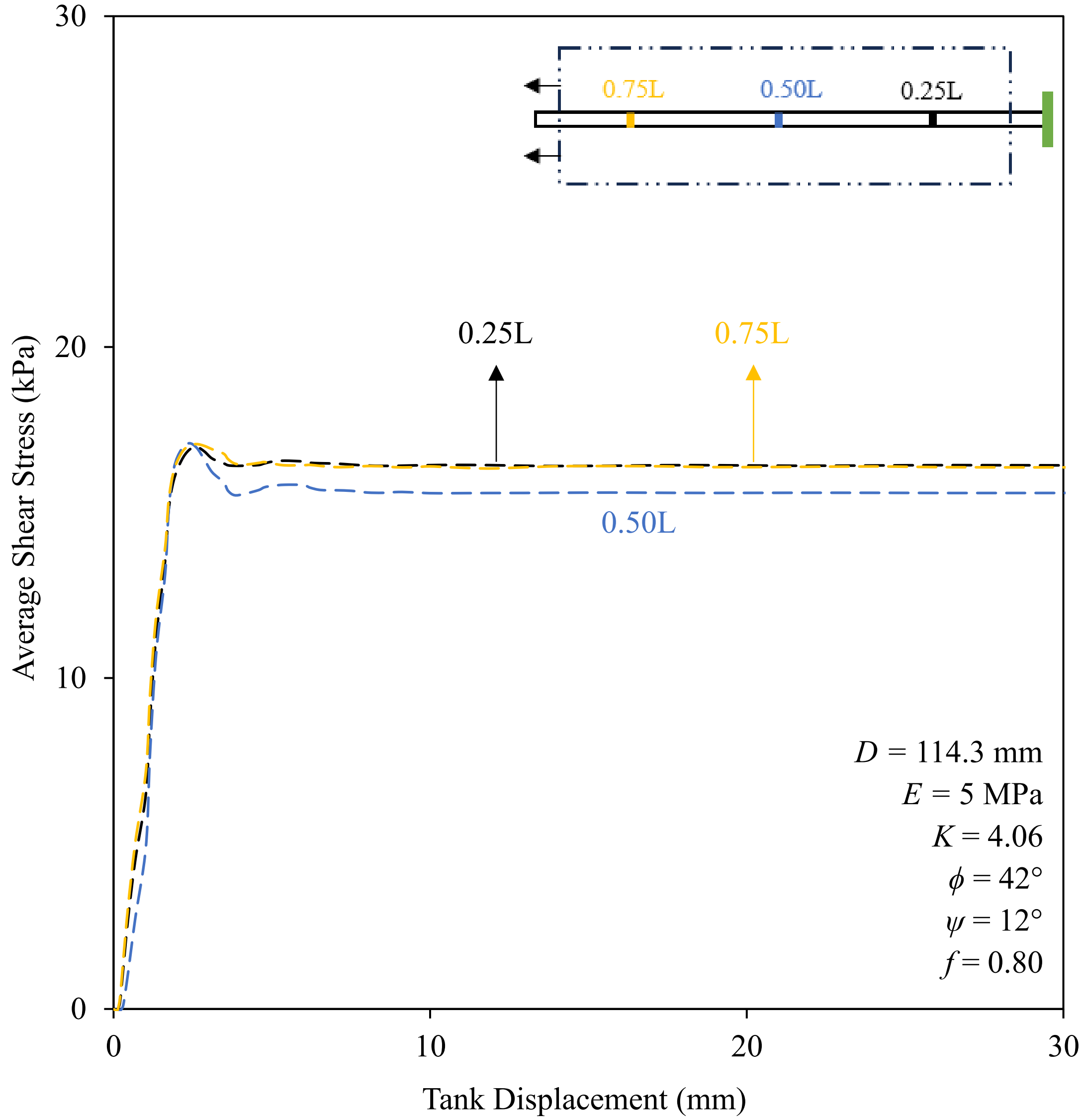

Figure 4.11: Distribution of average shear stress at 0.25L, 0.50L, and 0.75L (K model)

The buried pipeline can experience significant wall stress during the axial ground movement. To examine the wall stress, the maximum von Mises stress at different pipe sections was plotted against the tank displacement at those sections (Figure 4.12). Note that the stress distribution was not uniform throughout the length of the pipe. As expected, the maximum stress occurred at the fixed pipe end and progressively decreased to a minimum at the trailing end section. At approximately 2 mm of tank displacement, the stresses nearly reached their peak value.

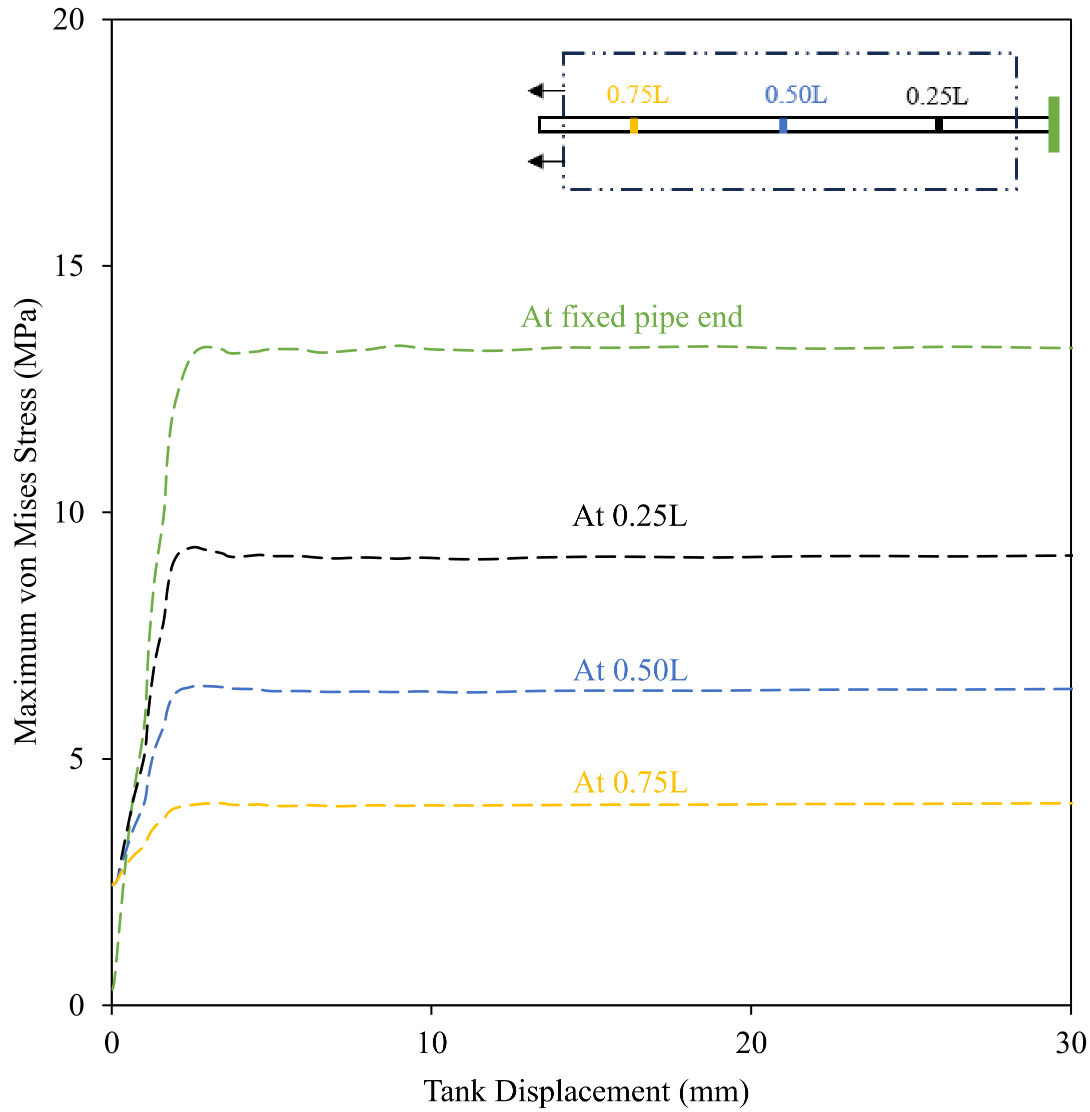

Figure 4.12: Maximum von Mises stress at different pipe sections

4.7 Use of Compaction-Induced Stress (Compaction Model)

As mentioned in Chapter 3, both vertical and horizontal stresses increase during the process of compaction. Once the compaction equipment is removed, the vertical stress decreases to the overburden stress level, while the horizontal stress remains higher than the at-rest value. Katona (1978) developed a squeeze layer compaction technique for both linear and non-linear soil models in 2D FE analysis to simulate compaction-induced horizontal stress on long-span culverts. In this method, a uniform compaction load is first applied to the surface of the first lift. For each subsequent lift, a new uniform load is added, while an equal and opposite pressure is applied to the previous lift to counteract the compaction load. This process continues until the crown is reached, after which no additional compaction load is applied. The squeezing of each lift results in increased lateral pressure due to the Poisson's ratio effect. A similar staged construction procedure was proposed by Mirmoradi and Ehrlich (2015) and Scotland (2016).

McGrath et al. (1999) proposed an alternative method for simulating the compaction of backfill soil layers in FE analysis by applying concentrated nodal forces directly to the pipe. The magnitude of these nodal forces depends on key factors such as the soil friction angle, the backfill compaction method, and the pipe properties. It was assumed that the distribution of the nodal force remained constant over a depth of 300 mm. The authors also reported that the compaction-induced stress for a 900 mm pipe was significantly higher than that for a 1500 mm pipe, in order to match the field deflection under the same compaction method. Later in the study, McGrath et al. (1999) proposed an analytical equation to estimate the equivalent nodal pressure on the pipe for the 2D CANDE model.

Using PLAXIS 2D FE analysis, Wang et al. (2017) simulated the effect of compaction pressure on steel-reinforced high-density polyethylene (SRHDPE) pipes buried in the soil. In their approach, a uniform vertical pressure of 80 kPa was initially applied to the surface of the first lift. Each time a new backfill layer was added, the compaction pressure on the previous layer was deactivated. Once the new soil lift was in place, the 80 kPa compaction pressure was reapplied to the surface of the newly placed lift. This technique effectively simulated the SRHDPE pipe installation process. A similar approach was also proposed by Ezzeldin and Naggar (2020), though they applied a surface load of 15 to 30 kPa to simulate the compaction effects on corrugated metal pipes in their PLAXIS 3D analysis.

Reza et al. (2024) estimated compaction-induced stress with depth using the methods proposed by Duncan and Seed (1986). They calculated the compaction-induced stress by subtracting the at-rest values from the total horizontal pressure. At burial depths of 340 mm and 480 mm, they estimated compaction-induced stresses of 24.7 kPa and 16.2 kPa, respectively. Earlier, Dezfooli et al. (2014) developed an equation to estimate equivalent thermal loading based on compaction-induced stress, considering the interaction between the stiffness of the pipe wall, soil mass, and trench wall. Saleh et al. (2021) proposed a simplified method for estimating equivalent thermal loading at any soil layer by assuming fixed-fixed boundary conditions. Reza et al. (2024) estimated corresponding fictitious temperatures of 100 °C and 65 °C for the stresses of 24.7 kPa and 16.2 kPa, respectively, using the approach proposed by Saleh et al. (2021). In their 3D FE analysis, fictitious temperature loading was applied perpendicular to the pipe axis, simulating the force–displacement responses and pipe wall strains observed in the tests.

In this study, a numerical technique similar to that suggested by Reza et al. (2024) was used to simulate the compaction effects. An orthotropic soil thermal expansion coefficient of 0.00005 /°C was applied perpendicular to the pipe axis. A local coordinate system was assigned to the soil domain to enable the expansion in the orthotropic direction. At a burial depth of 625 mm, the compaction-induced stress was calculated to be 13.8 kPa (Reza et al. 2024). An Expression Field was created to apply the fictitious thermal loading equivalent to the compaction-induced stress, as suggested by Reza et al. (2024).

To ensure the numerical stability of the compaction model, both vertical soil displacement and kinetic energy were monitored. As compared to the K model discussed above, the vertical soil displacement is slightly higher for the compaction model. At the end of the gravity loading phase, the compaction model recorded a maximum vertical settlement of 1.95 mm. Additionally, the kinetic energy of the model also remained within the specified limit of 5-10% of the internal energy, confirming that the system reached a stable equilibrium, and no significant dynamic effects or numerical instability occurred during the gravity loading phase.

The comparison of pipe axial forces between the FE analysis (i.e., compaction model) and Test-3 is shown in Figure 4.13. It is evident that the FE analysis underpredicted the peak axial force by 55% when no compaction load was applied. Notably, using the compaction-induced stress proposed by Reza et al. (2024) also underpredicted the peak axial force by 40%. It is important to note that Reza et al. (2024) applied the compaction-induced stress model to an MDPE pipe. The MDPE pipe experiences diameter reduction under load, which leads to a substantial decrease in the normal stress at the pipe springline level. On the other hand, the higher stiffness of the steel pipe results in no reduction in pipe diameter or normal stress. Besides, the higher stiffness of the steel pipe can attract a higher load due to negative arching. As a result, the compaction-induced stress experienced by MDPE and steel pipes may differ significantly.

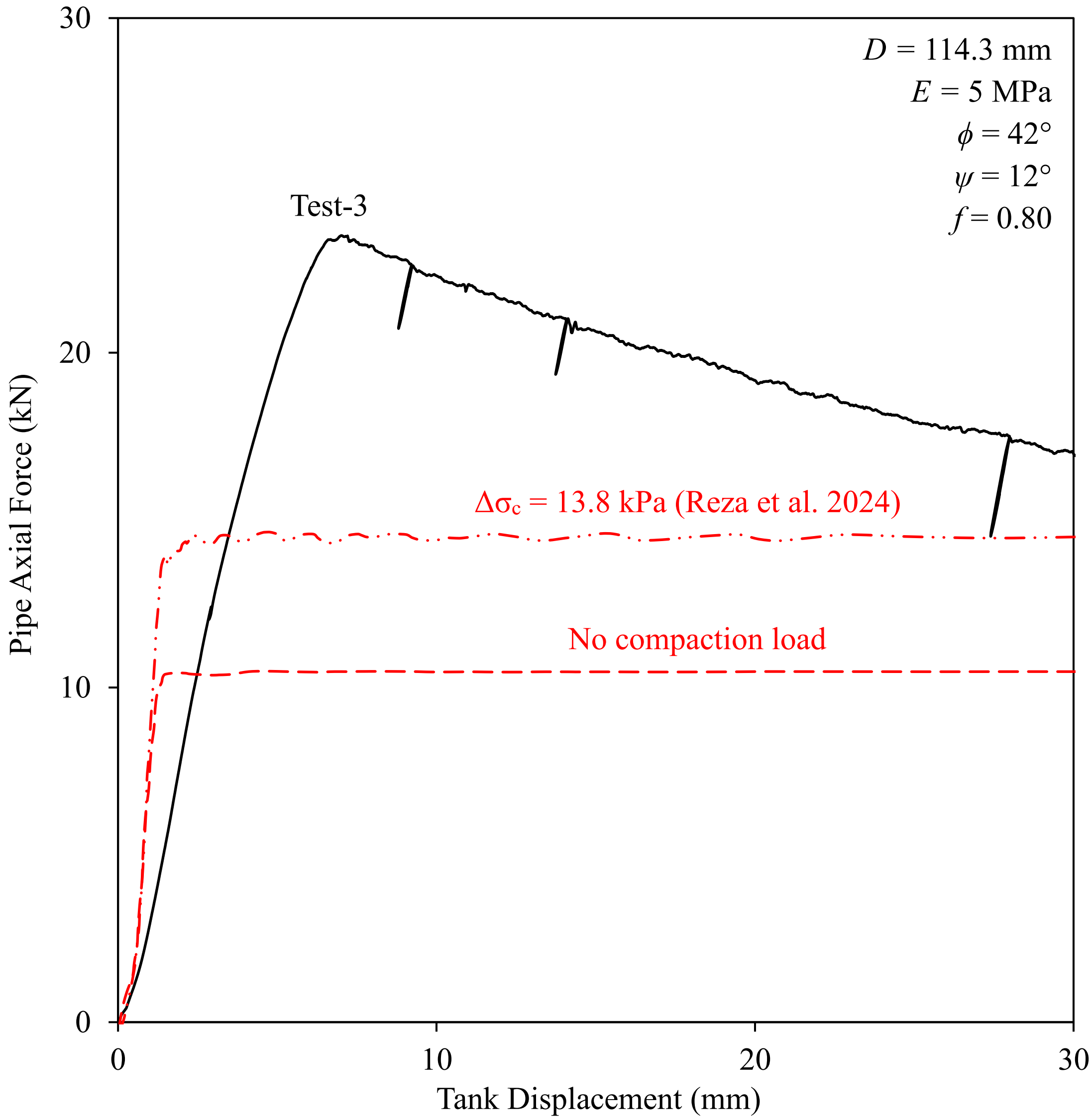

Figure 4.13: Comparison of FE analysis and full-scale laboratory Test-3 (Compaction model)

An attempt was made to increase the magnitude of compaction-induced stress in Abaqus for the steel pipe that provided the maximum axial force measured during the test. At the pipe springline level (i.e., 625 mm), the compaction-induced stress of 31 kPa was found to simulate the maximum pulling force. This stress was simulated during FE analysis using a fictitious temperature of 122 °C. The resulting distributions of horizontal stress and fictitious temperature are shown in Figures 4.14 and 4.15.

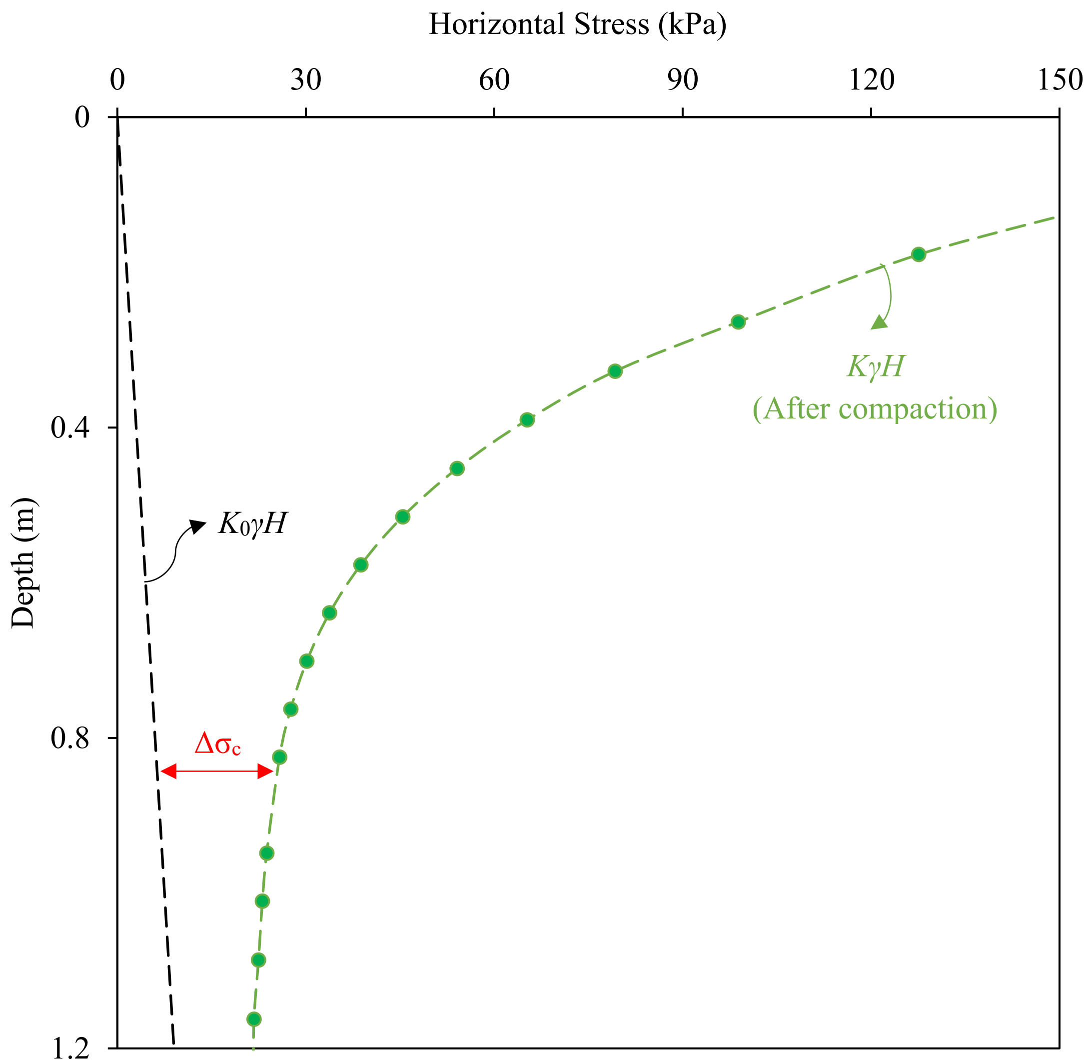

Figure 4.14: Distribution of horizontal stress (after Reza and Dhar 2024)

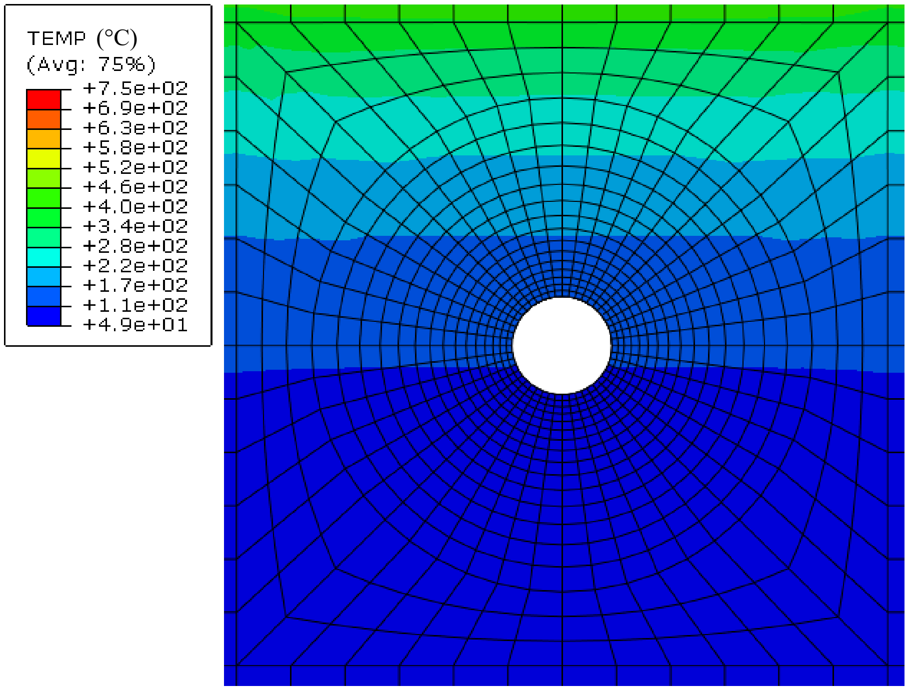

Figure 4.15: Applied temperature to soil domain (122 °C at springline level)

Figure 4.16 shows the force–displacement response of the Compaction model-based analysis and Test-3. The effect of compaction-induced stress is again evident in this figure. A compaction-induced stress of 31 kPa at the springline successfully predicts the peak axial force observed in Test-3. As mentioned earlier, the differences in the initial slope may be due to the use of the linear elastic–perfectly plastic Mohr–Coulomb model for the soil domain, whereas in real field conditions, a nonlinear stress–strain relationship might be expected. Similar to the K model, a higher accumulation of plastic strain (maximum 4.7%) was also observed at the pipe springline level than at the pipe crown and invert.

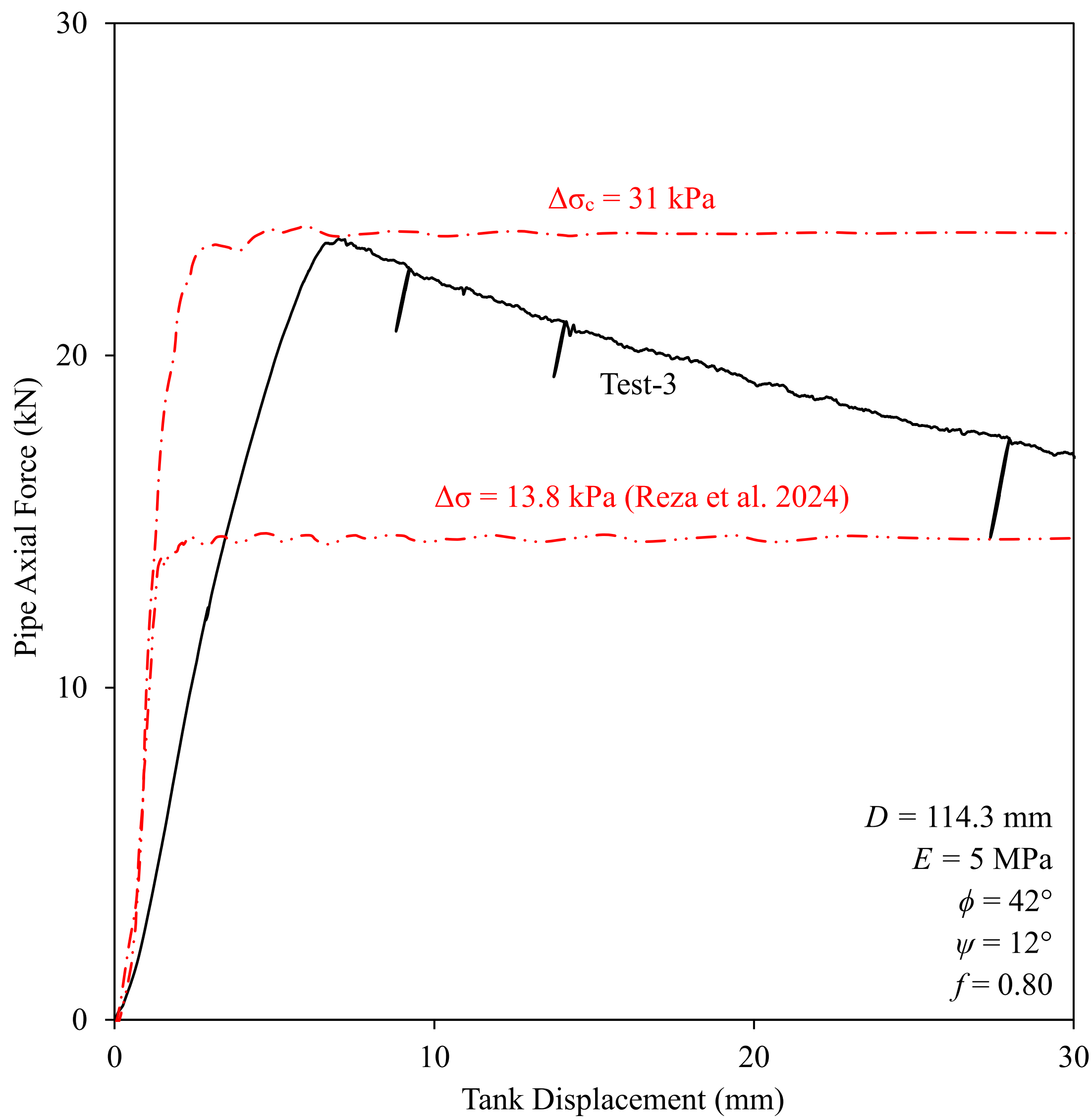

Figure 4.16: Comparison of FE analysis and full-scale laboratory Test-3 (Compaction model)

The distribution of normal stress around the pipe circumference is shown in Figure 4.17. Similar to the K model, the normal stress distribution was uniform throughout the entire length of the pipe. As expected, a higher concentration of normal stress was observed near the trailing end of the pipe (at 0.90L), indicating the boundary wall effect.

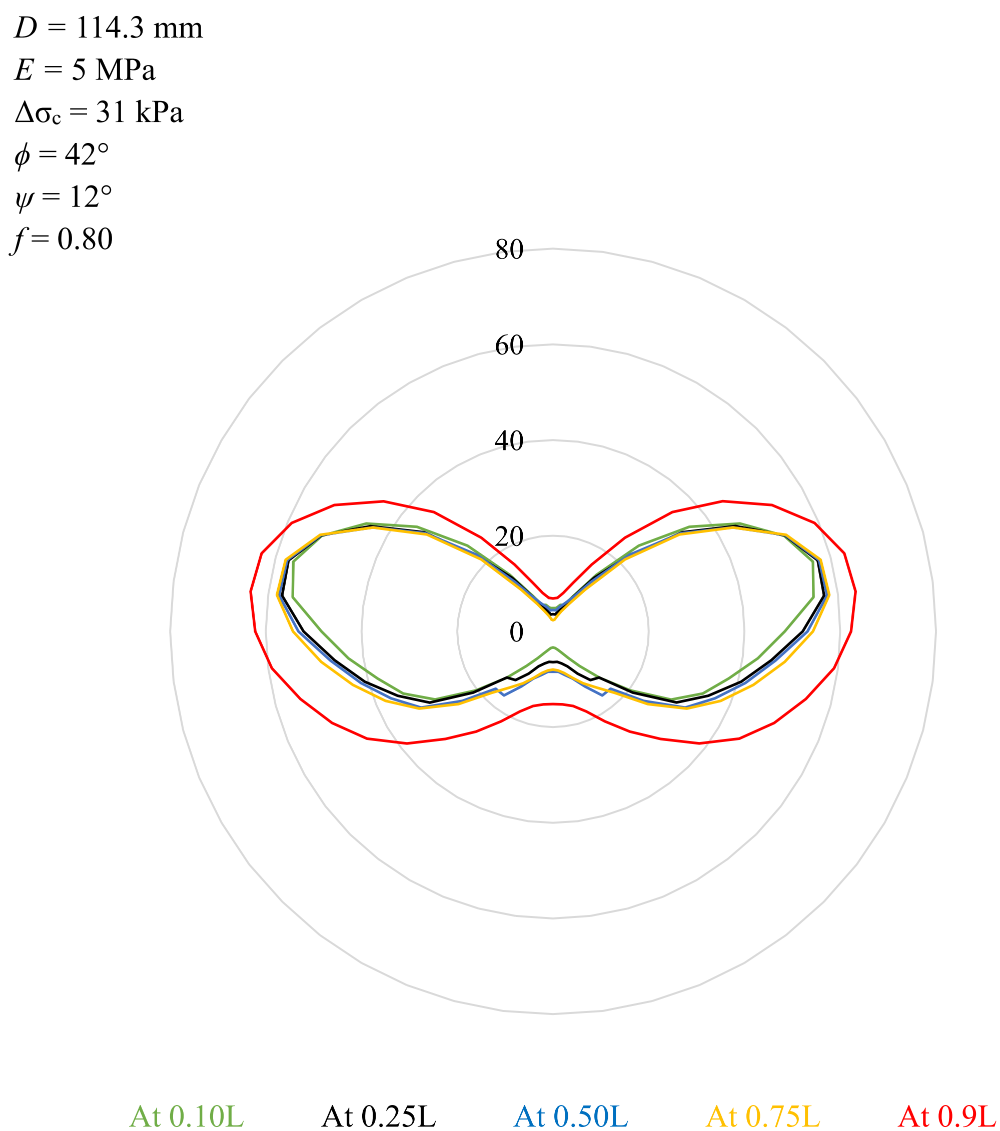

Figure 4.17: Distribution of normal stress (in kPa) around the pipe circumference at peak axial force (Compaction model)

Figure 4.18 shows the distribution of normal stress with the tank displacement at the pipe mid-section. Similar to the K model, a significant increase in the normal stress (~ 17 kPa) was observed at the springline level, which can be attributed to the compaction-induced stress. However, no significant increase in normal stress was observed at the pipe crown and invert. Note that a slight increase in the overall average stress (~ 3.5 kPa) was observed initially during the pulling step, indicating the negligible effect of shear-induced dilation even for analysis based on the compaction model.

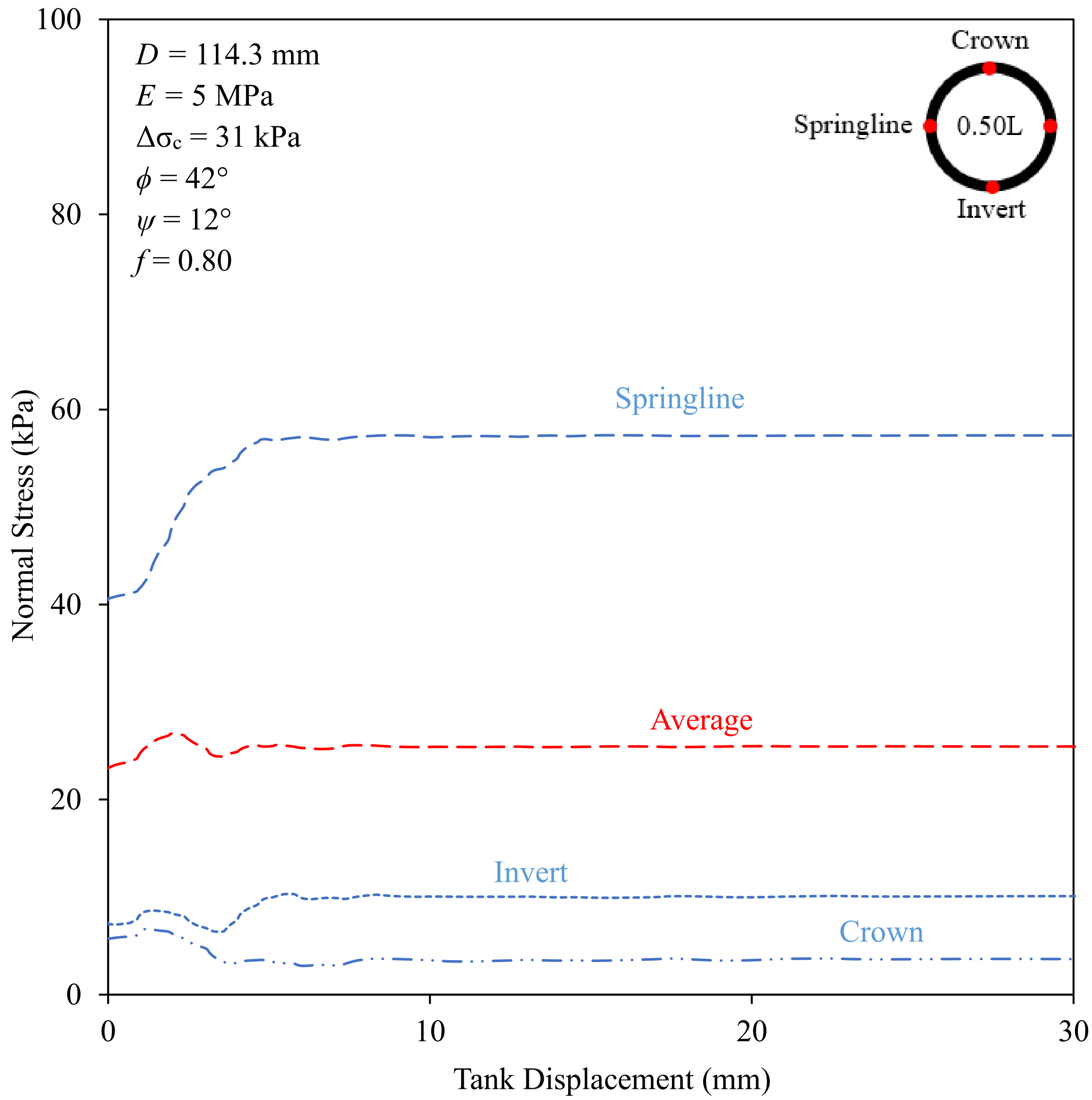

Figure 4.18: Distribution of normal stress with tank displacement (Compaction model)

The distribution of average circumferential shear stresses at the 0.50L and 0.75L sections of the pipe with respect to the tank displacement is shown in Figure 4.19. As the relative displacement between the pipe and the surrounding soil developed, the shear stress at each point increased, eventually reaching the peak shear strength. Notably, the distribution of average shear stress remained uniform across the sections, with the peak shear stress observed at ~ 16.5 kPa.

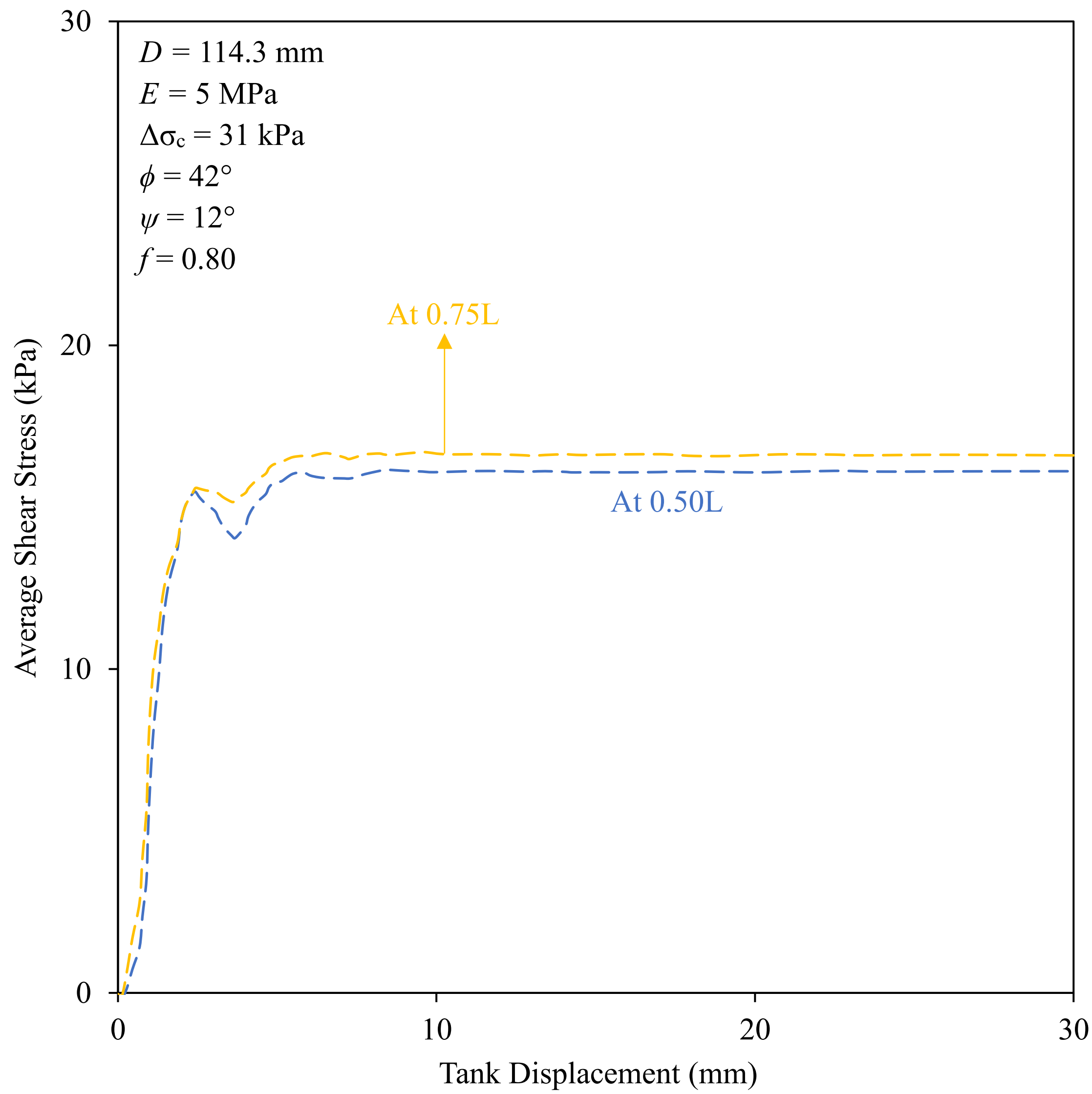

Figure 4.19: Distribution of average shear stress at 0.50L, and 0.75L (Compaction model)

The axial strain at the pipe crown was also monitored using the results of the FE analysis. Figure 4.20 shows the axial strain distribution along the entire length of the pipe, derived from FE analysis. As expected, the axial strain was highest at the fixed pipe end and progressively decreased to a minimum at the other end. Note that the highest strain value in FE analysis is significantly below the typical yield strain (i.e., 0.2%) for steel pipes subjected to axial ground movement. The observed variations in strain distribution with different tank displacements are likely attributed to post-peak fluctuations in the response.

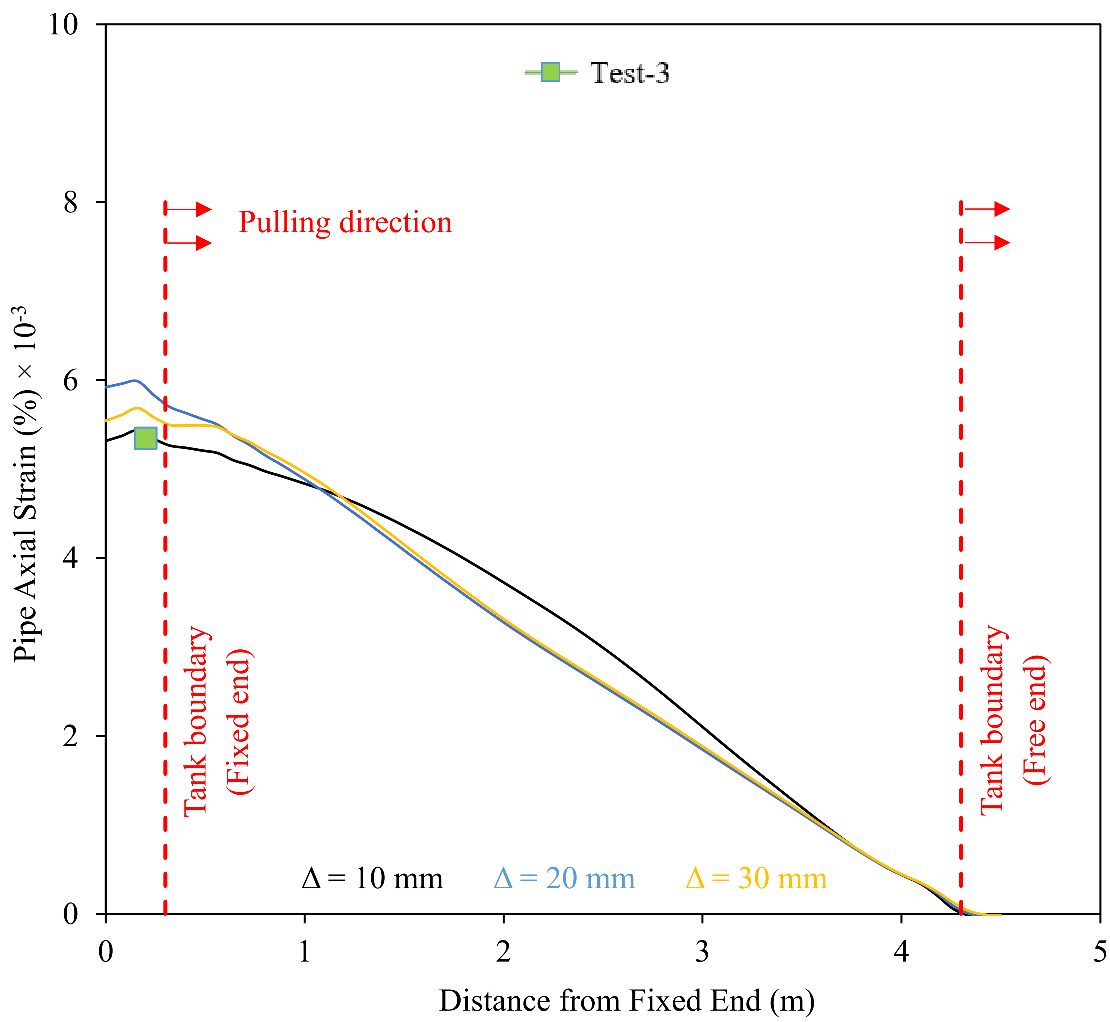

Figure 4.20: Lengthwise axial strain distribution on the crown

4.8 Use of Radial Expansion (Cavity Expansion Model)

Although the analysis presented above revealed that compaction-induced stresses play an important role in the axial frictional force at the soil-pipe interface, it is generally believed that shear-induced dilation is responsible for the higher axial force for pipes in dense sand. Wijewickreme et al. (2009) applied radial expansion of the shear band around the pipe to mimic the shear-induced dilation effects in dense sand. However, the thickness of the shear band is closely related to the mean particle diameter (d_{50}). Roscoe (1970) reported that when Leighton Buzzard sand was sheared, it failed within the thinnest possible zone, with the thickness of the failure zone being ten times the particle diameter ($10d_{50}$). Later, Bridgwater (1980) theoretically confirmed the shear band thickness proposed by Roscoe (1970) using statistical mechanics methods. DeJaeger (1994) experimentally demonstrated that the shear band thickness for fine sand ranged from 5 to 10 mm and from 12 to 20 mm for coarse sand. Karimian (2006) reported the thickness of the active shear zone for Fraser River sand to be between 1.2 and 2.8 mm, based on measurements in the colored sand zone, which was also comparable to $10d_{50}$ (i.e., 2.3 mm). In their discrete element analysis, Meidani et al. (2018) also suggested using $10d_{50}$ as the active shear zone thickness for Fraser River sand. To end this, the thickness of the active shear zone for locally manufactured sand used in this study can be approximated as 7.42 mm (i.e., $10d_{50}$).

Karimian (2006) also conducted a series of direct shear tests on Fraser River sand to assess the level of dilation during shearing until the constant volume phase was reached. It was reported that the average vertical deformation was around 30% of the thickness of the active shear zone. Based on this, it is reasonable to consider a maximum radial expansion of 2.2 mm (i.e., 30% of 7.42 mm) at the interface for numerical modeling.

An attempt was made to radially expand the pipe to simulate shear-induced dilation effects in dense sand. A uniform temperature was applied to the pipe section in the predefined field module to achieve a radial expansion of 2.1 mm. Expansion in the axial direction (along the pipe's length) was restricted, while an expansion coefficient of 1.1×10^{-5} /°C was applied in the cross-sectional plane of the pipe. All other properties were kept the same as described in Section 4.4. The change in diameter after the application of thermal load is shown in Figure 4.21.

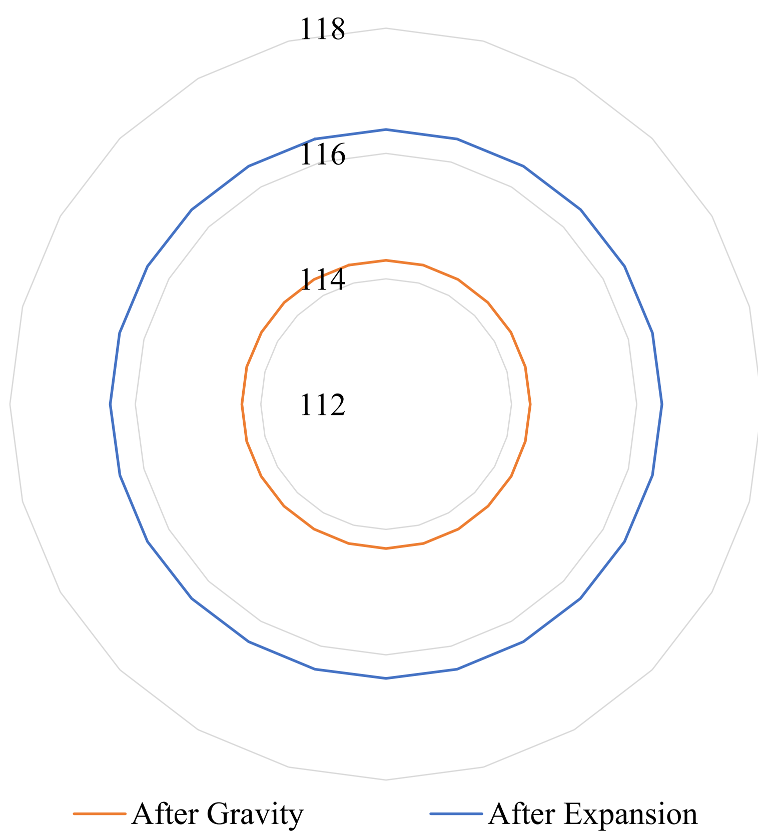

Figure 4.21: Expansion of pipe diameter (mm)

At the end of the gravity loading phase, the expansion model recorded a maximum vertical settlement of 1.95 mm. Additionally, the kinetic energy of the model also remained within the specified limit (5-10%) of the internal energy. The force–displacement responses of the Expansion model and Test-3 are shown in Figure 4.22.

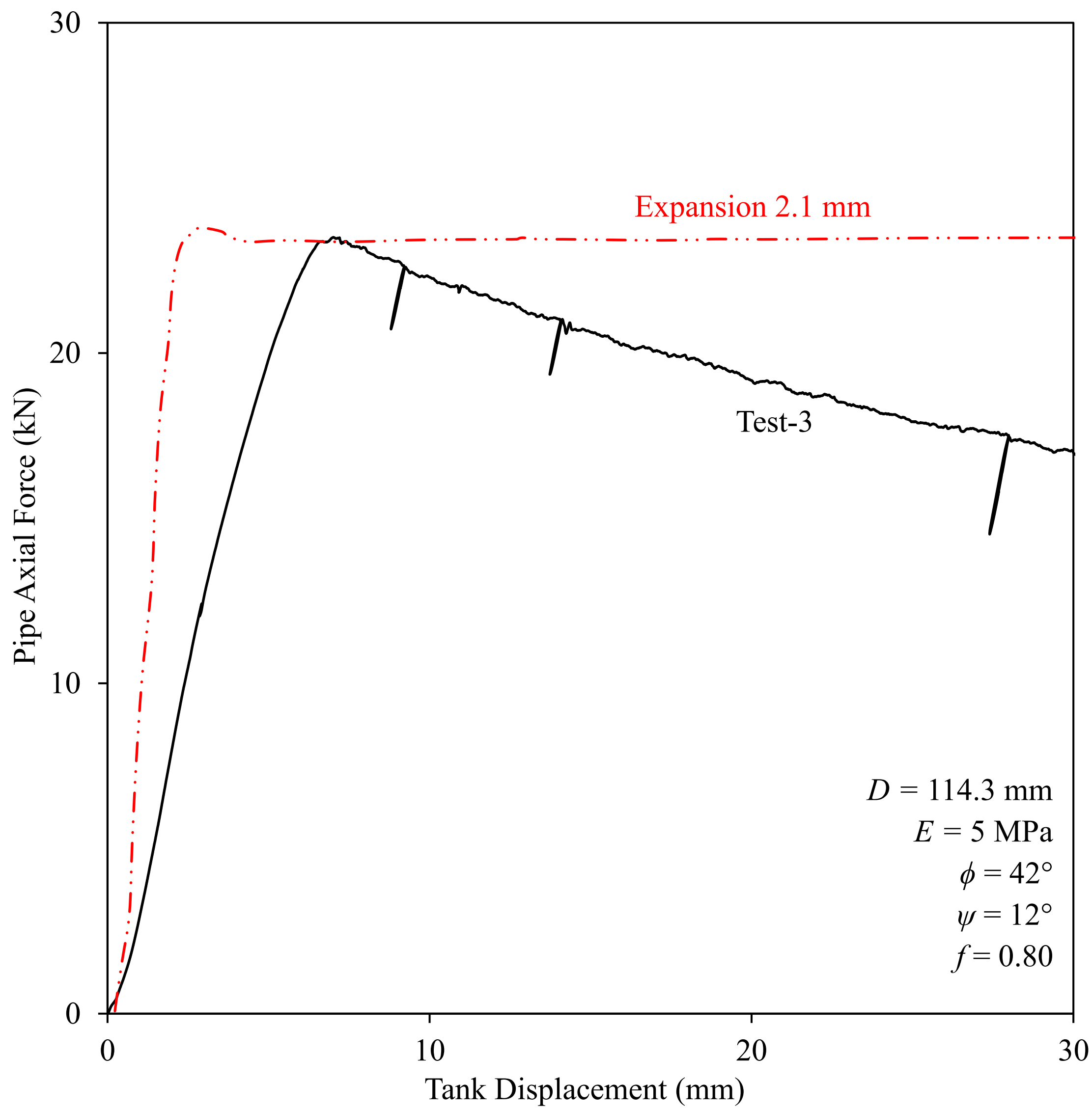

Figure 4.22: Comparison of FE analysis and full-scale laboratory Test-3 (Expansion model)

It is evident that a radial expansion of 2.1 mm successfully predicts the peak axial force (i.e., Test-3) experienced by a 114.3 mm pipe subjected to axial ground loading. Note that the backfill soil was compacted using the hand-tamper method for Test-3. To simulate the effect of the vibratory plate compactor on the peak axial load, a larger radial expansion may be required. The distribution of normal stress around the pipe circumference at a distance of 0.50L is shown in Figure 4.23.

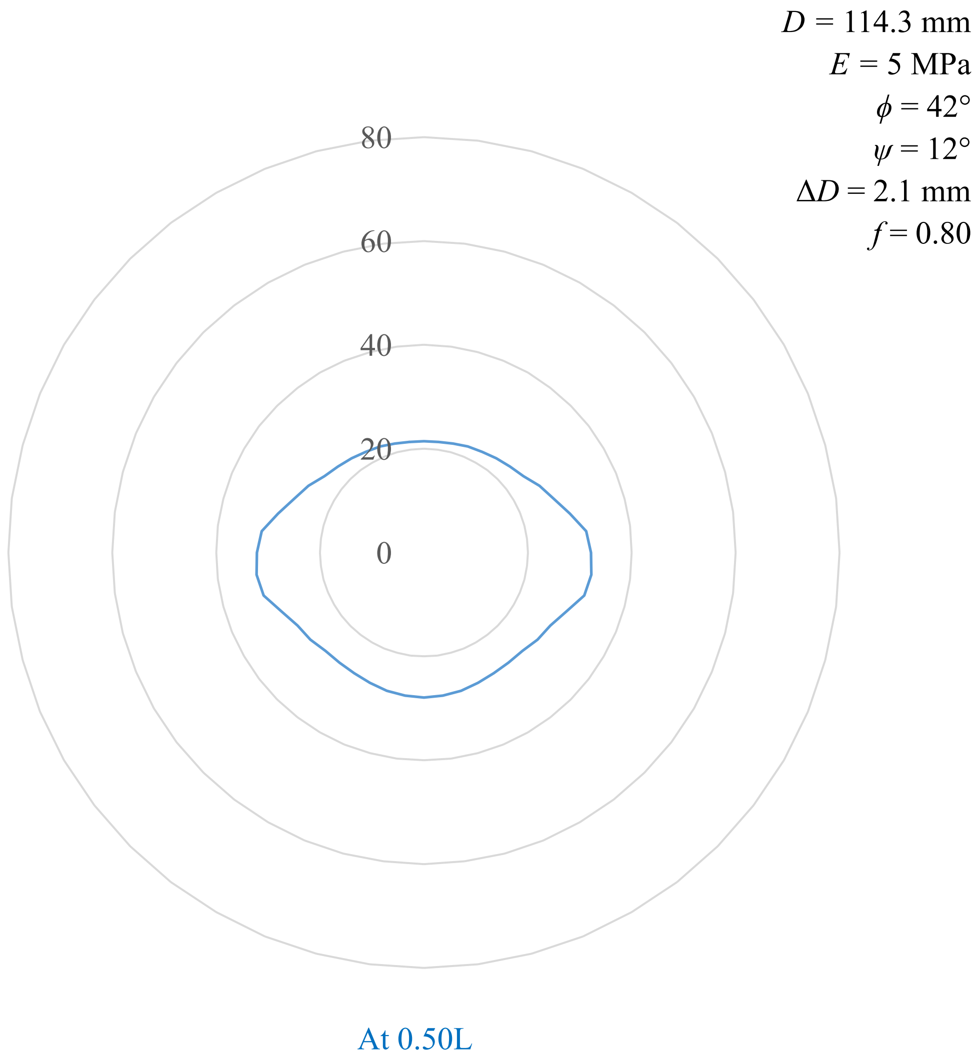

Figure 4.23: Distribution of normal stress (in kPa) around the pipe circumference at peak axial force (Expansion model)

As expected, relatively higher normal stress was observed at the pipe springline level. However, in the case of the Expansion model, the stress concentration was more localized, affecting only a thin zone of soil around the pipe. As a result, the normal stress at peak axial force was comparatively lower than that observed in the K and Compaction model approaches.

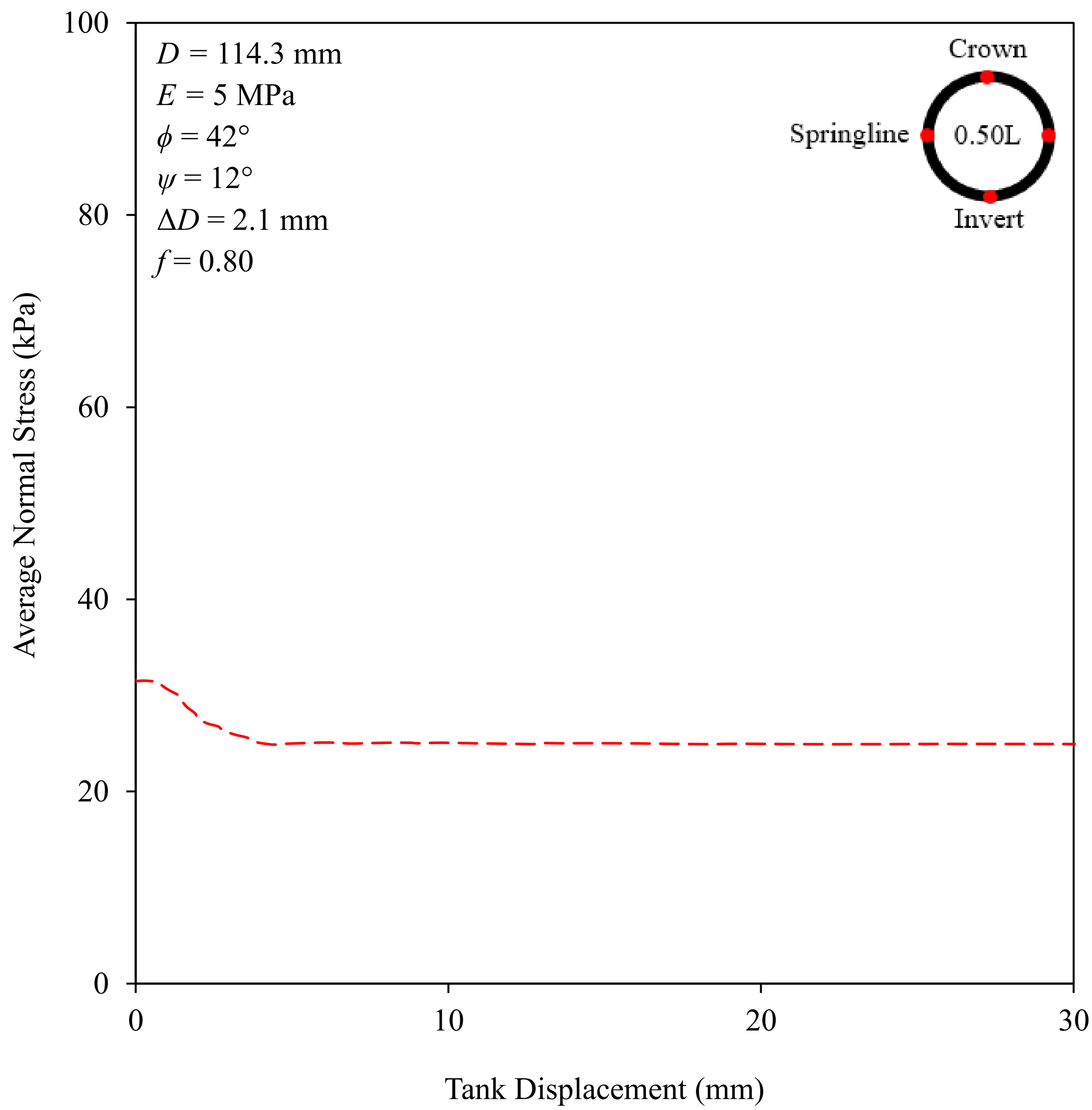

Figure 4.24: Distribution of normal stress with tank displacement (Expansion model)

A drop of approximately 6.5 kPa in average normal stress was observed in the Expansion model during the pulling step, indicating lower contact pressure on the pipe (Figure 4.24). On the other hand, the average shear stress distribution was uniform across the sections, with the peak average shear stress varying between 16 kPa and 17 kPa, as shown in Figure 4.25.

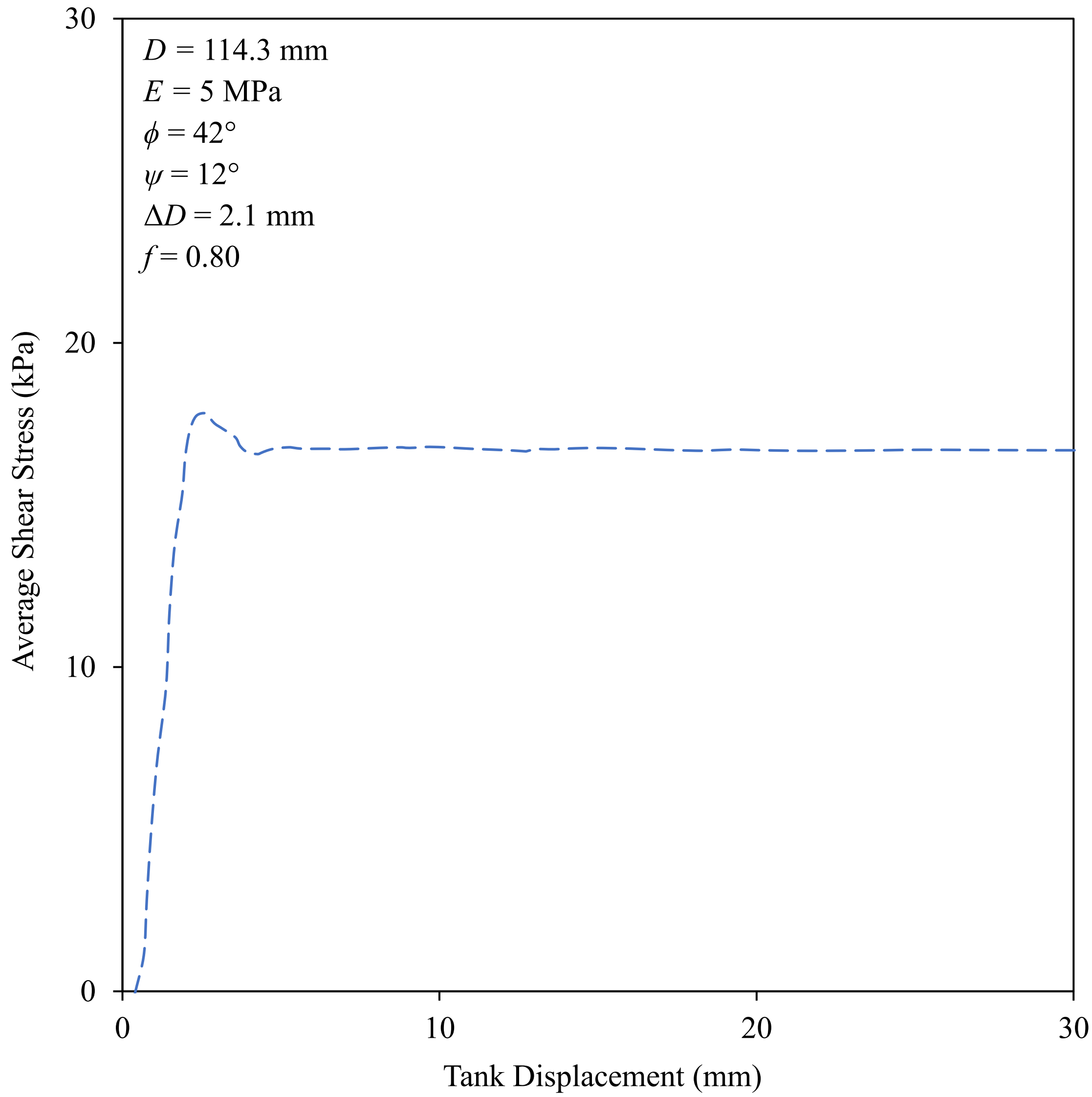

Figure 4.25: Distribution of average shear stress at 0.50L (Expansion model)

4.9 Effect of Inclination Angle

As discussed earlier in Chapter 2, the present design guidelines (ALA 2005, PRCI 2009) consider the pipeline as a beam, with the interaction between the soil and pipeline modeled as orthogonal soil springs in the axial, traverse-horizontal, and traverse-vertical directions. It is important to note that the stiffness of these springs in the three directions is independent, indicating that the deformation of soil springs in one direction does not affect the soil springs in the other directions. However, in real ground movement scenarios, the relative soil movement may not be confined to a single direction but rather involves a combination of both axial and transverse components (i.e., oblique loading) (Nyman 1984, Hsu 1996, Guo 2005, Daiyan et al. 2011, Farhadi 2013, Morshed 2019, Ye et al. 2024).

It is important to understand how deviating from a pure axial loading condition impacts the interaction between the buried pipeline and the surrounding soil. A numerical study was carried out to investigate the effects of the inclination angle on the soil-pipeline response, both in the horizontal and vertical planes. For this analysis, a small inclination angle of 5° was chosen. This slight inclination from pure axial loading helps to understand the effects of pipeline misalignment in full-scale laboratory tests.

The compaction model approach was employed to compare the force–displacement responses between axial and oblique loading conditions, as shown in Figure 4.26. When the inclination angle was in the vertical plane, the average burial depth decreased to ~ 450 mm. As a result, a reduction in the axial force at the fixed pipe end was observed compared to the pure axial condition. A similar observation was also made using the K model.

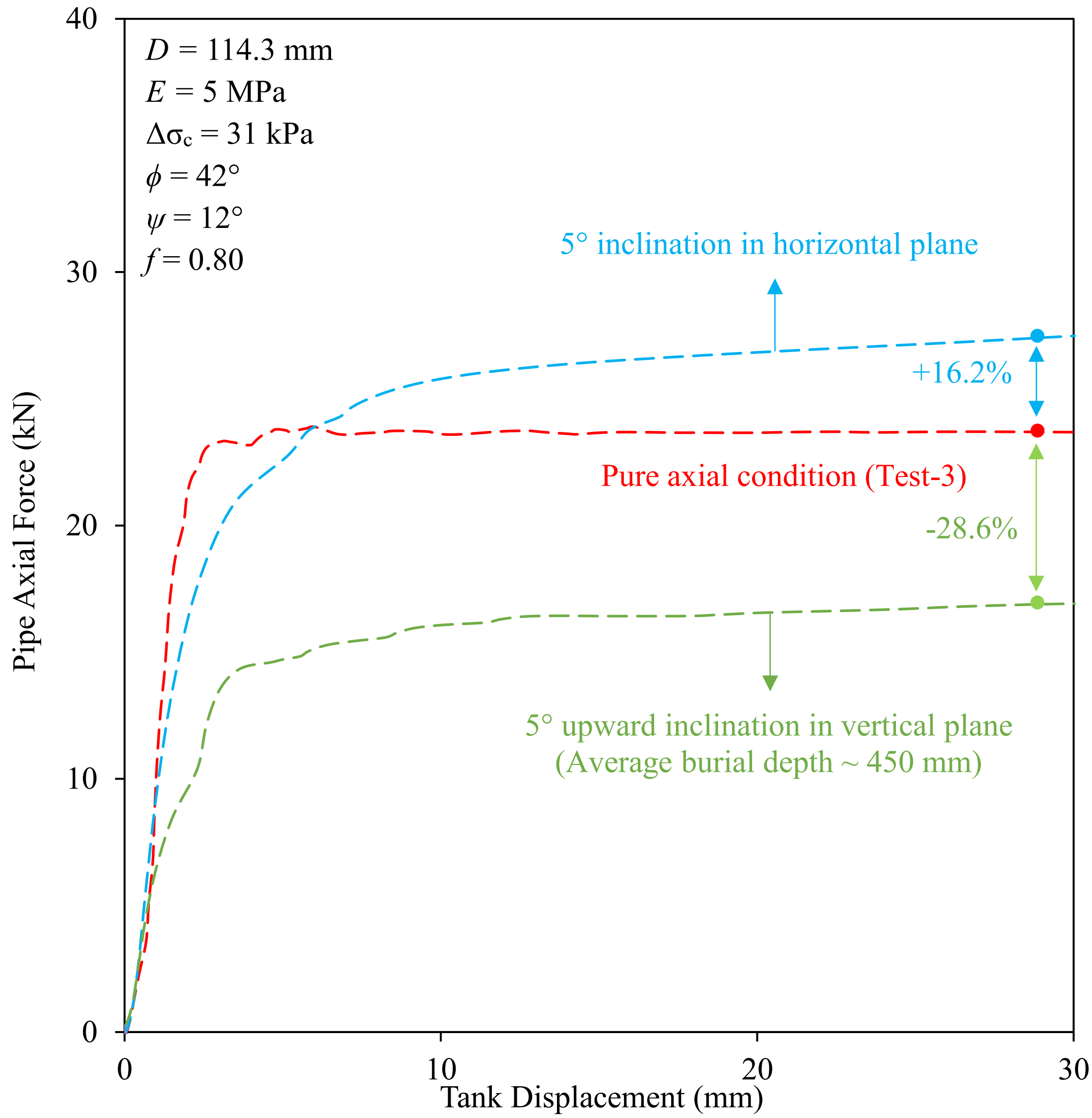

Figure 4.26: Force–displacement responses for oblique loading conditions

A significantly higher axial interacting force (16.2%) was observed for the horizontal oblique loading condition though there was no change in burial depth (i.e., 625 mm). The increase in the axial interacting force can be attributed to the increased normal pressure at the interface. It is also evident that to reach the peak axial force for oblique loading, a larger relative displacement was required. Similar numerical observations were also made by Daiyan et al. (2011).

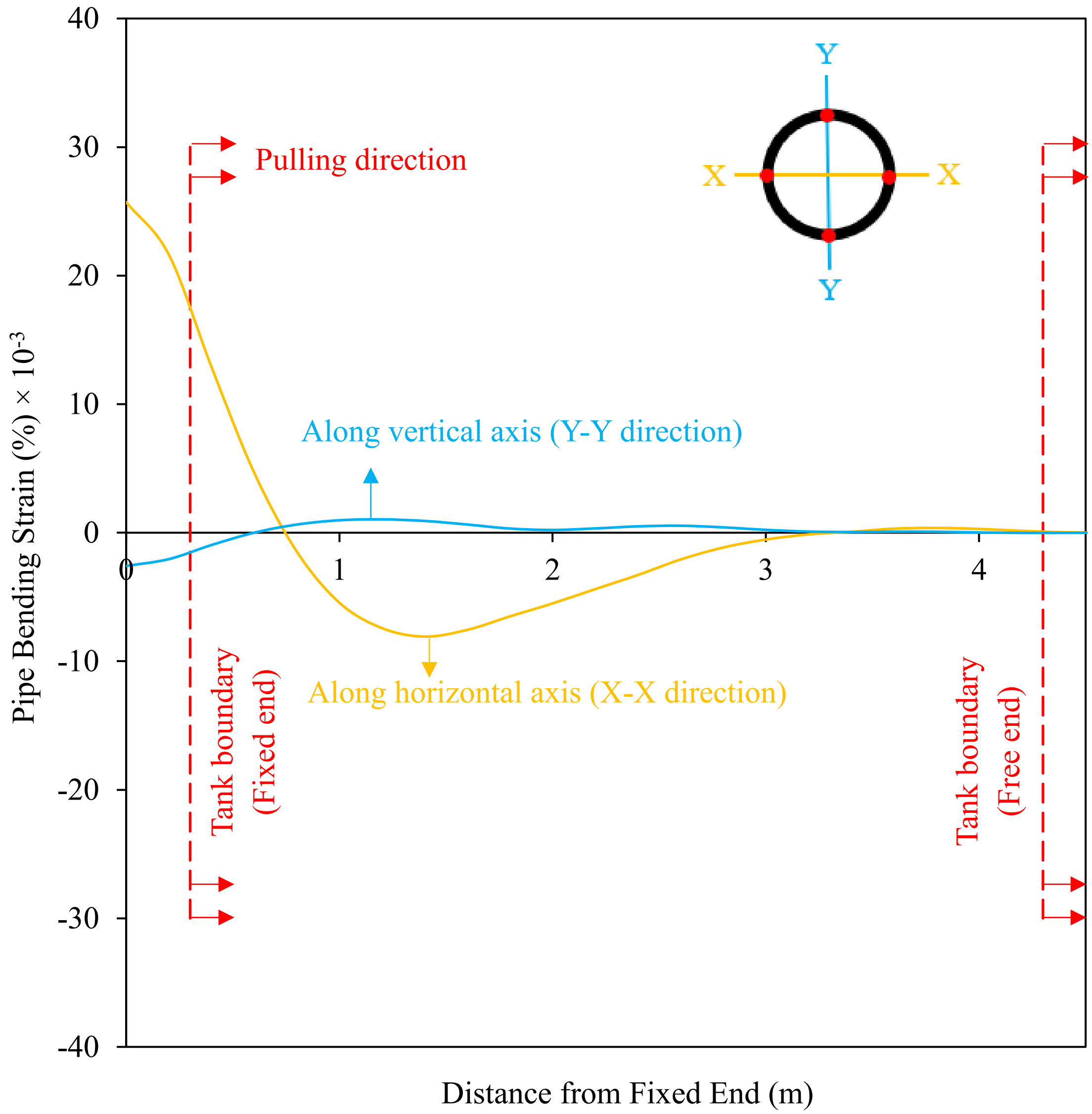

Figure 4.27: Bending strain distribution for the horizontal oblique condition

When the loading condition changes from pure axial to oblique, both axial and bending strains are induced in the pipeline. From FE analysis, it was evident that the maximum axial strain at the fixed pipe end resulting from horizontal oblique loading (~0.032%) was notably higher than the axial strain observed under pure axial conditions (~0.006%). Bending strains can also be calculated by taking one-half of the difference in axial strain readings between the two extreme points on the pipe wall. Figure 4.27 shows the distribution of bending strain along the pipe length. The bending strain in the horizontal direction was significantly higher than in the vertical direction, indicating that bending was more pronounced for inclination on the horizontal plane.

4.10 Parametric Study

A parametric study was also carried out to investigate the effects of various soil parameters and interface friction factors. The modulus of elasticity of soil (E_s) was varied from 2 MPa to 15 MPa to observe how soil stiffness affects the axial force on the pipeline. The peak friction angle was changed from (ϕ) 38° to 48°. Additionally, the effect of dilation was studied on peak pipe axial force by varying the dilation angle (ψ) from 5° to 18°. The interface friction factor (f) was also studied to determine the effect of pipe roughness by changing the values from 0.5 to 0.9. The following sections will briefly discuss the effects of each of these parameters on the peak pipe axial force.

4.10.1 Effect of Soil Parameters

Figure 4.28 shows the relationship between peak axial force and soil modulus for a burial depth of 625 mm. The mean effective confining pressure (p') was varied from 1.5 kPa to 100 kPa at the pipe springline level. It is evident that an increase in soil modulus resulted in an increase in peak axial force. As the mean effective confining pressure increased, the soil surrounding the pipe became stiffer, resulting in increased normal pressure on the pipe surface. Therefore, higher peak axial forces are expected for higher values of Young's modulus of elasticity of soil.

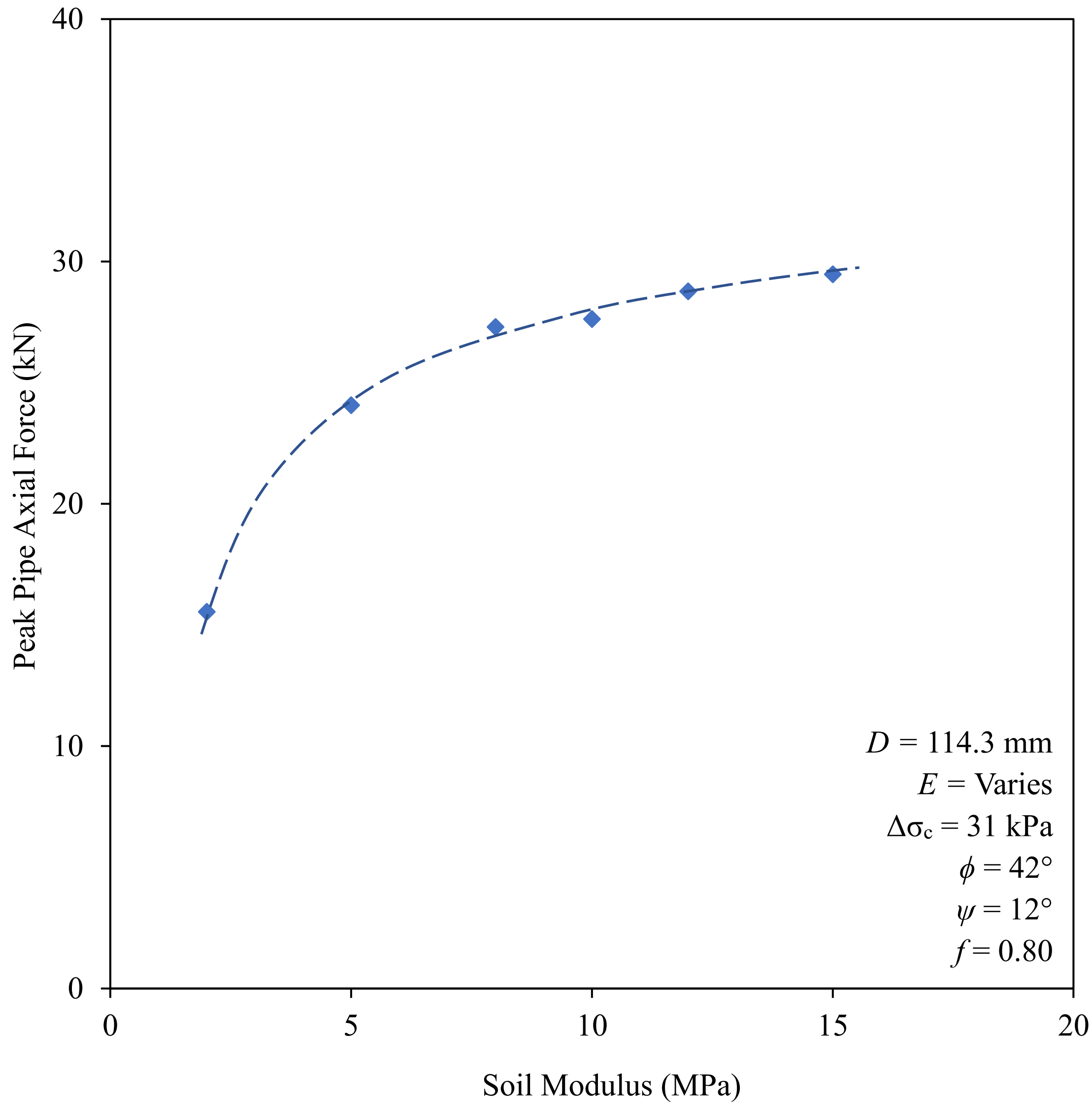

Figure 4.28: Effect of soil modulus on peak pipe axial force

Figure 4.29 shows the effect of the interface friction angle of soil on the peak axial forces. Six different soil friction angles (i.e., 38°, 40°, 42°, 44°, 46°, and 48°) were studied. The interface friction factor was kept constant (f = 0.80) throughout the analysis. As shown in Figure 4.29, the peak axial force slightly increased as the friction angle increased. When the friction angle was increased by 5°, the axial soil resistance was increased by ~ 6.5%.

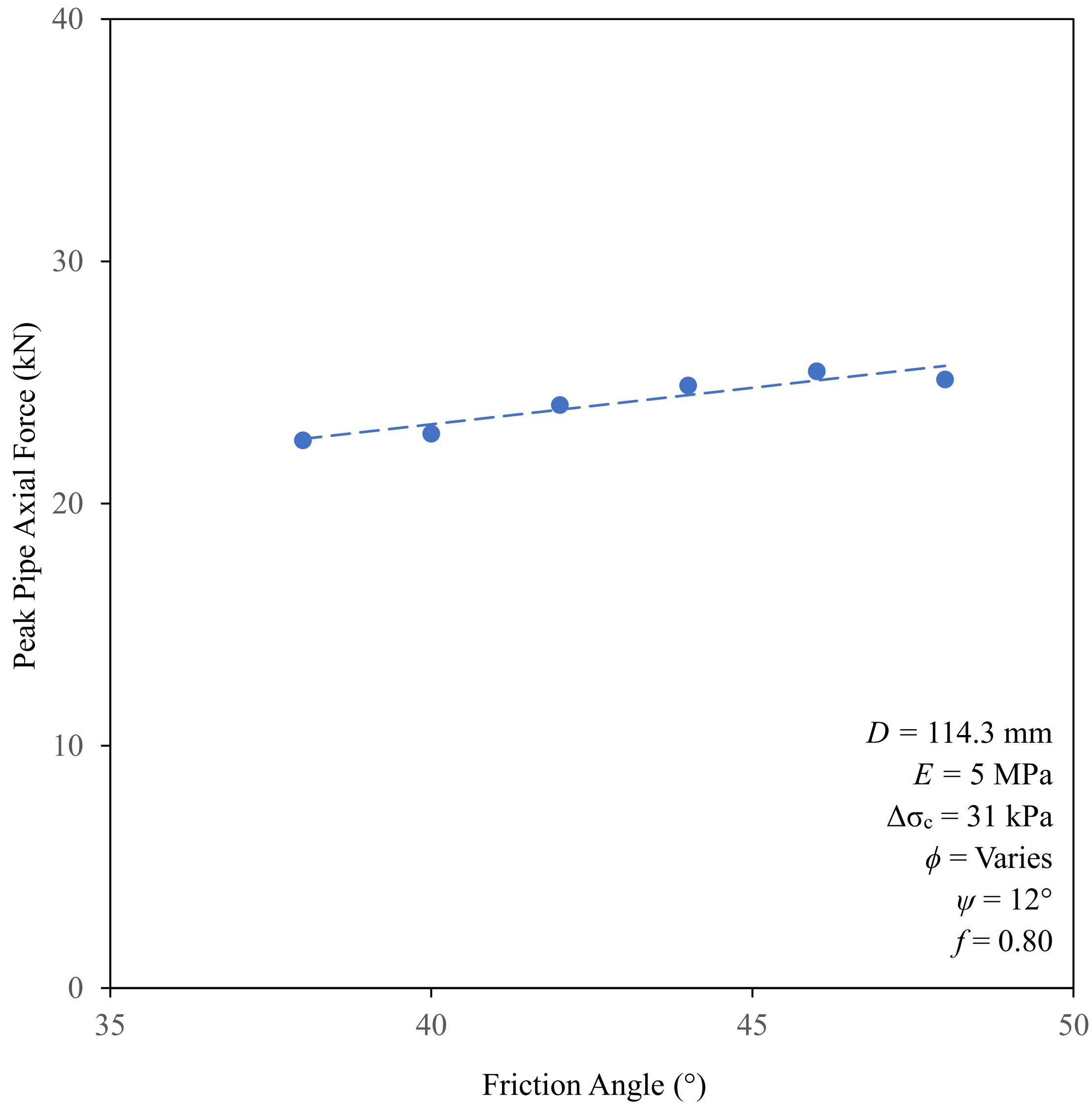

Figure 4.29: Effect of friction angle on peak pipe axial force

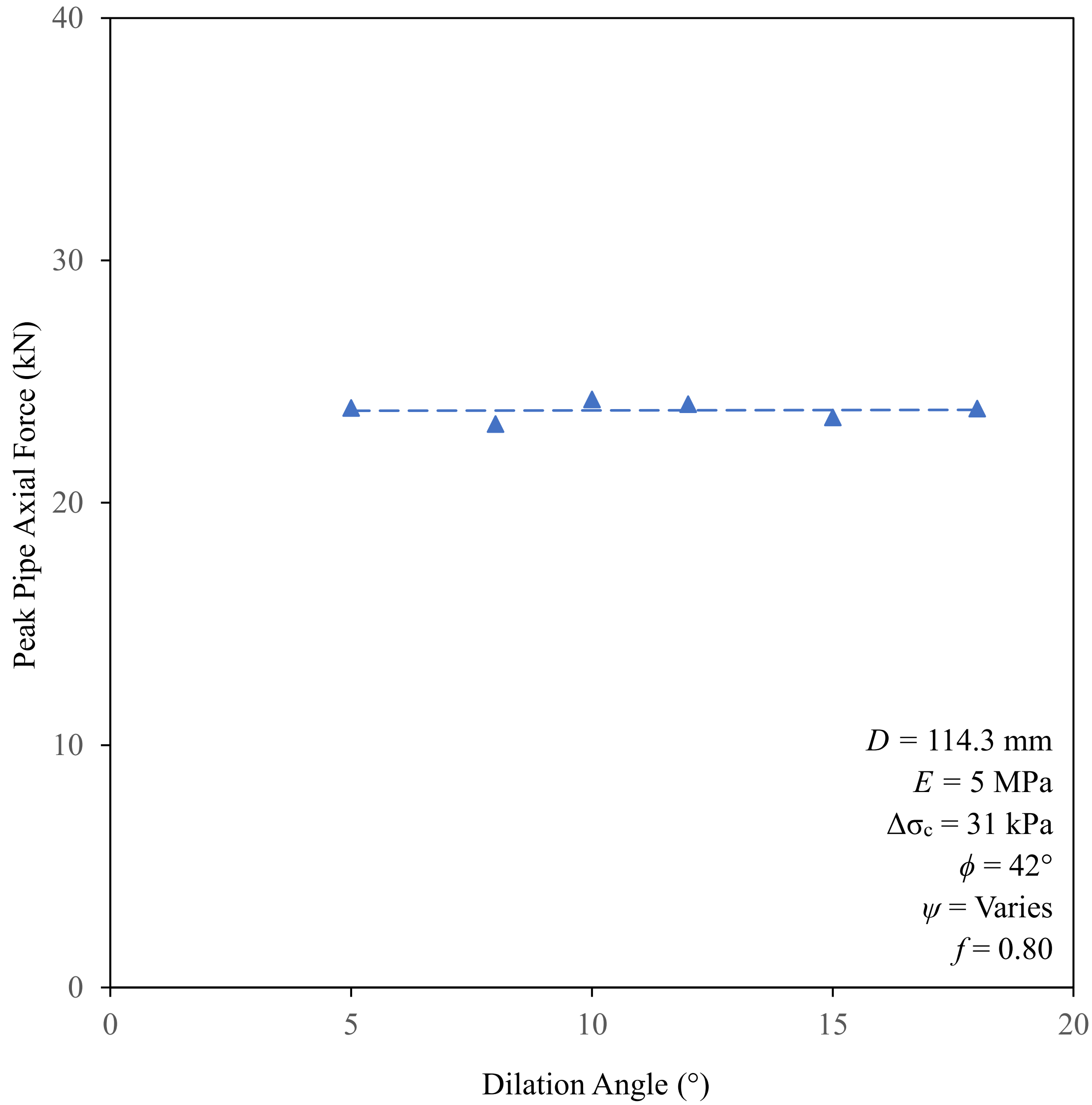

Figure 4.30: Effect of dilation angle on peak pipe axial force

The effect of different soil dilation angles on peak axial force is shown in Figure 4.30. Notably, the peak soil resistance did not change significantly when the dilation angle was varied from 5° to 18°. The normal stress distribution, as discussed in Sections 4.6 to 4.8, also demonstrated that the effect of dilation was either absent (K model and Expansion model) or negligible (Compaction model) during the soil pulling step, specifically for smaller diameter pipe. The variations in peak axial load from the design guidelines may be associated with compaction-induced energy or the surface roughness of the pipe. However, shear-induced dilation is believed to contribute mainly to the higher axial force on pipes. More studies on compaction-induced energy and pipe surface roughness are necessary to confirm their effect on axial soil resistance.

4.10.2 Effect of Interface Friction Factor

The response of buried pipelines subjected to axial ground loading can be significantly affected by the surface roughness and coating thickness of the pipes. Design guidelines (ALA 2005, PRCI 2009) recommend a friction factor of 0.7 for smooth steel pipes and 0.8 for rough steel pipes. Guo and Zhou (2024) conducted a series of full-scale laboratory tests and reported that the surface roughness of 102 mm steel pipes increased the peak pullout resistance by 72-79%, whereas shear-induced dilation increased the resistance by 21-28%. The effect of surface roughness was more significant than shear-induced dilation, especially for small-diameter steel pipes.

To investigate the effect of surface roughness, the interface friction factor was varied from 0.5 to 0.9. Figure 4.31 shows the relationship between the interface friction factor and peak pipe axial force. As expected, the peak pipe axial force increased significantly with the higher friction factors. This increase in pipe axial force can be attributed to the interlocking of soil particles with the pipe surface. As surface roughness increases, more soil particles embed into the pipe surface, resulting in higher shear resistance. As a result, a higher axial force is required to overcome frictional resistance when there is a relative ground movement.

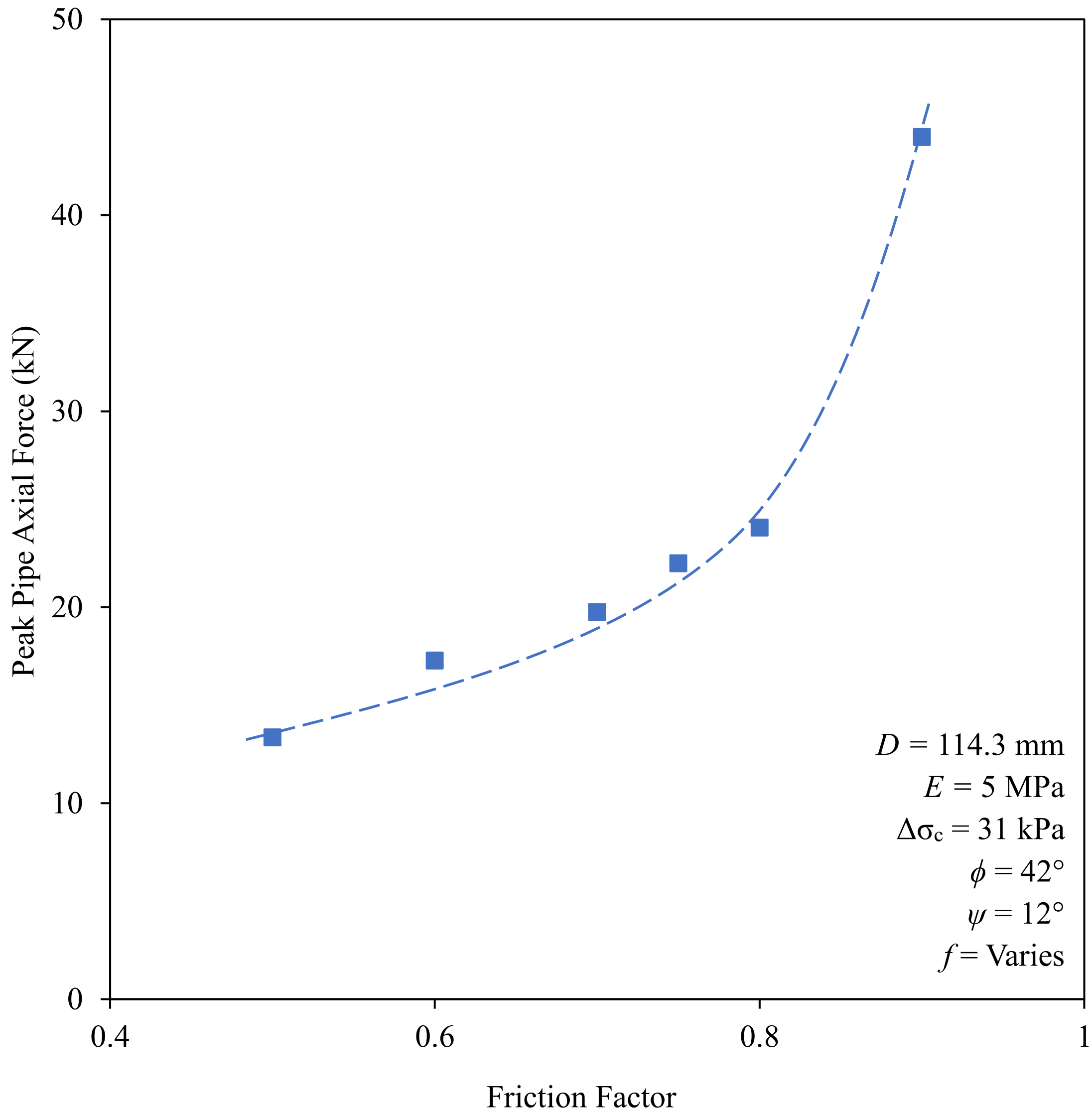

Figure 4.31: Effect of interface friction factor on peak pipe axial force

4.11 Conclusions

This chapter briefly discusses the development of FE modeling to simulate a full-scale laboratory test of 114.3 mm steel pipe (Test-3) subjected to axial ground loading. The classical Mohr–Coulomb plasticity was successfully employed to predict the peak pipe axial force. The following conclusions can be drawn from the above studies:

- The peak axial force can be successfully predicted using the value of the coefficient of lateral earth pressure recommended by Meidani et al. (2018) for pipe in backfill soil compacted with a hand tamper. However, the modified earth pressure coefficient is sensitive to the median grain size, so attention should be given to the mean grain size of the soil particles. Additionally, the effect of compaction energy was not considered in Meidani et al. (2018).
- The compaction model proposed by Reza et al. (2024) was unable to predict the peak axial force for the steel pipe. To simulate the peak axial force experienced by the 114.3 mm steel pipe, higher compaction-induced energy at the pipe springline level was needed. This discrepancy is likely due to the differences in the load transfer mechanisms between the MDPE pipe and the steel pipe.
- A uniform pipe radial expansion of 2.1 mm successfully predicted the peak axial force in Test-3. This method applies artificial expansion to account for the shear-induced dilation. To better assess the level of dilation at the interface, additional laboratory tests will be required. It is important to note that in Test-3, the backfill soil was compacted using a hand tamper. For Test-7, where the backfill was

compacted with a vibratory plate compactor, a larger radial expansion will be needed to simulate the test results.

- The normal stress distribution around the pipe circumference was uniform along its length. However, higher normal stress was observed towards the trailing end of the pipe due to the boundary effect of the tank wall. In the Expansion model, the stress concentration was more localized, leading to lower normal stress compared to the values observed in the K and Compaction models.
- The shear stress distribution was found to be uniform across the sections of the pipe in each model, with peak values ranging from 15 to 18 kPa.
- The pipe wall stress was analyzed using the maximum von Mises stress. Compared to the trailing pipe end sections, a higher stress concentration (~ 13.5 MPa) was observed at the fixed pipe end, as expected.
- The axial strain distribution from the FE analysis on the pipe crown near the fixed pipe end was comparable to that observed in the full-scale laboratory test (0.006% vs. 0.005%). However, the maximum strain values were significantly well below the typical yield strain (0.2%) for steel pipes subjected to axial ground movement.
- When the loading condition changed from pure axial (i.e., 0°) to a 5° horizontal oblique, both the axial and traverse interacting forces increased. The increase in forces can be attributed to the increase in normal stress around the pipe. Additionally, both axial and bending strains were induced on the pipeline under the horizontal oblique condition.

- The parametric study showed that the pipe axial force was primarily influenced by the soil modulus, soil friction angle, and the surface roughness of the steel pipe. The effect of dilation was not evident from the parametric study.

4.12 Reference

ALA (American Lifelines Alliance). 2005. Guidelines for the design of buried steel pipe, Reston, VA, USA.

Al-Khazaali, M. and Vanapalli, S. K. 2019. A novel experimental technique to investigate soil–pipeline interaction under axial loading in saturated and unsaturated sands. *Geotechnical Testing Journal*, 43 (1), 70–93.

Almahakeri, M., I. D. Moore, and A. Fam. 2019. Numerical techniques for design calculations of longitudinal bending in buried steel pipes subjected to lateral earth movements, *Royal Soc. Open Sci.*, 6 (7): 181550.

Andersen, D. 2024. Behavior of small-diameter buried steel pipes subjected to axial ground movement, *M.Eng. thesis*, Memorial University of Newfoundland, Canada.

Anzum, S. and Dhar, A. S. 2024. Three-dimensional finite-element modeling of polyethylene pipes in dense sand subjected to a lateral force, *Journal of Pipeline Systems Engineering and Practice*, 15 (3).

Barrett, J., and Phillips, R. 2020. Formulation of 3D soil springs for pipe stress analyses, In proc., *13th International Pipeline Conference*, American Society of Mechanical Engineers.

Bridgwater, J. 1980. On the width of failure zones. Géotechnique, 30 (4): 533–536.

Budhu, M. 2010. Soil mechanics and foundations, 3rd ed.; John Wiley & Sons, Inc.: Hoboken, NJ, USA, ISBN 978-0-470-55684-9.

Chakraborty, T., and R. Salgado. 2010. Dilatancy and shear strength of sand at low confining pressures, *J. Geotech. Geoenviron. Eng.*, 136 (3): 527–532.

Daiyan, N., Kenny, S., Phillips, R., Popescu, R. 2011. Investigating pipeline-soil interaction under axial lateral relative movements in sand. *Canadian Geotechnical Journal,* 48 (11): 1683-1695.

Dassault Systèmes 2019. ABAQUS/CAE user's guide. Providence, RI: Dassault Systèmes Simulia.

Davis, E.H. 1968. Theories of plasticity and the failure of soil masses, In Soil mechanics: Selected topics (ed. I. K. Lee), pp. 341–380. London: Butterworth.

DeJaeger, J. 1994. Influence of grain size and shape on the dry sand shear behaviour, In proc., *13th International Conference on Soil Mechanics and Foundation Engineering*, Vol. 1, pp. 13–16.

Dezfooli, M. 2014. Staged construction modeling of large diameter steel pipes using 3-D nonlinear finite element analysis, *Ph.D. dissertation*, Univ. of Texas, Arlington, TX.

Duncan J. M., and Seed, R. B. 1986. Compaction induced earth pressures under K_0 conditions, *J Geotech Eng*, 112 (1):1–22.

Ezzeldin, I., and Naggar, H. E. 2021. Three-dimensional finite element modeling of corrugated metal pipes, *Transportation Geotechnics*, 27: 100467.

Farhadi, B. 2013. Numerical modeling of pipe-soil interaction under transverse direction, *Master's thesis*, University of Calgary, Canada.

Guo, P. 2005. Numerical modeling of pipe-soil interaction under oblique loading, *Journal of Geotechnical and Geoenvironmental Engineering,* 131 (2): 260-268.

Hsu, T.-W. 1996. Soil restraint against oblique motion of pipelines in sand, Canadian Geotechnical Journal 33: 180-188.

Janbu, N. 1963. Soil compressibility as determined by oedometer and triaxial tests. In Proc., *European Conf. on Soil Mechanics and Foundation Engineering (ECSMFE)*, 19–25. Essen, Germany: German Society for Earthworks and Foundations.

Jung, J. K., T. D. O'Rourke, and N. A. Olson. 2013. Lateral soil-pipe interaction in dry and partially saturated sand, *J. Geotech. Geoenviron. Eng.*, 139 (12): 2028–2036.

Katona, M. G. 1978. Analysis of long-span culverts by the finite element method. *Transp Res Rec*, Transp Res Board, Washington, DC, 678:59–66.

Karimian, S. A. 2006. Response of buried steel pipelines subjected to longitudinal and transverse ground movement, *Ph.D. thesis*, University of British Columbia, Canada.

Lings, M.L., and Dietz, M.S. 2004. An improved direct shear apparatus for sand, *Geotechnique*, 54 (4):245-256.

McGrath, T. J., Selig, E. T., Webb, M. C., and Zoladz, G. V. 1999. Pipe interaction with the backfill envelope, Report No. FHWA-RD-98-191, US Department of Transportation.

Meidani, M., Meguid, M.A., and Chouinard, L.E. 2018. Estimating earth loads on buried pipes under axial loading condition: insights from 3D discrete element analysis, *Geo-Engineering*, 9:5.

Mirmoradi, S. H., and Ehrlich, M. 2015. Numerical evaluation of the behavior of GRS walls with segmental block facing under working stress conditions, *Journal of Geotechnical and Geoenvironmental Engineering*, 141 (3):04014109.

Muntakim, A.H., and Dhar, A.S. 2020. Assessment of axial pullout force for buried medium-density polyethylene pipelines, *Journal of Pipeline Systems Engineering and Practice*, 12 (2).

Murugathasan, P., Dhar, A.S., and Hawlader, B. 2021. An experimental and numerical investigation of pullout behavior of buried ductile iron water pipes in sand, *Canadian Journal of Civil Engineering*, 48 (2): 134–143.

Nyman, K. 1984. Soil response against the oblique motion of pipes, *ASCE Journal of Transportation Engineering,* 110 (2): 190-202.

PRCI (Pipeline Research Council International) 2009. Guidelines for constructing natural gas and liquid hydrocarbon pipelines through areas prone to landslide and subsidence hazards, Report prepared for the Design, Material, and Construction committee, Pipeline Research Council International, Inc.

Reza, A. and Dhar, A. S. 2024. Finite-element modelling of axial movements of polyethylene pipes in dense sand, *Transportation Geotechnics*, 48, 101336.

Reza, A., and Dhar, A.S. 2021. Axial pullout behavior of buried medium-density polyethylene gas distribution pipes, *International Journal of Geomechanics*, 21(7).

Robert, D. J., P. Rajeev, J. Kodikara, and B. Rajani. 2016. Equation to predict maximum pipe stress incorporating internal and external loadings on buried pipes, *Can. Geotech. J.*, 53 (8): 1315–1331.

Roscoe, K. H. 1970. 10th Rankine Lecture: The influence of strains in soil mechanics. *Géotechnique*, 20 (2): 129–170.

Roy, K., B. Hawlader, S. Kenny, and I. Moore. 2016. Finite element modeling of lateral pipeline–soil interactions in dense sand, *Can. Geotech. J.*, 53 (3): 490–504.

Saha, R.C., Dhar, A.S., and Hawlader, B.C. 2019. Shear strength assessment of a well graded clean sand, In Proc., GeoSt. John's 2019, *72nd Canadian Geotechnical Conference*, St. John's, NL, Canada.

Saleh, A. E., Jalali, H. H., Pokharel, A., and Abolmaali, A. 2021. Deformation of buried large diameter steel pipes during staged construction and compaction-case study and finite element analysis. *Transport Geotech*, 31:100649.

Scotland, I., Dixon, N., Frost, M., Fowmes, G., and Horgan, G. 2016. Modelling deformation during the construction of wrapped geogrid-reinforced structures, *Geosynthetics International*, 23 (3).

Sinha, T., and A. S. Dhar. 2023. Beam-on-spring modeling of buried MDPE pipes in sand subjected to lateral loads a at pipe junction, *J. Pipeline Syst. Eng. Pract.*, 3 (3): 100125.

Wang, F., Han, J., Corey, R., Parsons, R. L., Sun, X. 2017. Numerical modeling of installation of steel-reinforced high-density polyethylene pipes in soil, *J Geotech Geoenviron Eng*, 143 (11):04017084.

Ye, M., Ni, P., and Maitra, S. 2024. Response of flexible pipes buried in sand under multi-directional movement: understanding fault-pipeline interaction, *Soil Dynamics and Earthquake Engineering,* 187, 108978.

Chapter 5: Conclusion and Recommendations

5.1 Overview

Small-diameter steel pipes are widely used in Canada for the safe transportation of oil and natural gas for domestic purposes. These pipelines are often routed through unstable ground conditions, which can affect their performance and safety. However, there is limited research on the behavior of small-diameter steel pipes in such conditions. Most existing studies focus on scenarios where the steel pipe is pulled through a static soil mass. On the other hand, this study involved axially pulling the soil mass while restraining the pipe at one end, simulating a more realistic ground movement scenario. Twelve full-scale laboratory tests were conducted to investigate the response of the buried pipeline under axial ground loading. The effects of two different compaction techniques and three different ground movement rates were studied. More specific conclusions related to experimental studies and numerical modeling mentioned in the study are discussed in detail in the previous two chapters, while a brief overview of the findings and some general conclusions are presented in this chapter.

5.2 Conclusions

The following key conclusions can be drawn from the experimental and numerical analysis of small-diameter steel pipe subjected to axial ground movement:

- Though the design guidelines (ALA 2005, PRCI 2009) provided a close match in predicting the peak axial force for loose backfill, they were unsuccessful in predicting the peak axial force for compacted backfill. The discrepancy in predicting peak axial force in compacted backfill was mainly associated with compaction-induced energy.

- Compared to the hand tamper compaction technique, the vibratory plate compactor induced higher energy, resulting in a higher peak axial force for the same-diameter pipe. The effect of pipe diameter was also evident in the peak normalized force, with a higher normalized value observed for the relatively smaller diameter pipe.
- Since the axial elongations were not significant (i.e., 1-2 mm), the tests used in this study can be considered element-level tests and may be utilized to improve design guidelines. Additionally, the axial strain on the pipe crown near the fixed pipe end was found to be very negligible.
- The classical Mohr–Coulomb plasticity model was employed to predict the peak axial resistance experienced by the steel pipe. From the FE analysis, it was evident that both the normal and shear stress distributions were uniform along the length of the pipe. However, the effect of shear-induced dilation was absent or negligible during the soil-pulling phase.
- The modified earth pressure coefficient, as proposed by Meidani et al. (2018), was successful in predicting the peak axial force when the backfill soil was compacted using the hand tamper. However, the effect of compaction-induced energy was not taken into account by Meidani et al. (2018).

- The misalignment of pipe placement in the horizontal plane during full-scale laboratory tests could significantly increase the axial interacting forces, which could be attributed to the increase in normal pressure around the pipe. In the event of oblique loading conditions, the bending strain was also induced on the pipeline, along with the axial strain.

5.3 Recommendations

While the current study provides valuable insight into axial soil-pipe interaction problems, further research can be conducted on the following areas to build upon the present study:

- Additional full-scale laboratory tests should be conducted, considering the misalignment of the pipe during placement in both the vertical and horizontal planes, to understand the effect of inclination angles.
- The effect of soil displacement rates was evident in normalized force, with higher normalized forces observed for lower displacement rates. However, more full-scale tests with varying pipe diameters will be needed to conclude the impacts of soil displacement rates on axial soil resistance.
- When comparing the nondimensional peak forces of this study with those in the literature, the present study showed consistently higher forces. It is worth noting that most previous studies involved relatively larger-diameter pipes being pulled through static soil. The higher normalized peak forces observed in this study could be attributed to differences between the pipe-pulling and soil-pulling

mechanisms. Further studies should focus on the soil-pulling mechanism for larger-diameter pipes.

- The peak axial force on steel pipes can be significantly influenced by surface roughness and coating thickness of the pipe. Specific studies should be concentrated on various pipe segments, including non-coated (e.g., smooth, intermediate, and rough) and coated (e.g., fusion-bonded epoxy, high-performance powder coating, epoxy asphalt, and galvanizing) segments to explore their effects on axial force.
- As expected, compaction-induced energy and lift thickness can affect the peak axial force of small-diameter steel pipes. Future studies should investigate different compaction techniques with varying lift thicknesses. Pressure transducers might also be attached to the pipe wall to measure the compaction-induced stress on the pipe surface.
- The classical Mohr–Coulomb model was unable to simulate the post-peak response observed in the test results, and the initial slope of the analysis also differed from that observed in the full-scale tests. Advanced soil constitutive models with varying friction and dilation angles should be used to better understand the interface interactions and provide more accurate predictions.
- The FE analysis revealed that strain distribution was not uniform across the pipe sections. To capture detailed and continuous strain information, strain gauges or optical distributed sensor interrogators should be employed across different locations of the pipe.

References

ALA. 2005. Guidelines for the design of buried steel pipe, American Lifelines Alliance, Reston, VA, USA.

Al-Hussaini, M.M. and Townsend, F.C. 1975. Investigation of K_0 testing in cohesionless soils, Technical Report S-75-16, U.S. Army Engineer Waterways Experiment Station, Vicksburg, Miss. 39180.

Al-Khazaali, M., and Vanapalli, S.K. 2019. Axial force-displacement behaviour of a buried pipeline in saturated and unsaturated sand, *Géotechnique*, 69 (11).

Andersen, D. 2024. Behavior of small-diameter buried steel pipes subjected to axial ground movement, *M.Eng. thesis*, Memorial University of Newfoundland, Canada.

Anderson, C. 2004. Soil–pipeline interaction of polyethylene natural gas pipelines in sand, *MSc thesis*, Department of Civil Engineering, The University of British Columbia, Vancouver, BC, Canada.

ASCE. 1984. Guidelines for the seismic design of oil and gas pipeline systems, Committee on Gas and Liquid Fuel Lifelines, Technical Council on Lifeline Earthquake Engineering, *American Society of Civil Engineers*, New York, USA.

Bilgin, Ö., and Stewart, H.E. 2009a. Design guidelines for polyethylene pipe interface shear resistance, *Journal of Geotechnical and Geoenvironmental Engineering*, 135 (6): 809–818.

Bilgin, Ö. and Stewart, H. E. 2009b. Pullout resistance characteristics of cast iron pipe, *Journal of Transportation Engineering*, 135 (10): 730–735.

Budhu, M. 2010. Soil mechanics and foundations, 3rd ed.; John Wiley & Sons, Inc.: Hoboken, NJ, USA, ISBN 978-0-470-55684-9.

CAPP (Canadian Association of Petroleum Producers). 2024. Energy and the Canadian economy, Retrieved April 10, 2024, from https://www.capp.ca/en/our-priorities/energy-and-the-canadian-economy/.

CER (Canada Energy Regulator). 2024. Provincial and territorial energy profiles – Canada, Retrieved April 10, 2024, from https://www.cer-rec.gc.ca/en/data-analysis/energy-markets/provincial-territorial-energy-profiles/provincial-territorial-energy-profiles-canada.html.

Chakraborty, S., Dhar, A.S., and Reza, A. 2021. A laboratory investigation of buried 42-mm diameter MDPE branched pipes under relative axial ground movements, In Proc., of *74th Canadian Geotechnical Conference*, GeoNiagara 2021, Niagara Falls, ON, Canada, September 26-29.

Chen, T.-J., and Fang, Y.-S. 2008. Earth Pressure due to vibratory compaction, *Journal of Geotechnical and Geoenvironmental Engineering*, 134 (4): 437-444.

Davis, E.H. 1968. Theories of plasticity and the failure of soil masses, In soil mechanics: selected topics (ed. I. K. Lee), pp. 341–380, London: Butterworth.

Dewar, D. 2019. A suggested soil and/or rock to pipeline landslide interaction classification system, Geo St. John’s, Canada.

Guo, C., and Zhou, C. 2024. Axial behaviour of steel pipelines buried in sand: effects of surface roughness and hardness, Géotechnique.

Hansen, J.B. 1961. The ultimate resistance of rigid piles against transversal forces, Bulletin 12, Danish Geotechnical Institute, Copenhagen, Denmark.

Janbu, N. 1963. Soil compressibility as determined by oedometer and triaxial tests, In Proc., *European Conf. on Soil Mechanics and Foundation Engineering (ECSMFE)*, 19–25, Essen, Germany: German Society for Earthworks and Foundations.

Karimian, S. A. 2006. Response of buried steel pipelines subjected to longitudinal and transverse ground movement, *Ph.D. thesis*, University of British Columbia, Canada.

Katebi, M., Maghoul, P., and Blatz, J. 2019. Numerical analysis of pipeline response to slow landslides: case study, *Canadian Geotechnical Journal*, 56 (12): 1779–1788.

Kouretzis, G.P., Karamitros, D.K., and Sloan, S.W. 2015. Analysis of buried pipelines subjected to ground surface settlement and heave, *Canadian Geotechnical Journal*, 52 (8): 1058-1071.

Kulhawy, F.H., and Mayne, P.W. 1990. Manual on estimating soil properties for foundation design, Report EPRI-EL 6800, Electric Power Research Institute, Palo Alto. pp. 306.

Kunert, H.G., Marquez, A.A., Fazzini, P., and Otegui, J.L. 2016. Failures and integrity of pipelines subjected to soil movements, In Handbook of Materials Failure Analysis with Case Studies from the Oil and Gas Industry, pp. 105–122.

Lings, M.L., and Dietz, M.S. 2004. An improved direct shear apparatus for sand, *Géotechnique*, 54 (4): 245-256.

Meidani, M., Meguid, M.A., and Chouinard, L.E. 2018. Estimating earth loads on buried pipes under axial loading condition: insights from 3D discrete element analysis, *Geo-Engineering*, 9:5.

Muntakim, A.H., and Dhar, A.S. 2020. Assessment of axial pullout force for buried medium-density polyethylene pipelines. Journal of Pipeline Systems Engineering and Practice, 12 (2).

Murugathasan, P., Dhar, A.S., and Hawlader, B. 2021. An experimental and numerical investigation of pullout behavior of buried ductile iron water pipes in sand, *Canadian Journal of Civil Engineering*, 48 (2): 134–143.

NRC (Natural Resources Canada). 2020. Pipelines across Canada. Retrieved November 14, 2023, from https://natural-resources.canada.ca/our-natural-resources/energy-sources-distribution/fossil-fuels/pipelines/pipelines-across-canada/18856.

O'Rourke, M. J., and Liu, X. 2012. Seismic design of buried and offshore pipelines, MCEER Monograph, MCEER-12-MN04.

O'Rourke, M. J. 1989. Approximate analysis procedures for permanent ground deformation effects on buried pipelines, In Proc., of the *Second U.S.-Japan Workshop on Liquefaction, Large Ground Deformation and Their Effects on Lifelines*, Buffalo, New York, Technical Report NCEER-89-0032, Multidisciplinary Center for Earthquake Engineering Research, Buffalo, New York, pp. 336-347.

PRCI. 2017. Guidelines for constructing natural gas and liquid hydrocarbon pipelines through areas prone to landslide and subsidence hazards, Design, Material and Construction Committee of Pipeline Research Council International, Inc., Virginia, USA.

Reza, A., and Dhar, A.S. 2021. Axial pullout behavior of buried medium-density polyethylene gas distribution pipes, *International Journal of Geomechanics*, 21 (7).

Roy, K., B. Hawlader, S. Kenny, and I. Moore. 2016. Finite element modeling of lateral pipeline–soil interactions in dense sand, *Can. Geotech. J.*, 53 (3): 490–504.

Saberi, M., Annan, C.D., and Sheil, B.B. 2022. An efficient numerical approach for simulating soil-pipe interaction behaviour under cyclic loading, *Computers and Geotechnics*, 146.

Sarvanis, G.C., Karamanos, S.A., Vazouras, P., Mecozzi, E., Lucci, A., and Dakoulas, P. 2017. Permanent earthquake-induced actions in buried pipelines: numerical modeling and experimental verification, *Wiley*, 47 (4): 966-987.

Sheil, B.B., Martin, C.M., Byrne, B.W., Plant, M., Williams, K., and Coyne, D. 2018. Full-scale laboratory testing of a buried pipeline in sand subjected to cyclic axial displacements, *Géotechnique*, 68 (8): 684–698.

Shi, P. 2015. Seismic wave propagation effects on buried segmented pipelines, *Soil Dynamics and Earthquake Engineering*, 72: 89-98.

Statistical Review of World Energy. 2024. BP Statistical Review, London, UK.

TSB (Transportation Safety Board of Canada). 2024. Monthly and annual statistics on pipeline occurrences, Retrieved April 10, 2024, from https://www.tsb.gc.ca/eng/stats/pipeline/stats.html.

Weerasekara, L., and Wijewickreme, D. 2008. Mobilisation of soil loads on buried polyethylene natural gas pipelines subject to relative axial displacements, *Canadian Geotechnical Journal*, 45 (9): 1237–1249.

Wijewickreme, D., Karimian, H., and Honegger, D. 2009. Response of buried steel pipelines subjected to relative axial soil movement, *Canadian Geotechnical Journal*, 46 (7): 735–752.

Appendix A: Figures of Test Setup and Procedure

Figure A.1: Full-scale test facility developed at Memorial University of Newfoundland (Side view)

Figure A.2: Full-scale test facility developed at Memorial University of Newfoundland

(Front view)

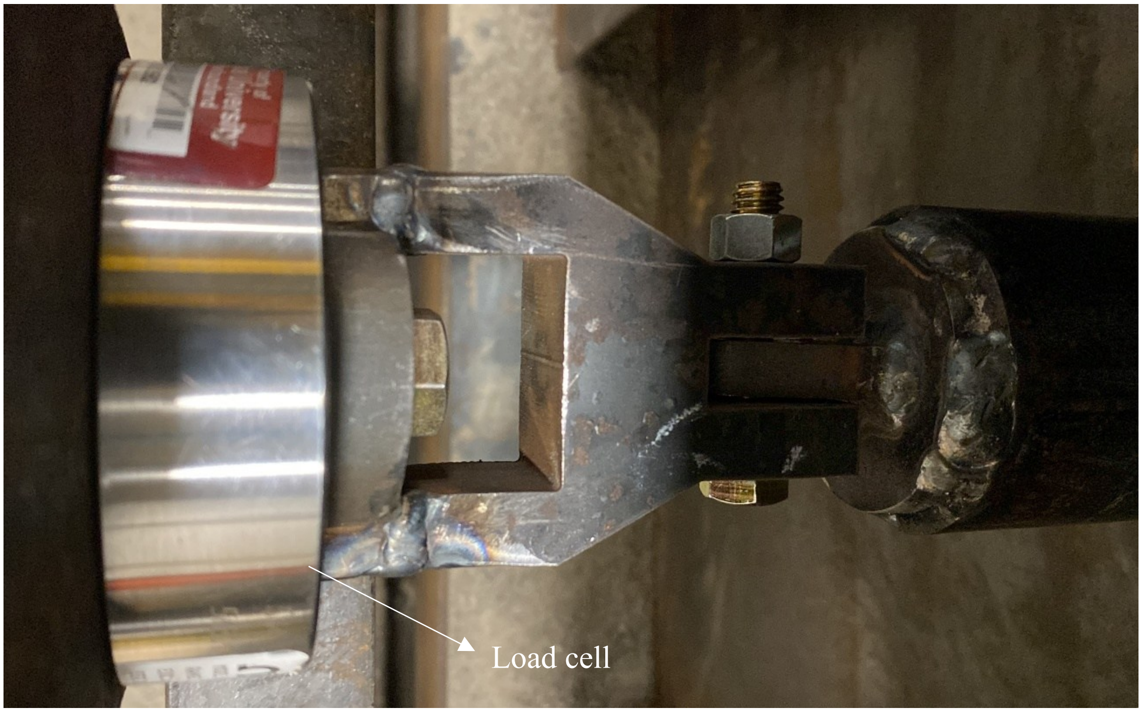

Figure A.3: Load cell connection

Figure A.4: Sand dumping process inside the tank

Figure A.5: Finished surface after the hand tamper compaction of the first layer

Figure A.6: Density measurement process using the sand-cone method (ASTM D1556)

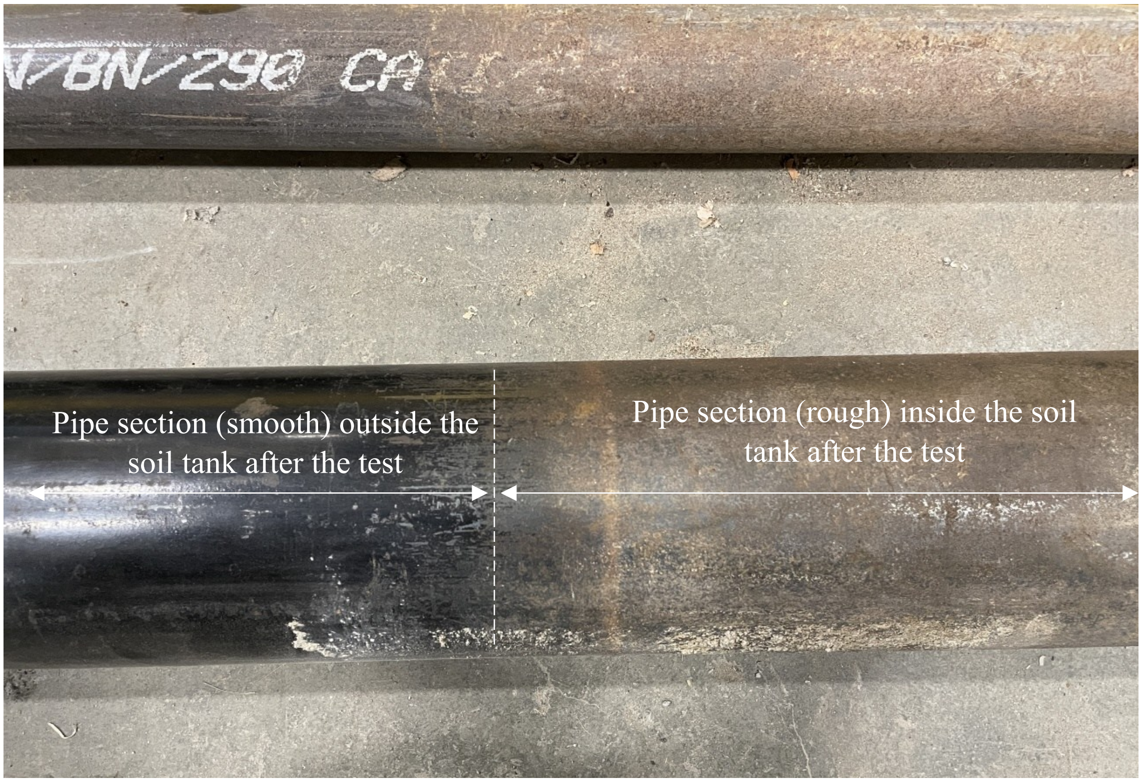

Figure A.7: Pipe segment after the test